CHARACTERISATION OF THE WAVEGUIDE DEPENDENCE OF OPTICAL MODE LOSS IN SEMICONDUCTOR LASERS

Author:

PETER EDWARD REES

Cardiff University
School of Physics and Astronomy

A THESIS SUBMITTED IN ACCORDANCE WITH THE REQUIREMENTS FOR
THE DEGREE OF DOCTOR OF PHILOSOPHY IN PHYSICS

YEAR: 2017

Contents

List of Figures

4

List of Tables

Abstract

The improvement of optical mode loss in semiconductor lasers is of significant commercial value, contributing to lower threshold current densities and higher above-threshold slope efficiencies. While it has improved significantly with successive developments in semiconductor laser design resulting from improvements to the fabrication process, characterisation methods for the measurement of optical mode loss have not kept pace. Today values of optical mode losses as low as 1cm^{-1} are frequently reported, and yet the precision and accuracy of its measurement are rarely better than 1cm^{-1} itself.

To address this, I demonstrate that a modulated approach to the segmented contact method for the measurement of modal absorption and loss can measure optical mode losses with precisions as low as 0.1cm^{-1}. I also demonstrate the removal of non-linearity from detection system using a novel approach to amplitude calibration by flux superposition.

I apply this improved methodology in the comparison of InAs QD samples with differing waveguide core dimensions (2440Å and 3740Å), finding a reduction in optical mode loss between these samples from (4.8±0.4)cm^{-1} to (2.25±0.10)cm^{-1}.

In addition to measuring the optical mode loss at the lasing wavelength I investigated the origins of the observed wavelength dependence of optical mode loss below the material band-edge, comparing experimental values of modal absorption and loss spectra with a waveguide model. I show the wavelength dependent optical mode loss of wide waveguide core samples agrees well with losses predicted from model incorporating free carrier absorption, intervalence band absorption and waveguide dispersion. I also show that in both samples optical mode losses and their respective wavelength dependences are insensitive to changes in temperature from 298-370K. I also investigate the causes of oscillating modal absorption and loss seen in narrow waveguide core samples.

Acknowledgements

I would like to express my gratitude to both Professors Peter Smowton and Peter Blood for the years of guidance they have provided as well as the inspiring enthusiasm they have for this subject. I would also like to thank all members of the Optoelectronics research group, both current and past, who have in a thousand ways contributed to this work through the experiences and advice they have shared with me.

To my friends at Cardiff University School of Physics and Astronomy, thank you for always being there for me when I most needed distracting from my work.

Lastly, I dedicate this thesis to my loving and supportive family. Most especially to my wife, Katie, without whose encouragement I might never have studied physics, and to our newborn son, Owen, who provided me with the motivation to finish this thesis.

Chapter 1   Introduction

1.1   Context

Semiconductor lasers are integral to technologies that define our age. The coherency offered by laser light is necessary for the long distance fibre optic based telecommunications used in global communications and its reliant industries, such as the global stock market and internet based technologies. Technology industry leaders including Hewlett Packard and IBM are looking to integrate semiconductor lasers into modern life further through their use in optical interconnects, a key enabler for improving data transmission rates and reducing power consumption both at the scale of data centres and personal computing. (Tan et al., 2013)(IBM, 2015)

Currently one of the biggest markets for semiconductor lasers is as pump sources for high power fibre lasers used in materials processing and defence applications. Here the high electric-optical conversion efficiency (of the order of 60%) makes them attractive pump sources, however the remaining inefficiencies combined with high power requirements (kilowatts are typical) leads to additional cooling requirements to maintain device efficiency and lifetime. These requirements add significant expense and volume to these systems which could potentially be eliminated with improved optical efficiency.

With this growing dependence upon semiconductor laser technologies, there is now greater need than ever for improvements in their threshold current densities, wall-plug efficiency and lifetime performance. Semiconductor lasers have seen progressive improvements in their performance throughout the decades. The original semiconductor lasers were demonstrated in bulk GaAs p-n junctions in 1962 (Hall et al., 1962)(Nathan et al., 1962) but we have since seen the introduction of double heterostructures, quantum confinement by quantum wells and quantum dots; and separate confinement heterostructures, each with subsequent improvements in the threshold current densities observed (Alferov, 2000). These improvements have been enabled by greater control and quality in the growth of laser structures with the introduction of metal-organic vapor-phase and molecular beam epitaxial methods.

Currently, the best threshold current densities exhibited by semiconductor lasers incorporate quantum dots in a separate confinement heterostructure, and present a good option for optical interconnects formed by the direct growth of III-V materials on silicon substrates due to their low power consumption and insensitivity to defects formed by this process (Liu et al., 2015)(Chen et al.,

2016). However quantum dots also typically exhibit lower optical gain due to their reduced optical cross section (with respect to quantum wells), necessitating the reduction of mirror loss by increasing their cavity lengths or their mirror reflectivity. A consequence of this is the performance of these devices, with respect to both threshold current density and above threshold slope efficiency, becomes more highly dependent upon optical mode loss.

Presently, the optimisation of semiconductor lasers for optical mode loss is more commonly demonstrated in the waveguide design of quantum cascade lasers. This is because the typical emission of these devices (mid-infrared and terahertz wavelengths) leads to much higher values of optical mode loss (in excess of $10cm^{-1}$) due to higher absorption of light from intervalence band and free carrier absorptions (Bengloan et al., 2005). However in QD lasers emitting at telecommunications wavelengths (1.3-1.6μm), optical mode losses are much lower, frequently below $5cm^{-1}$, with some reports lower than $1cm^{-1}$. An example of this is epitomised by Slipchenko et al values for quantum well laser diodes with optical loss measured as low as $0.34cm^{-1}$ in (Slipchenko et al, 2004), wherein the experimental uncertainty (which is not commented upon or calculated by the authors) is apparently far greater than the value of $0.34cm^{-1}$ itself, and relies upon a choice number of data points contributing to the value's calculation. Currently the optimisation of optical mode losses in such devices is not commonly explored, likely because the experimental uncertainties in its measurement by conventional methods are typically much larger than the improvements in optical mode loss we might hope to achieve.

In order to satisfy the need to improve efficiency of semiconductor lasers, approaches to the characterisation of optical mode loss must keep pace. This work aims to do this by introducing improvements to the measurement of modal absorption and loss through the electrically pumped segmented contact method (Blood et al., 2003) with the goal of measuring optical mode loss to within precisions of $0.1cm^{-1}$ for the purpose of comparing lasers with a difference less than $1cm^{-1}$. We will go on to test structures which differ only in the design of their waveguide in order to interrogate the waveguide dependence of optical mode loss. In particular, we will vary the waveguide core thickness in InAs quantum dots in $In_{0.15}Ga_{0.85}As$ quantum well lasers with a separate confinement heterostructure formed from GaAs and $Al_{0.4}Ga_{0.6}As$ layers.

1.2   Thesis Overview

In *Chapter 2 Background Theory* we provide the necessary theory required for understanding this work. This includes an overview of the behaviour of semiconductor lasers employing separate

confinement heterostructures and quantum dots, the origins of optical mode loss and its impact on the performance of these devices.

The already established experiment methodologies used in this work are provided in *Chapter 3 Experiment Methodology*. These include details of the measurement of commonly measured figures of merit of lasers (e.g. laser threshold current and above-threshold slope efficiency), as well as a detailed description of the Segmented Contact Method (SCM) for the measurement of modal absorption and loss. This will be discussed in the context of other methods for the measurement of optical mode loss.

Improvements to the measurement of modal absorption and loss by the SCM are discussed in *Chapters 4* and *5*. Firstly, we address uncertainties in the measurement arising from the drift in experimental conditions with long integration times by the *Modulated Method of Modal Absorption and Loss by SCM*. Through this, we demonstrate the modulated SCM is capable of measuring the optical mode loss of segmented contact devices with precisions of 0.1cm^{-1}.

In *Chapter 5 Amplitude calibration by flux superposition,* we go on to identify a non-linear response to the measurement of light by the photodetector array used in the SCM. This was found as a result of investigating causes for a persistent upward trend in optical mode loss with increasing wavelength in samples measured. To resolve this we develop an amplitude calibration method based upon the principle of flux superposition which is sensitive to the requirements of the apparatus used in the SCM.

Through this we demonstrate this approach to the flux superposition calibration method is capable of calibrating the amplitude of multiple photodiode elements simultaneously. We confirm the upward trend in optical mode loss is not the result of detector non-linearity, informing later work in *Chapter 6*. This work also substantially improves the accuracy of measurements of large values of modal absorption and loss (>10cm^{-1}) by the SCM and removes significant noise contributions arising from varying levels of non-linearity between photodiode elements. We also demonstrate how this method can be used for characterising the non-linearity of the detector system under different experimental conditions.

In *Chapter 6 Waveguide Core Dependence of Optical Mode Loss* we apply the discussed improvements in the measurement of modal absorption and loss by the SCM in order to precisely

characterise optical mode loss in structures with differing waveguide core thickness (2440Å and 3740Å). We begin by characterising the laser emission of these devices, finding a significant improvement in above-threshold slop efficiency in laser samples with wide waveguide cores. This is consistent with reduced optical mode loss. We confirm this is the case with the amplitude calibrated, modulated SCM for measurement of modal absorption and loss, finding a significant increase in the optical mode loss of samples with narrower waveguide cores. Optical mode losses of

and   are measured for the wide and narrow waveguide core samples respectively. Comparison of this result with measured differential quantum efficiencies suggest optical mode loss is the largest contributor of reduced efficiency between these devices. We also identify an oscillating feature in the modal absorption and loss of narrow waveguide cores.

Waveguide modelling of these samples is used to investigate the upward trend in optical mode loss in these samples with increasing wavelength, as a result of the wavelength dependence of intervalence band absorption, free carrier absorption and dispersion of the waveguide. The upward trend in optical mode loss in wide waveguide core samples is found to be consistent with this model. The model does not account for the much greater wavelength dependence seen in the narrow waveguide core samples. Peaks in the modelled data suggest that the optical mode is weakly guided, allowing for resonances with the device structure beyond the cladding layers of the device to occur. However the one dimensional model presented does not account for the shorter wavelength spacing of oscillations in the experimental data.

I go on to test whether the improved SCM may measure a temperature dependence in the optical mode loss of wide or narrow waveguide core samples. Band-edge shifts with respect to temperature are well matched between these samples, suggesting the band-gap between respective QDs and wetting layers are identical. There is no consistent change in the wavelength dependence of optical mode loss or its net value with increasing temperature.

As part of this experiment, we investigate the oscillations in modal absorption and loss in narrow waveguide samples further. No correlation of the phase of these oscillations is found with the band-shift of devices. We do however find a consistent increase in the wavelength peak spacing of oscillations with temperature. This behaviour compares favourably with similar oscillations in the absorption spectra of bent optical fibres. We propose the oscillations are due to weak guiding of the

optical mode (this is supported by the resonant coupling predicted in the waveguide modelling of these samples) and bowing of the devices.

A discussion of the findings of this work and the direction future investigations could take are provided in *Chapter 7 Conclusion*.

ALFEROV, Z. 2000. Double heterostructure lasers: early days and future perspectives. *IEEE Journal of Selected Topics in Quantum Electronics,* 6**,** 832-840.

S. O. SLIPCHENKO, D. A. VINOKUROV, N.A. PIKHTIN, Z. N. SOKOLOVA, A. L. STANKEVICH, I.S. TARASOV, ZH. I. ALFEROV. Ultralow Internal Optical Loss in Separate-Confinement Quantum-Well Laser Heterostructures. *Physics of Semiconductor Devices,* Vol 38, Issue 12, pp1430-1439.

BENGLOAN, J. Y., SAPIENZA, L., CALLIGARO, M., PARILLAUD, O., LECOMTE, M., MARCADET, X. & SIRTORI, C. Dielectric waveguide optimisation for GaAs based quantum cascade lasers. 2005 Quantum Electronics and Laser Science Conference, 22-27 May 2005 2005. 1002-1004 Vol. 2.

BLOOD, P., LEWIS, G. M., SMOWTON, P. M., SUMMERS, H., THOMSON, J. & LUTTI, J. 2003. Characterization of semiconductor laser gain media by the segmented contact method. *IEEE Journal of Selected Topics in Quantum Electronics,* 9**,** 1275-1282.

CHEN, S., LI, W., WU, J., JIANG, Q., TANG, M., SHUTTS, S., ELLIOTT, S. N., SOBIESIERSKI, A., SEEDS, A. J., ROSS, I., SMOWTON, P. M. & LIU, H. 2016. Electrically pumped continuous-wave III–V quantum dot lasers on silicon. *Nat Photon,* 10**,** 307-311.

HALL, R. N., FENNER, G. E., KINGSLEY, J. D., SOLTYS, T. J. & CARLSON, R. O. 1962. Coherent Light Emission From GaAs Junctions. *Physical Review Letters,* 9**,** 366-368.

IBM 2015. IBM's Silicon Photonics Technology Ready to Speed up Cloud and Big Data Applications. *In:* VU, C. (ed.). Website Press Release.

LIU, A. Y., HERRICK, R. W., UEDA, O., PETROFF, P. M., GOSSARD, A. C. & BOWERS, J. E. 2015. Reliability of InAs&;GaAs Quantum Dot Lasers Epitaxially Grown on Silicon. *IEEE Journal of Selected Topics in Quantum Electronics,* 21**,** 690-697.

NATHAN, M. I., DUMKE, W. P., BURNS, G., JR., F. H. D. & LASHER, G. 1962. STIMULATED EMISSION OF RADIATION FROM GaAs p   n JUNCTIONS. *Applied Physics Letters,* 1**,** 62-64.

TAN, M. R. T., MCLAREN, M. & JOUPPI, N. P. 2013. Optical Interconnects for High-Performance Computing Systems. *IEEE Micro,* 33**,** 14-21.

Chapter 2   Background Theory

2.1   Introduction

In this chapter we begin with an overview of the fundamentals of laser diode behaviour and how they relate to the InAs quantum dot semiconductor lasers measured within this work (Section 2.2). We will then give a detailed discussion of optical mode loss in semiconductor lasers, including its impact on device performance (threshold current density and above threshold slope efficiency); its origin in InAs QD laser diodes emitting at 1.3µm and approaches to reduce the magnitude of this loss (Section 2.3).

2.2.0 Laser Diodes and their General Behaviour

The key requirements for laser action to occur include: a gain medium for the amplification of light, a "pumping" mechanism through which the amplifying properties of the gain medium are maintained and a feedback mechanism which maintains the coherence of the amplified light.

In semiconductor lasers, the gain medium consists of a semiconducting material where we can excite electrons to non-equilibrium energy levels (usually from the valence band to the conduction band). Collectively, electrons in these higher lying states can both emit and amplify light across a range of wavelengths. We explore the properties of the gain medium in more detail in Section 2.2.2.

The pumping of the gain medium is achieved by the electrical injection of carriers. In *diode lasers*, this is achieved by forming a p-i-n junction, where the central portion of the device which includes the gain medium is left undoped while the surrounding semiconductor material is doped during growth. When this structure is forward biased, electrons and holes are injected into the conduction and valence bands of the gain medium respectively. Under a high enough forward bias, a *population inversion* can be achieved in the gain medium (i.e. there are more electrons in the higher energy state than in the lower state).

Once a population inversion is achieved, light emitted by and propagating through the gain medium will experience an amount of amplification. In this work we consider edge-emitting lasers only, thus light will be propagating along the plane of the gain medium only. Feedback of this amplified light can be achieved by partial reflection from the facets of the device (Fig. 2.1), allowing light to make multiple passes through the gain medium. Other feedback mechanisms, such as those seen in ring cavity lasers or distributed feedback lasers, are also possible.

As the amplification of light approaches the overall cavity loss, that is the loss of light from transmission through the facets of the device (the mirror loss or α_m) and from propagating within the structure (the optical mode loss or α_i), the amplified light can make more passes through the medium. As the phase and energy of the amplified light is conserved the overall emitted light becomes more and more coherent. This increases to the point that the coherent output dominates the emission of the device, at which point it is said to begin *lasing*.

Attempts to increase the gain due to amplification beyond the cavity losses with further pumping, rather than causing a positive net gain, instead causes an increase in photon density within the laser cavity and typically much higher optical output.

Before this event, we consider the light emitted from the device as being only *amplified spontaneous emission* (ASE); but beyond this point it is said to begin *lasing*, made distinct by greater coherency in the emission. The coherence of the emission leads to a much narrower spectral linewidth of the emission; generally centred at the wavelength at which the condition for lasing was met in the gain medium.

2.2.1 Broad Area Emitting Laser Diode Structure
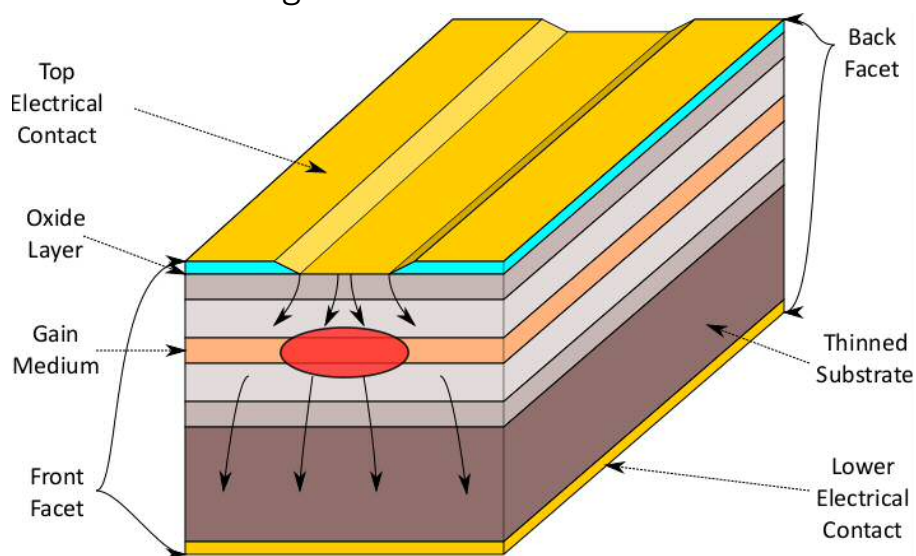
Figure 2.1 Broad area emitting, oxide-isolated stripe laser device (not to scale)

Broad area (BA) emitting laser diodes are formed by first defining exposed strips of the top semiconductor surface by deposition of an electrically insulating oxide layer, usually SiO_2, using photolithography. Metallisation of contacts following this step ensures good electrical contact is made with only a strip of the top of the semiconductor material, typically 50µm wide, and all of the lower contact. A complete description of device fabrication is provided in Section 3.2.

When a potential difference is applied between the top and bottom contacts, current flow near the top of the device is restricted to near the defined strip (with some current spreading as indicated). This causes the injection of carriers in the active region to also be limited to a small central strip of the gain medium, located near the top of the device.

This has the advantage that there is no surface recombination of carriers (i.e. no carriers near the sidewalls) within the gain medium. While this leads to better internal efficiency of the laser it also results in weak guiding of the optical mode (as there is no refractive index change in the lateral direction, and guiding due to gain is relatively weak). This results in *broad area* emission in the plain of the gain medium from the facets.

Feedback is provided by forming a Fabry-Perot cavity (a pair of partially reflective surfaces along the axis of propagation) by cleaving of the device facets perpendicular to the oxide defined stripe. The air-semiconductor index change is sufficient for forming a partially reflective interface at the facets.

2.2.2 Semiconductor Gain Medium

In semiconductors, the uppermost energy levels of the constituent atoms will intermix, forming many combinations of bonding and anti-bonding charge distributions which may be collectively described as energy bands. The highest *occupied* energy levels of the atoms will form the valence band, whilst the lowest *unoccupied* energy levels will form the conduction band. At T = 0K, and in the absence of any further excitation, the valence band is by definition completely occupied, while the conduction band is empty.

With excitation (or above T= 0K), electrons may be excited from the valence band into the conduction band. As well as contributing an electron to the conduction band, a *hole* is formed in the valence band, both of which contribute to conduction through the material.
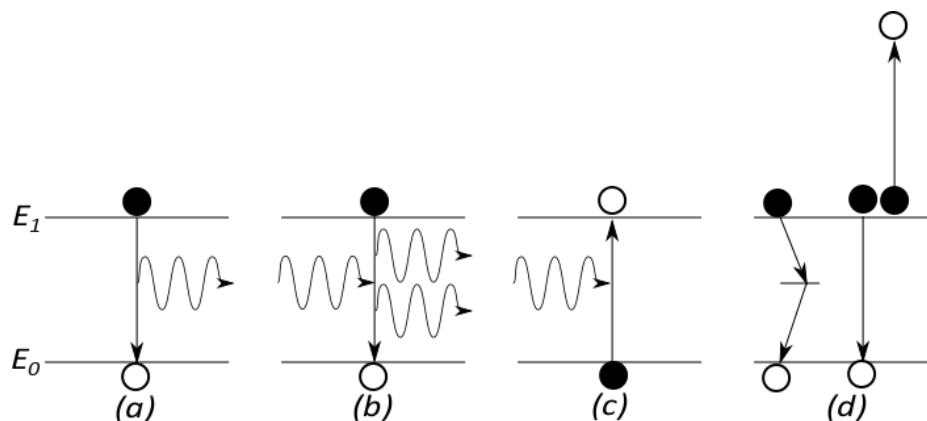
Figure 2.2 Electronic transitions between states with energies E_0 and E_1 respectively, including spontaneous emission (a), stimulated emission (b), absorption (c), and non-radiative processes including transition via additional states and Auger recombination (d). Dark and open circles indicate occupied and empty states respectively.

These electrons and holes can recombine (i.e. electrons from an occupied state in the conduction band make a transition into an unoccupied state of the valence band) through *radiative recombination*. Radiative recombination in turn may happen by a spontaneous process, i.e. *spontaneous emission* (Fig. 2.2 a) where the released photon is incoherent, or by an induced process in *stimulated emission* (Fig. 2.2 b). Importantly, photons generated by stimulated emission will possess the same energy, direction and phase as the inducing photon.

The reverse process to stimulated emission is also possible, *absorption,* where an electron from a low energy state undergoes a transition to a higher energy state with energy difference equal to the inciting photon (Fig. 2.2 c).

Finally, electrons and holes may also undergo *non-radiative recombination* (Fig. 2.2 d), where no photon is released. These can occur from electron transitions via intermediate states (i.e. impurity states either from device defects or surface states of the laser) where the energy is dissipated as *phonons*. Additionally, *Auger recombination* is the simultaneous excitation of a high energy state electron to a higher lying state through the recombination of another electron within this state with one of the three valence bands (split off, light hole and heavy hole bands), resulting in no net radiation. Momentum within the lattice is conserved by an equal but opposite change of k-vector for both of the Auger transitions. (Coldren and Corzine, 1995)

2.2.3 Confinement and Population Inversion

As discussed earlier, a *population inversion* is required before any net amplification of light by the gain medium can occur from the processes described in Fig. 2.2. In laser diodes, this is achieved by the formation of a *p-i-n* junction. Under forward bias, electrons are injected into the conduction band while holes are injected into the valence band. To achieve a large *local* population inversion in the gain medium the positions of large densities of electrons and holes must overlap. This contrasts with the conventional operation of a *p-n* junction diode seen in purely electronic applications, where the radiative recombination of carriers is undesirable and typically suppressed by preventing an overlap of large electron and hole densities.
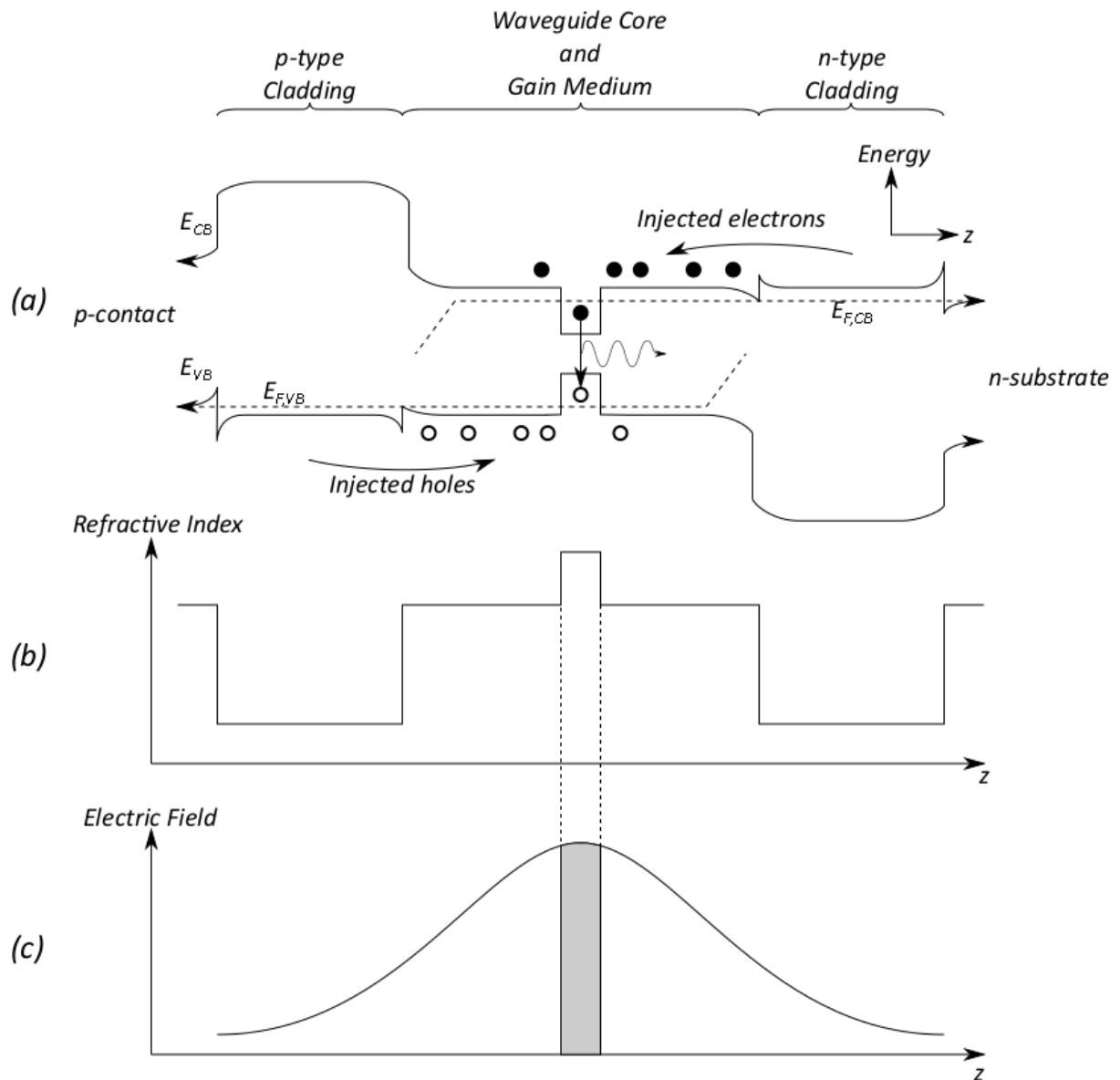
Figure 2.3 (a) Band diagram of separate confinement heterostructure with central quantum well under sufficient forward bias for a population inversion of the central gain medium. (b) Refractive index profile and (c) resulting optical mode profile and overlap with central gain medium.

Electrons and holes may be confined to the same position using a potential well in both the conduction and valence bands. Most commonly this is achieved by a double heterostructure of semiconductor materials where the gain medium, consisting of a thin layer of narrow band gap material, is surrounded by doped, wider band-gap materials (cladding). A large density of injected electrons and holes accumulate within the gain medium's potential well, allowing a large local population inversion to occur under lower current densities. Where quantum confined structures are used it is helpful to place the gain medium within a wider intermediary material with a narrower band-gap than the cladding region, as this ensures better carrier and optical confinement to the gain medium (Fig. 2.3 (a)). This is commonly described as a separate confinement heterostructure.

Optical confinement is achieved due to the contrast of refractive index between the narrow and wide band-gap materials in the heterostructure (Fig. 2.3 (b)). This helps confine the primary mode of light emitted by the laser to the gain medium (Fig. 2.3 (c)). The *modal gain*, *G*, of light propagating through the device is proportional to the overlap of the optical mode, , with the gain medium (Eq. 2.0). In our example, is the overlap integral of the mode over the area occupied by the quantum well shown in Fig. 2.3(c). It is also proportional to the *material* gain, *g*, which is defined as the amplification an optical mode will experience when entirely coupled to the gain medium. The calculation of the overlap factor is described further in Section 2.3.0.

$$\rule{6cm}{0.4pt}$$

Equation 2.0

When unbiased, the population of any given state in the device at a temperature is given by the Fermi function:

$$\frac{\rule{6cm}{0.4pt}}{\rule{3cm}{0.4pt}}$$

Equation 2.1

where , the Fermi energy, is determined by the total electrons in the system (Blood, 2015). By definition, for an intrinsic semiconductor at room temperature this is located close to the centre of the band gap. Given the energy gap between the valence and conduction bands, , is many times larger than , there is initially a small population of electrons in states within the conduction band (CB), and a large population in states within the valence band (VB).

Under forward bias, the injection of additional carriers causes the system to no longer be in equilibrium, and the above relationship (Eq. 2.1) does not hold. However, as energy is exchanged between the carriers of their respective bands on a far shorter timescale (~10ps) than the rate of recombination (~1ns), we can usually assume that the carriers within each band have an energy distribution which is in thermal equilibrium with the lattice. Thus while the *system* is not in equilibrium, there is an equilibrium within the CB and VB, therefore we can describe the system as being in *quasi-equilibrium*.

As we can regard the carrier distributions to be in thermal equilibrium within the CB and VB, we can attribute to each band a *quasi*-Fermi level, representative of their carrier populations:

$$\frac{\rule{6cm}{0.4pt}}{\rule{3cm}{0.4pt}}$$

22

Equation 2.2

where represents a state in the CB with a quasi-Fermi level , while:

$$\overline{\hspace{6cm}}$$

$$\overline{\hspace{3cm}}$$

Equation 2.3

where represents a state in the VB with a quasi-Fermi level . Thus a population inversion between two given states in the CB and VB respectively is achieved where:

Equation 2.4

From Eq. 2.4, the population inversion within a device can be shown to occur only where the quasi-Fermi separation exceeds the transition energy (this is known as the Bernard-Duraffourg condition). Hence for a population inversion to occur between states in the CB and VB:

Equation 2.5

where is the quasi-Fermi level separation. In any generalised system, must therefore be greater than the energy separation of the band edge of the gain medium. As is equal to the internal voltage of the diode (which is equal to the external voltage after a loss of potential due to series resistance), a larger population inversion (and a higher gain) is achieved in those energy states in which a population inversion has been achieved.

Where the population inversion is zero, there is no net gain and the material is transparent. As this occurs only when the photon energy is equal to , this transparency wavelength can be found experimentally and used to determine the value of for a given forward bias.

When there is sufficient population inversion to achieve the gain necessary for lasing, any further increase in the population inversion is suppressed by the resulting increase in stimulated emission. Instead of contributing to a larger carrier density, any increase in the injected current will result in photons contributing directly to the cavity photon density, hence we find that becomes *pinned* to its value at the threshold current.

2.2.4 Quantum Dots

The gain medium of the devices used in this work are self-assembled InAs quantum dots (QDs), grown via the Stranski-Krastanow (SK) mode (Eaglesham, 1990).

SK mode growth is achieved by the relaxation of strained material grown on deliberately lattice mismatched substrates. Under the growth conditions for SK to occur, strained material up to a few monolayers thick will relax to form small islands with quantum scale dimensions. Further growth of another material over the top of this will cause the electric potential of each of these islands to become confined in three dimensions.

This quantum confinement in three dimensions leads to a discrete set of states, as opposed to a continuum as found in quantum wells and bulk material. This is ideal for lasing, as it helps ensure that a narrow spontaneous emission spectrum is obtained; ideal for achieving ultra-low threshold laser devices. The narrow density of states should also limit the temperature sensitivity of such devices (Arakawa et al., 1982). Both of these effects are mitigated by the broad distribution of dot sizes (and hence broad set of discrete states), which results from the SK mode of growth. Despite this, improvements in laser diode temperature sensitivity and among the lowest lasing threshold current densities have been demonstrated (Liu et al., 1999)(Alferov, 2000).

The number of available states from a single layer of QDs can become completely inverted before sufficient gain to overcome the cavity losses of the laser is achieved. Therefore, QDs are often grown in multiple layers. Additional layers will also increase the current density required to create a population inversion, resulting in higher threshold current densities. Therefore the number of dot layers (and where possible the dot density of each layer) is optimised with respect to the cavity loss of the device. In addition, QDs are formed next to quantum wells; such that their narrow band gap potentials are adjacent to the wider band gap potential of the quantum wells. This aids in the confinement of charge to the QD layer, and is commonly called a DWELL structure.

As samples investigated in this work were made for the purpose of optimising the design of lasers grown monolithically on silicon substrates, we include the additional comments. Due to the large difference in the coefficient of thermal expansion between III-V semiconductors and silicon and the large variations in temperature experienced during epitaxial growth, monolithically grown devices tend to generate a large number of crystallographic defects, wherein non-radiative recombination of carriers can occur. The anticipated advantage of using QDs within this application is the reduction in

sensitivity to these defects. This is due to the localisation of recombining carriers to the QDs, reducing their interaction with defects propagating through layers containing the gain medium (Mi et al., 2009). The strain field surrounding QD layers is also expected to bend defects (which propagate upwards through the structure away from the substrate interface) away from the gain medium layers, increasing the likelihood of crystal defects annihilating with each other (Mi et al., 2006). Given this, additional defects introduced by recombination enhanced defect reactions throughout the operating lifetime of the device should have a reduced impact upon internal efficiency, and therefore exhibit better lifetime performance.

2.3.0 Internal Optical Mode Loss

Internal optical loss, α_i, is defined as the loss of light from the lasing optical mode of the laser as it propagates down the waveguide structure. As seen in Fig. 2.3, the mode will be distributed across multiple layers of the device. The photon energy of thiss laser light is typically smaller than the band gap of the materials through which it travels (the exception to this being the gain medium itself). As a result, this light is not subject to band-band absorptions by these layers. However an optical loss, , is still incurred due to mechanisms which persist for photon energies below the band gap, such as free carrier absorption.

The combined absorption from all layers is found from their respective absorption values, weighted by the confinement factor for each layer. For slab waveguides with k layers, we can express this with the following:

Equation 2.6

where the two dimensional confinement factors,   , (defined as perpendicular to the propagation of light) can be found from the normalised square of the electric field (propagating in the x direction as seen in Fig. 2.4) integrated across each layer's cross sectional area.

$$-$$

where   is the normalised transverse electric field profile.   and   define the dimensions of the slab waveguide elements (example dimensions for gain medium given in Fig. 2.4).   is the real component of refractive index of the slab waveguide element and   is the *effective* refractive index of the entire waveguide.
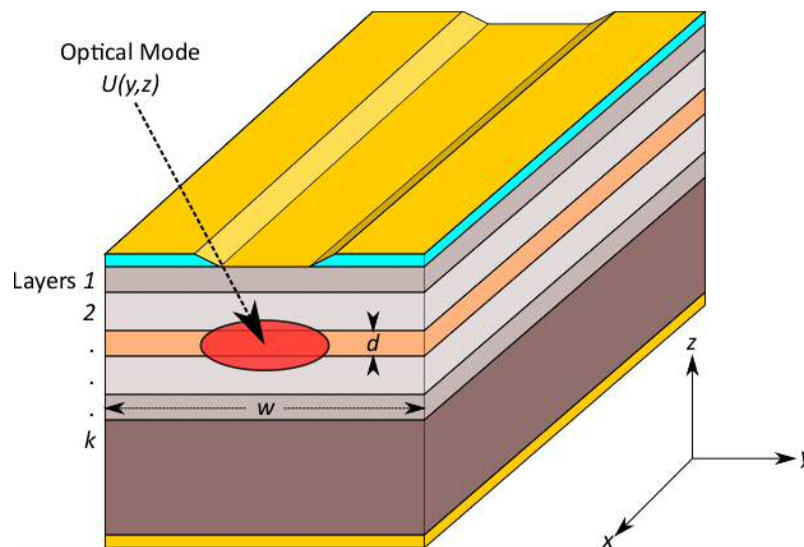
Figure 2.4 Absorption of optical mode propagating through BA laser

The mode,   , may be solved using mode matching methods given the complex refractive indices and geometry of the waveguide (typically carried out by optical mode solving software). The imaginary component,   , of the complex refractive index (as defined by   ), is given by:

$$\underline{\hspace{2cm}}$$

where   is the *vacuum* wavelength of the mode, and   the experimentally determined attenuation coefficient at the specified wavelength.

As well as determining the optical mode profile   , mode matching methods necessarily determine the *effective complex refractive index* of the mode. The imaginary component of which may be used to determine the effective overall attenuation,   , using Eq. 2.8. Arguably, this removes the need to apply Eq. 2.6 & 2.7 to determine   , however these equations remain useful for determining the contribution to optical loss from each layer.

2.3.1 Impact upon Laser Performance

The impact of α_i on device performance may be understood from its contribution to the threshold modal gain condition:

$$\frac{\quad}{\quad} \qquad \frac{\quad\quad}{\quad\quad}$$

The threshold modal gain,   , condition sees laser action occurring as the gain approaches the total cavity loss,   . The mirror loss of a Fabry-Perot cavity laser with cleaved facets may be determined from the mirror reflectivities,   and   , and cavity length,   . A decrease in   reduces the current density required to achieve the threshold gain.

The impact of   on above-threshold optical power may likewise be observed from its impact on the optical output from the facets of the device (derivation in (Coldren and Corzine, 1995)):

$$\frac{\quad\quad\quad}{\quad\quad\quad} \qquad \frac{\quad}{\quad}$$

The output power, P_0, from the facets above threshold is expressed as a function of the internal differential injection efficiency of carriers, n_i, the light extraction efficiency term, ──── , and the energy per photon, *hv*. This relationship describes the *above-threshold slope efficiency* of the laser.

From the light extraction efficiency term we see an increasing dependence upon   with decreasing   . This is typical of lasers with longer cavity lengths (i.e. greater than 3mm) or higher facet reflectivities, such as in high-power laser diode applications. The light extraction efficiency plotted as a function of the ratio ── demonstrates this (Fig. 2.5).

Light Extraction Efficiency (%)

α_i/α_m
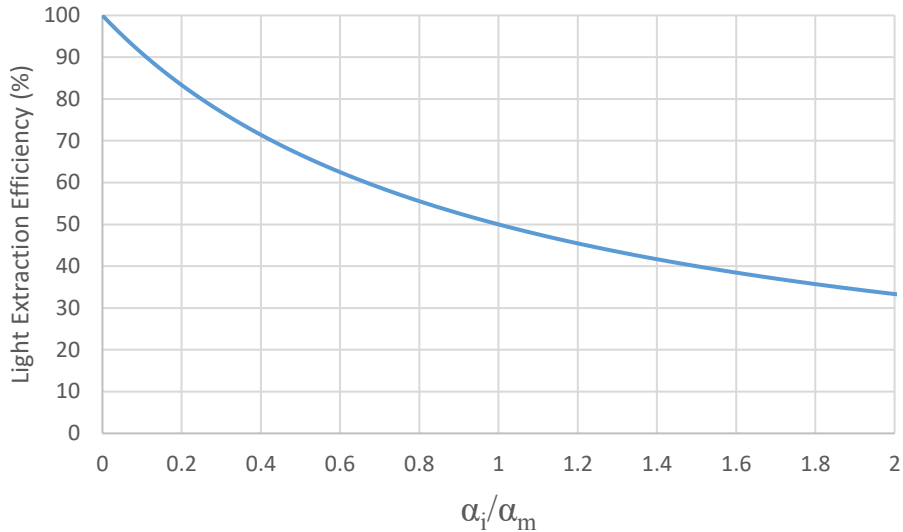
Figure 2.5 Modelled light extraction efficiency with respect to the ratio of cavity losses

Let us consider the general case of a 2mm long BA laser with uncoated, cleaved facets. Where the waveguide is predominantly made up of GaAs and AlGaAs, the air:semiconductor interface will introduce a reflectivity at each facet of ~0.32, and consequently a value of   of about 5.7cm^{-1}. We note from this that a variation in   across the range of values from 1.0 to 0.0cm^{-1} will lead to a change in extraction efficiency of approximately 15%, with over 1% for each incremental change of 0.1cm^{-1}. Improvements of the order of 1% are recognised as being of high commercial value for high power laser diodes (Crump et al., 2013), hence improvements in   of as little as 0.1cm^{-1} are significant.

In high-power laser diodes, values of   as high as 10W can be expected from single emitters. The fraction loss of this large optical power (of the order of 10%, or 1W) as optical mode loss must be accounted for. Given that the mechanisms contributing to   do not contribute additional carriers to the device; nor do we expect this optical power to be emitted out of the cavity; we must assume the optical power loss is retained within the cavity and dissipated by phonon relaxation. With device parameters reported for high-power laser diodes by Crump et al. (Crump et al., 2013), this would be of the order of 0.5W in the absorbing layers. Unfortunately the contributions to device heating from   are not well explored. However, if we follow this line of reasoning, reductions of   may also lead to a reduction in device heating and improved continuous wave performance (e.g. reduced roll-off of power due to device heating).

We also note that where active cooling is used to maintain a stable device temperature then the overall *wall plug* efficiency could be improved, as the heat load upon the cooling mechanism (e.g. thermoelectric cooler) will be reduced.
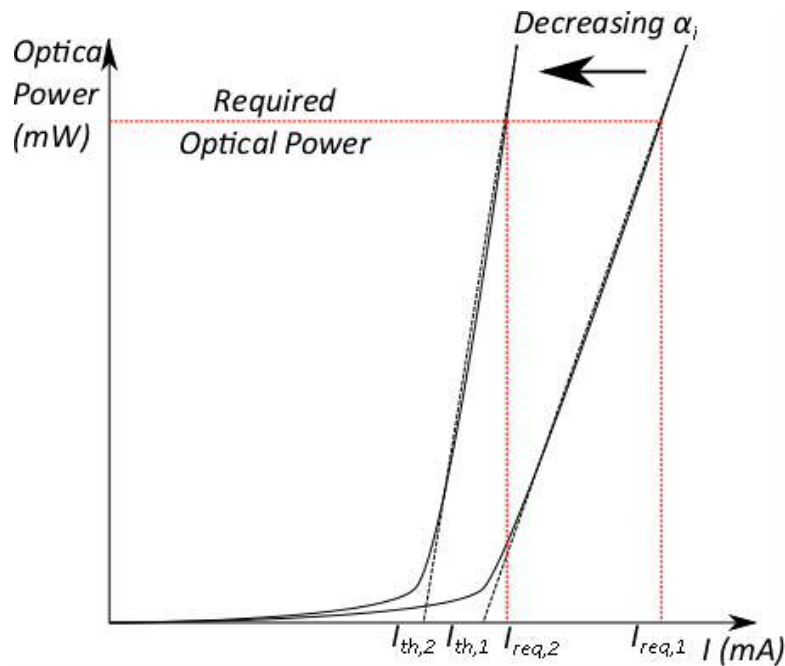
Figure 2.6 Typical impact of reduction in   upon measured light-current (L-I) and required current for constant optical power

As a result of the above described effects, we may expect an improvement in both the threshold current density and the above-threshold slope efficiency with decreasing   (Fig. 2.6). For the purposes of achieving low threshold devices, we note that the reduction of   is crucial where the gain medium provides only very weak levels of gain. However, in high power laser applications, where the intention is to operate lasers at currents many times above their threshold level, both a small reduction in threshold current and the increase in slope efficiency contribute to superior wallplug efficiency.

2.3.2 Absorption Mechanisms

Absorption of light by semiconductor material takes many forms. Those most frequently encountered in laser diodes include transitions between the conduction and valence bands, interactions with free carriers and scattering from the waveguide. At photon energies greater than the minimum bandgap of the laser heterostructure, band-band absorptions dominate the absorption spectrum. At photon energies below the minimum bandgap these transitions cannot occur and we

are left with the remaining in-band transitions (discussed in Section 2.3.3) and light scattering mechanisms.

As band-band absorptions necessarily occur at the lasing wavelengths of QD based devices they will be observed in addition to the optical mode loss in measurements of modal absorption and loss of *unpumped* material (Section 3.4.0), as seen in Fig. 2.6. When this material is pumped however, this absorption gives way to an amplification of light. Provided there is no unpumped material within the device during operation, the additional band-band absorption observed in the measurement will not contribute to the optical losses of the material.

As a result we can draw a distinction, between these two contributions, in measurements of modal absorption and loss. We define the modal absorption due to band-band absorptions as   in such spectra, and contributions to the modal loss as   . We regard both contributions as being present at wavelengths where band-band absorptions occur, while below the band-edge only   is observed. Hence we may use the values of   measured below the material band-edge to infer its value at the lasing threshold.
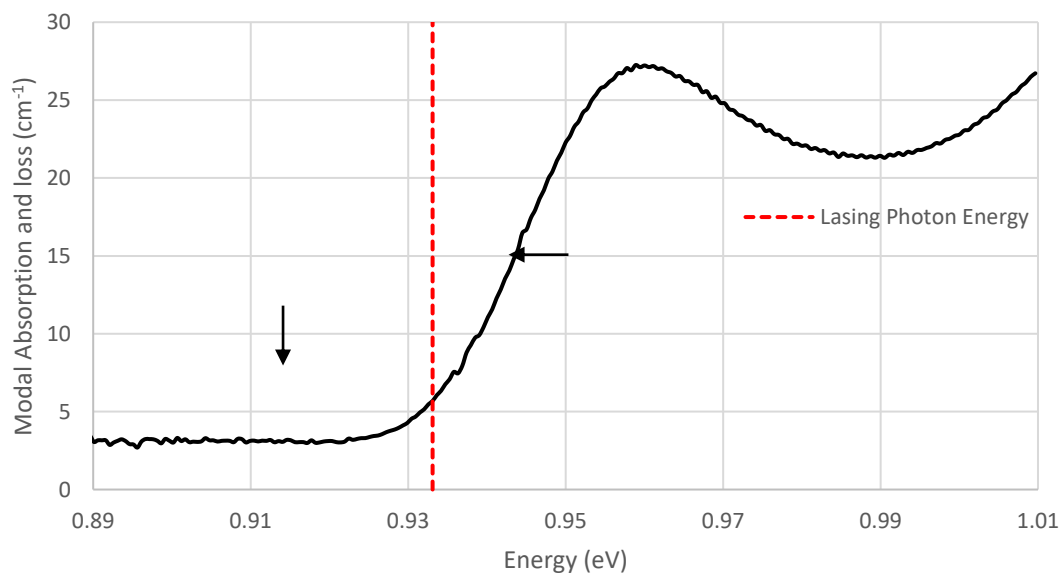
Figure 2.6 Example modal absorption and loss spectra, where contributions to absorption from only are observed at lower photon energies

2.3.3 Free Carrier Absorption, Intervalence Band Absorption and Interconduction Band Absorption

Free carrier absorption (FCA) is regarded as the absorption of light by carriers which are freely moving within their medium. As described by the Drude-Lorentz model, these carriers are said to experience no restoring forces from the medium they propagate through when interacting with an electric field. Such systems that we encounter include metals (containing a high density of free electrons) and doped semiconductors (where n-type and p-type materials allow for large populations of free electron and hole densities respectively).

For the purposes of this work, we will assume the optical mode is sufficiently confined that contributions to   from the top and bottom gold contacts of the laser can be ignored, and consider the FCA of semiconductor material only.

The Drude-Lorentz model can be applied to the electron and hole carriers of a semiconductor for the purpose of calculating their absorption (Fox, 2001) to give the expression:

$$\rule{3cm}{0.4pt} \cdot \rule{1cm}{0.4pt}$$

Equation 2.11

where   is the carrier density (contributed to by dopants and injected carriers), *e* their charge,   their effective mass,   the electric permittivity of free space, *n* the refractive index, *c* speed of light,   the momentum damping period of the carrier,   the absorbed photon's frequency and   a constant with values typically between 1.5 and 3.

For n-type material, free carriers occupying states below the Fermi level can be excited into higher unoccupied states (Fig 2.7). However, to conserve momentum, scattering by phonons or interactions with impurities are also required (Fig. 2.7). In the classical Drude-Lorentz model, the original value for   in the ⎯ dependence is determined to be 2, however this does not account for a dependence in   upon the phonon scattering process. Depending on the dominant scattering processes,   can take on values between 1.5 and 3.5. These processes include acoustic phonon scattering (=1.5), optical phonon scattering (=2.5), and scattering from ionised impurities (=3 or 3.5) (Pankove, 1975). For example, in n-type GaAs with carrier concentration of at least 1×10^{17}, a

value of 3 is observed due to the dominance of impurity scattering proposed by Willardson and Beer (Willardson and Beer, 1967).
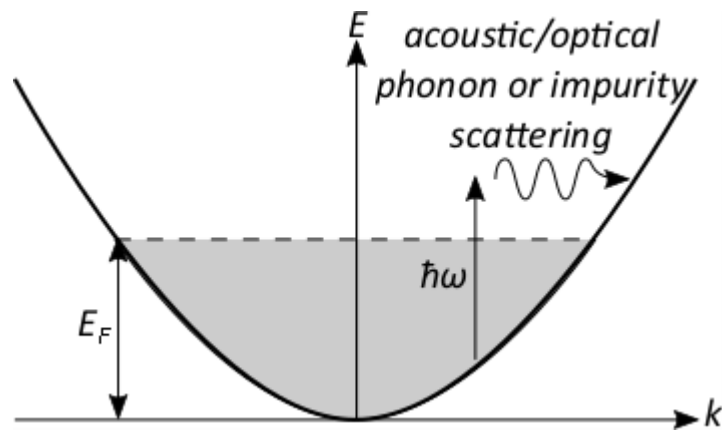
Figure 2.7 Scattering assisted free carrier absorption in the conduction band: carriers below the Fermi energy (defined by the doping density) transition to a higher lying unoccupied state if assisted by a scattering event

From Fig 2.7 and Eq. 2.11, it would appear that contributions to FCA from n and p-type dopants only vary with respect to the effective masses of the carriers, the momentum damping of the medium and the dominant scattering mechanism; however other in-band transitions are possible.

For example, absorption measurements of n-type GaAs by Spitzer and Whelan (Spitzer and Whelan, 1959) demonstrate reasonable agreement with the Drude-Lorentz model at long wavelengths (in excess of 3µm). Within the range of 1-3 µm however an approximately constant value of absorption is observed with respect to wavelength. This departure from the model is due to the presence of *interconduction band absorption* (ICBA), where electrons from the direct band valley also transition to higher lying valley states.

P-type material may exhibit the absorption predicted by the Drude-Lorentz model (i.e. scattering assisted transitions of holes from states above the Fermi energy to below), however we must also allow for direct transitions through *intervalence band absorption* (IVBA). Here transitions do not require the assistance of phonon scattering, as they transition directly between the light hole, heavy hole and split-off bands. Due to the lack of dependence on phonon and impurity scattering processes, IVBA is thought to dominate contributions to optical mode loss in diode lasers, and attempts to optimise waveguide design consequently seek to minimise IVBA first.
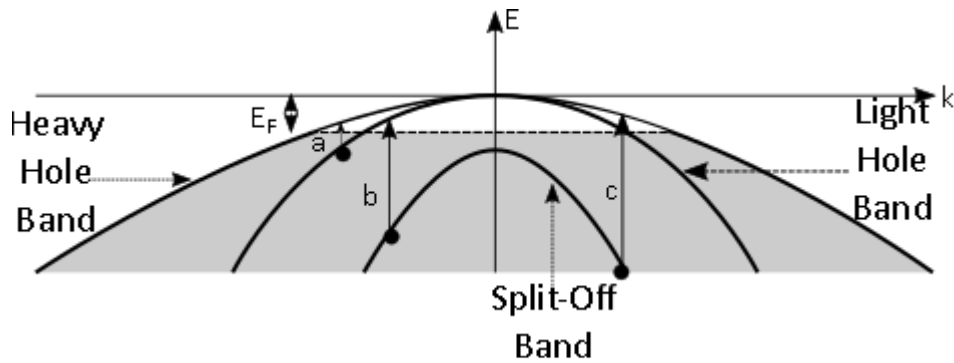
Figure 2.8 Intervalence band absorption: electrons directly transitioning between a) Light hole and heavy hole bands, b) split-off and light hole bands and c) split-off and light hole bands. The transitions due to c) will dominate at higher photon energies.

Due to the three possible transitions (Fig. 2.8) peaks may be discerned in the absorption spectra at the wavelengths at which each transition becomes possible (Pankove, 1975), albeit at wavelengths far below the material band gaps explored in this work. In GaAs, the large energy gap between the uppermost bands (which may vary with the introduction of strain and quantum confinement) and the split-off bands has been shown to give a small contribution to IVBA at short wavelengths (~1.3μm). This IVBA increases exponentially with wavelength as it approaches the split-off band energy difference (0.34eV, equivalent to a wavelength of about 3.6μm) (Henry et al., 1983).

The active region of the device is nominally undoped (although some small background doping during the growth of these layers is often unavoidable), but free carriers will also be found here due to the flow of carriers during device operation. During operation, this will be equal to the threshold carrier density, contributed to by both holes and electrons. These carriers will in turn obey the same physics as described for the doped material, but allowing for the absence of doping impurities to contribute to phonon assisted FCA. Provided the carrier density in the laser pins for currents above threshold, contributions to   from FCA, ICBA and IVBA should remain constant.

2.3.4 Example Strategies for Reducing α_i

Experimentally, the discussed wavelength dependence of FCA, IVBA and ICBA could be used to determine which carriers give the biggest contribution to the overall value of   . For example, an exponential increase in absorption with wavelength would be indicative of strong IVBA. This analysis however would be complicated due to the *modal* contributions of all waveguide layers. Additionally, dispersive relations of the waveguide guiding could also contribute to a wavelength dependence. Comparison of experimental data with a complete model of the expected modal loss (see Section 2.3.0) would become necessary.
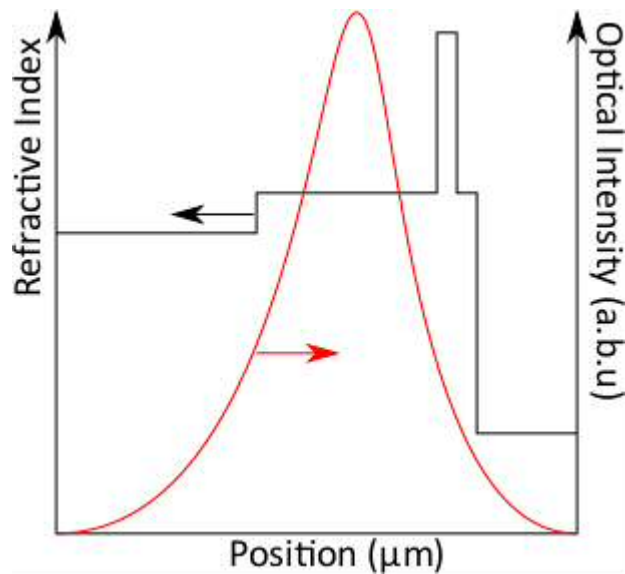
Figure 2.9 Extreme double asymmetric waveguide design impact upon optical mode overlap with p-type cladding (right hand side)

Once a large contribution towards the value of ⬚ is identified, for example from the IVBA due to hole carriers, we may consider measures for reducing its impact. One method of reducing the impact of p-doped material, where the hole densities are significantly higher, is to minimise the overlap of the optical mode with these layers. One approach (investigated experimentally by Buda et al. (Buda et al., 1997) for devices lasing at 826nm) is to change the symmetry of the waveguide such that the overlap of the optical mode with the strongly absorptive p-type cladding is reduced. Theoretical calculations suggest that this approach would be particularly advantageous in lasers emitting at telecommunications wavelength (Ryvkin and Avrutin, 2004). It was also successfully employed more recently in "extreme double asymmetric", EDAS, waveguide designs (Fig. 2.9) in high-power lasers emitting at 940nm from InGaAs QW structures (Crump et al., 2013).

In EDAS structures, the waveguide thickness of the n-type cladding is increased, the index step change with the p-type guide increased (by increasing the p-type cladding Al content) and its width decreased. The resulting optical mode is highly asymmetric, in favour of a smaller overlap with the p-type material. Improvements in external differential efficiency consistent with reduced ⬚ were shown, demonstrating the importance of IVBA in p-type material in these structures. The electrical resistance from the p-side contact was also vastly reduced, leading to better internal efficiency. However, this was at the cost of increased threshold current due to a large reduced overlap of the optical mode with the active region. These investigations into asymmetric waveguides demonstrate the importance of optimisation of waveguide design for improved differential efficiency.

Where both n and p-type dopants are believed to be responsible, the thickness of the undoped core of the waveguide may be increased to reduce overlap with the doped cladding regions, while the symmetry of the solution maintains the best possible overlap of the optical mode with the gain medium. The disadvantage here is the increased electrical resistance of the diode, which leads to a higher power dissipation as device heating, but also a decrease in the overlap of the optical mode with the central gain medium (see Section 6.2).

As FCA, IVBA and ICBA are proportionate to the number of free carriers present, another approach to reducing   is to grade the doping profile, particularly with respect to the p-type cladding. As the overlap of the optical mode with the cladding decreases with distance from the centre of the waveguide, a larger doping density at longer distances from the centre of the waveguide can be afforded when optimising for reduced   . Again, this approach must be balanced against the resulting increase in electrical resistance with decreasing dopant concentration. In (Slipchenko et al, 2004), ultrawide waveguides (1μm) for quantum well lasers operating at 1.08μm are used to achieve a very low optical mode loss value of 0.34cm^{-1}, although the precision to which this was found is questionable (see discussion in Section 1.1).

ALFEROV, Z. 2000. Double heterostructure lasers: early days and future perspectives. *IEEE Journal of Selected Topics in Quantum Electronics,* 6**,** 832-840.

ARAKAWA, Y. & SAKAKI, H. 1982. Multidimensional quantum well laser and temperature dependence of its threshold current. *Applied Physics Letters,* 40**,** 939-941.

BLOOD, P. 2015. *Quantum confined laser devices : optical gain and recombination in semiconductors*, Oxford : Oxford University Press.

BUDA, M., ROER, T. G. V. D., KAUFMANN, L. M. F., IORDACHE, G., CENGHER, D., DIACONESCU, D., PETRESCU-PRAHOVA, I. B., HAVERKORT, J. E. M., VLEUTEN, W. V. D. & WOLTER, J. H. 1997. Analysis of 6-nm AlGaAs SQW low-confinement laser structures for very high-power operation. *IEEE Journal of Selected Topics in Quantum Electronics,* 3**,** 173-179.

COLDREN, L. A. & CORZINE, S. W. 1995. *Diode Lasers and Photonic Integrated Circuits,* New York, Wiley.

CRUMP, P., ERBERT, G., WENZEL, H., FREVERT, C., SCHULTZ, C. M., HASLER, K. H., STASKE, R., SUMPF, B., MAAßDORF, A., BUGGE, F., KNIGGE, S. & TRÄNKLE, G. 2013. Efficient High-Power Laser Diodes. *IEEE Journal of Selected Topics in Quantum Electronics,* 19**,** 1501211-1501211.

DEPPE, D. G., SHAVRITRANURUK, K., OZGUR, G., CHEN, H. & FREISEM, S. 2009. Quantum dot laser diode with low threshold and low internal loss. *Electronics Letters,* 45**,** 54-56.

EAGLESHAM, D. J. & CERULLO, M. 1990. Dislocation-free Stranski-Krastanow growth of Ge on Si(100). *Physical Review Letters,* 64**,** 1943-1946.

FOX, M. 2001. *Optical Properties of Solids,* New York, Oxford University Press.

HENRY, C., LOGAN, R., MERRITT, F. & LUONGO, J. 1983. The effect of intervalence band absorption on the thermal behavior of InGaAsP lasers. *IEEE Journal of Quantum Electronics,* 19**,** 947-952.

LIU, G., STINTZ, A., LI, H., MALLOY, K. J. & LESTER, L. F. 1999. Extremely low room-temperature threshold current density diode lasers using InAs dots in In$_{0.15}$Ga$_{0.85}$As quantum well. *Electronics Letters,* 35**,** 1163-1165.

MI, Z., YANG, J., BHATTACHARYA, P. & HUFFAKER, D. L. 2006. Self-organised quantum dots as dislocation filters: the case of GaAs-based lasers on silicon. *Electronics Letters,* 42**,** 121-123.

MI, Z., YANG, J., BHATTACHARYA, P., QIN, G. & MA, Z. 2009. High-Performance Quantum Dot Lasers and Integrated Optoelectronics on Si. *Proceedings of the IEEE,* 97**,** 1239-1249.

PANKOVE, J. I. 1975. *Optical processes in semiconductors,* New York, New York : Dover.

RYVKIN, B. S. & AVRUTIN, E. A. 2004. Improvement of differential quantum efficiency and power output by waveguide asymmetry in separate-confinement-structure diode lasers. *IEE Proceedings - Optoelectronics,* 151**,** 232-236.

SPITZER, W. G. & WHELAN, J. M. 1959. Infrared Absorption and Electron Effective Mass in n-Type Gallium Arsenide. *Physical Review,* 114**,** 59-63.

WILLARDSON, R. K. & BEER, A. C. 1967. *Semiconductors and semimetals. Vol.3, Optical properties of III-V compounds,* New York ; London, New York ; London : Academic Press.

S. O. SLIPCHENKO, D. A. VINOKUROV, N.A. PIKHTIN, Z. N. SOKOLOVA, A. L. STANKEVICH, I.S. TARASOV, ZH. I. ALFEROV. Ultralow Internal Optical Loss in Separate-Confinement Quantum-Well Laser Heterostructures. *Physics of Semiconductor Devices,* Vol 38, Issue 12, pp1430-1439.

Chapter 3   Experiment Methodology

3.1   Introduction

Here we will discuss in detail the established methodology for the characterisation of broad area lasers used in this work. We begin by summarising the fabrication of broad area lasers and segmented contact devices (Section 3.2). We then briefly describe the commonly known characterisation methods, including measurement of voltage-current-light output characteristics as well as device nearfield profile (Section 3.3). The theoretical underpinnings of these experiments are explored fully in works such as (Coldren and Corzine, 1995) and (Blood, 2015).

Measurements of the modal gain, absorption and loss by the single-pass segmented contact method (SCM) (Section 3.4) are less well established. This method forms the focus of much of this work, and a full treatment for the motivations behind its use (i.e. the shortcomings in other methods of measuring   ); its theoretical underpinnings; and our experimental methodology are provided here. We will also describe how shortcomings in this method may be overcome by a modulated approach to the SCM.

3.2   Device Description and Fabrication

Here we will summarise the fabrication process followed by colleagues to produce broad area (BA) lasers. The additional fabrication steps required for producing segmented contact devices will be described later as part of our discussion of the SCM experiment methodology, with some references to this material.

Unless otherwise stated, devices investigated in this work are fabricated from material consisting of an active region of 3 layers of InAs quantum dots, each within InGaAs quantum wells and separated by GaAs spacer layers, expected to achieve laser action at 1.3μm. Confinement in the growth direction is achieved by AlGaAs cladding layers, surrounded by additional layers of GaAs. All of which is grown onto a GaAs substrate. Compositional and layer thicknesses will be discussed as and where relevant.

A small area of material (2-4cm^2) is separated from the parent wafer and then cleaned in heated solvents in preparation for fabrication. Next an electrically resistive layer of silicon dioxide (SiO$_2$) is deposited onto the exposed semiconductor surface.

As the central stripe of BA lasers is large (50µm wide), photolithography is sufficient to define the etching dimensions of the SiO_2 (Fig. 3.1). This is performed by the deposition of a positive tone photo-resist, which when exposed to patterned light, may be selectively dissolved by solvents to leave 50µm wide channels in the photo-resist material where we wish to etch the SiO_2. These channels are formed perpendicular to the (110) crystal plane to ensure the contact stripe is perpendicular to the cleaving plane of the facets.
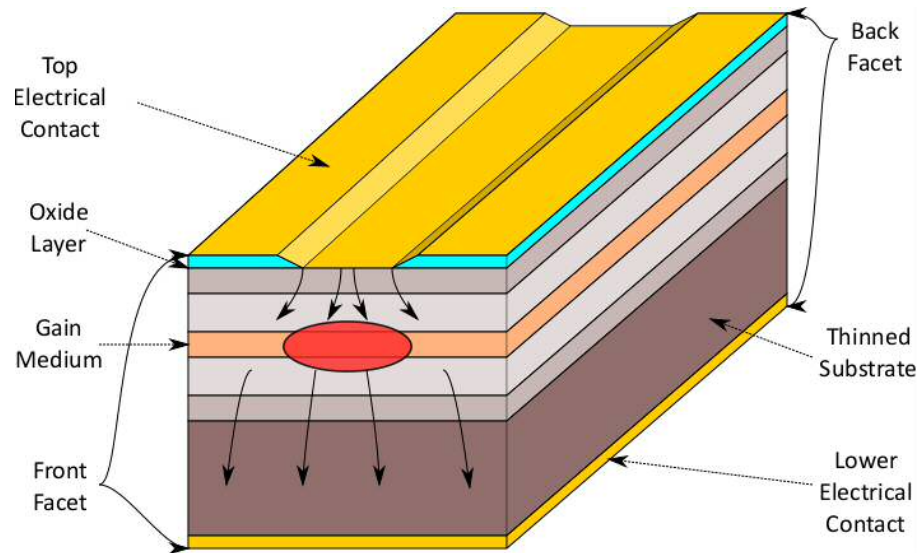
Figure 3.1 BA laser illustrating the emission of light from the facet (not to scale)

Once the SiO_2 channels are etched, solvents for the removal of unexposed resist are used to remove the remaining photoresist. Metallisation of the top and lower contacts may now begin.

Metals for evaporation onto the semiconductor surface must be matched both for dopant and semiconductor material. For the top p-type GaAs material a zinc and gold alloy provides both sufficient adherence to the semiconductor surface and a good ohmic contact (i.e. a contact which is purely resistive in behaviour).

Metallisation of the n-type side (lower contact) is preceded by lapping of the substrate layer. The thinning of the material is necessary for the later described cleaving process. The reduced device thickness also aids in the extraction of heat from the device active region (GaAs has poor thermal conductivity). Over-thinning of the substrate can lead to strain induced deformation of the device. As a general rule, the overall device thickness after thinning will be 80-120µm.

The metallisation of the lower contact is more complex due to the difficulty in forming a good ohmic contact with n-type GaAs. A gold and germanium alloy is used to make an initial good ohmic contact with the substrate, while an additional layer of nickel is used to prevent "balling" of the

surface material. A final layer of gold is then applied by evaporation to help form a good electrical contact with the copper blocks or gold plated transistor headers used in testing.

At this point the small area of material is cleaved into multiple laser devices. The length of the BA lasers is defined by cleaving along the (110) plane of the material. This is achieved by forming a small defect at the edge of the sample material (using a scribe tool) and applying pressure to the material, such that a clean break in the material forms along the (110) plane. Because this break is formed by the propagation of a break along a crystallographic plane, the surface is mirror-like and nearly atomically perfect. The length of BA lasers may be varied by changing the position of this cleave.

Devices are separated by scribing the material at the mid-point between the 50μm contacts and applying pressure to form a break. This results in a rough surface along the length of the devices. This is helpful for suppressing lasing modes running perpendicular to the intended direction of the device.

BA laser devices of multiple possible lengths can be formed. We will typically use 1, 2, 3 and 4mm devices in this work. At this point samples are handed from a fabrication expert to myself to carry out subsequent sample preparation steps.

I selected BA lasers for testing based on the quality of their facets and metallisation of the top and bottom contacts, as apparent when observed through an optical microscope. The bottom (n-type) contact of the device is secured to copper blocks, which are secured to a transistor header, using silver conductive epoxy. This epoxy ensures reasonable thermal and electrical contact between the device and the transistor header for the purposes of heat extraction and cooling. The device may be placed perpendicular to, or in the plane of, the transistor header to suit the needs of the experiment.

Pins of the transistor header are epoxied at approximately the centre of the top contact using gold wire and silver epoxy, manipulated into place by hand with the aid of an optical microscope. In general only one wire is used, however multiple wires may also be placed to aid in heat extraction. The silver epoxy is cured between mounting steps using a hot plate to secure elements in place during the mounting process.

3.3.0 Laser Characterisation Techniques

3.3.1 Current-Voltage-Light (I-V-L) Measurement

In this experiment the current, voltage and light (I-V-L) characteristics of a BA laser device may be measured simultaneously to assess the quality of electrical contacts on the device, or measure the lasing threshold current and above-threshold slope efficiency.

I have the option of performing this experiment using a continuous or pulsed current supply. Continuous current (known commonly as continuous wave or CW) is the most commonly used mode of operation for laser devices, however it will also generate heating in the active region of the device. For currents sufficiently high above threshold, this will tend to cause a "roll-off" effect in the L-I characteristic. Such measurements are useful for determining performance of devices in the context of their applications, however heating effects also cause the measurement of above-threshold slope light-current relationship to deviate from a linear trend. This complicates the measurement of above-threshold slope efficiency and linear extrapolation of threshold current density.

As a result, unless we intend to assess heat effects in this mode of operation, it is convenient to measure the I-V-L characteristic using a pulsed current source. For low duty cycles, this reduces the net heating of the device substantially, minimising changes in device behaviour with increasing current. We describe the duty cycle used in devices on an experiment-by-experiment basis.

A pulsed constant-current source is passed through a potential divider controlled by a stepper motor which determines the applied voltage to the device. The resulting current and voltage to the device are read out to a computer via an A to D card.

Light is measured by directing the front facet emission onto a reverse biased, large area photodetector (which is sensitive to the expected lasing wavelength of the device) and measuring the resulting photocurrent. This photocurrent is also measured by the boxcar integrator. The resulting measurement is given in arbitrary units against current, or L-I. This may be used to determine the threshold current of the device (see Section 2.3.1)

Provided the lasing wavelength of the device is known, light emission from the BA laser may be measured in real units by a wavelength calibrated integrating sphere, which provides a *time averaged* measurement of the pulsed light. The optical power measured from the front or from both facets (dependent on device orientation) above threshold is measured as a function of current (a P-I

measurement). This may be used to determine the threshold current and, correcting for the duty cycle of the current source, above-threshold slope efficiency (Section 2.3.1).

The I-V characteristic is useful for determining the quality of the device contacts, the response of which should be diode like in appearance. It is also used to check for identical electrical behaviour between the top contacts of segmented contact devices for SCM (Section 3.4.3).

3.3.2 Nearfield

The nearfield of a device describes the emission profile of light at the facet of a device, and is a useful tool for observing the quality of BA and segmented contact devices. It may be used to identify imperfections in the facet quality and the waveguide (see also Section 3.4.4), as well as the effects of filamentation in lasing devices. It is measured by focusing an image of the front facet of the device onto a photodetector array sensitive to the expected emission spectrum.

In addition to quality analysis, the lateral spreading of current from the top contact (illustrated in Fig. 2.1) may be determined by measuring the full width half maximum (FWHM) of the image, provided only *unamplified* light is measured. This is achievable using band pass filters which restrict the imaged nearfield to wavelengths from the weakly amplified light from relatively long wavelength emission of the device. Alternatively, the nearfield may be spectrally resolved (Section 3.4.5). The FWHM dimension may be converted from width in pixels to real units by comparison with an image containing measurable dimensions of the device (e.g. facet width), obtainable by reflecting light from a lamp source off the device facet.

3.4.0 The Segmented Contact Method (SCM) for the measurement of modal gain, absorption and loss

The focus of this work is in applying SCM to the precise measurement of internal optical mode loss, . However, the SCM does not represent the only method for the measurement of , therefore I will begin with a brief account as to why I have used this method with reference to the shortcomings of the more commonly used methods.

3.4.1 Motivations

I believe the external differential quantum efficiency (DQE) method is the most commonly used approach for the measurement of . In this method, the above-threshold slope efficiencies of multiple devices of varying lengths are measured, and a linear relationship between the reciprocal of the DQE, $-$, and the reciprocal of the mirror loss, $-$, may be used to determine both the internal differential quantum efficiency, , and   (see Eq. 2.9). This method's wide spread adoption is readily understood from an experimentalist's point of view; the method uses simple to fabricate laser devices, where only the length is varied, and the measurement of the above-threshold slope efficiency is a widely practiced characterisation method (Section 3.3.1).

However, disadvantages in the DQE method make it unsuitable for the *precise* measurement of . Firstly, the measurement is taken across multiple devices. This introduces scatter into the linear relationship between $-$ and $-$ due to variations in the facet reflectivity and series areal resistance of devices (which are in turn due to variations in the quality of the cleave and metallisation of contacts or device mounting respectively).

Variability in device quality may be reduced by fabricating large sets of lasers for each length measured, and selecting the best performing devices from each set (i.e. the lowest threshold current and/or highest slope efficiency). Assuming the best performing lasers correspond with approaching ideal device perfect conditions, then a complete set of devices approaching similar, "perfect" quality should be obtained and the scatter consequently reduced. Additional scatter in the measurement of above-threshold slope efficiency has also been observed (Crump et al., 2013), introduced by uncertainties inherent in the coupling of laser emission with the detector and sensitivity of the device to changes in temperature and reflected light.

Even by accounting for the above uncertainties, the *accuracy* of the DQE method is not ensured. The DQE method assumes complete Fermi level clamping above threshold (Smowton and Blood, 1997), an effect which can be exacerbated in QD systems (Blood, 2015). The presence of drift leakage also leads to the external differential efficiency having a dependency on current, and therefore device length. This departure from linearity is frequently observed in the literature, including (Crump et al., 2013).

We may also consider applying the Hakki-Paoli method (Hakki and Paoli, 1975) for the measurement of modal gain and loss from the contrast of the longitudinal modes of a laser operated

at below-threshold current conditions. This method has seen frequent use also, and may be readily applied to BA lasers; although shorter cavity lengths (<1mm) are generally favoured as this will increase the longitudinal mode spacing and so relax the requirement for high spectral resolution.

Disadvantages to the Hakki-Paoli method include the requirement for high quality facets; as this is recognised to be of huge importance to obtaining well defined longitudinal modes. It also requires equipment with sufficient spectral resolution to not only observe these modes (e.g. for a 1mm long cavity of primarily consisting of GaAs (with refractive index of 3.3), the longitudinal mode wavelength spacing is approximately 1.5Å at wavelengths around 1μm) but also minimise the impact due to the convolution of the mode profile with the response function of the detection system. Modifications to this method which help reduce, but not eliminate, the need for high spectral resolution are given by (Cassidy, 1984), (Hofstetter and Thornton, 1998) and (Volet et al., 2016).

Provided the above limits are met a net modal gain spectrum for the laser could be found. Values for   can then be determined from the net modal gain spectrum measured below the band-edge of the laser device, where gain is believed to be entirely absent. The value of   experienced at the *lasing wavelength* of the device would be assumed to be equal to this below band-edge value. However, the emission of light at these below band-edge wavelengths is greatly reduced, which greatly reduces the experimental precision achievable for its measurement.

The segmented contact method (SCM) is introduced in full in (Blood et al., 2003). It can be seen as an electrically pumped analogue to optically pumped stripe length measurements, as they are both single pass measurements of the laser material. However here differences in the length of material where carriers are injected is achieved electrically rather than optically. An additional change is that the stripe length is varied in discrete steps using a test structure with isolated electrical contacts. The resulting amplified spontaneous emission spectrum from the front facet is then compared for different combinations of sections in order to determine the modal gain, absorption and loss spectra for the test structure (Section 3.4.5).

Similarly to the Hakki-Paoli method,   is obtained from the measurement of modal gain and loss or modal absorption and loss characteristics at wavelengths where there is no material gain or absorption respectively. The modal gain and loss measurement suffers from similar disadvantages to those seen in the Hakki-Paoli method, as the emission of light where gain is absent is minimal. The modal absorption and loss however is measured by the emission of light from *pumped* material (i.e.

43

where a voltage is applied) transmitted through *unpumped* material where there is no bias applied. The band gap of the gain medium within a forward biased section will narrow due to Coulomb interactions with the introduction of additional carriers, and consequently the emission band edge of this gain medium is lowered. Emission from this lowered band edge then passes through unpumped material where no such band gap narrowing occurs, thus modal loss just below the band edge of the unpumped material is interrogated with larger ASE.

3.4.2 Fabrication of Test Structures

Test structures for the SCM are fabricated alongside BA lasers, as described in Section 3.2. Electrical isolation of the top contacts is achieved by photolithographic etching of a thin gap (6μm wide) between contacts after the metallisation of the top contact. For material grown on off-axis substrates we may also choose to fabricate the segmented contact devices at an orientation such that the resulting cleave plane is not perpendicular to the direction of the waveguide. This results in atomically flat but angled facets which help to minimise the internal reflection of light at the air-semiconductor interface. This is important as light measured within the SCM should only make a single pass through the structure.

The depth of the etching process is crucial; too little and significant current spreading will occur while too deep an etch will interfere with the optical mode, potentially creating an additional optical loss mechanism in the device. The inter-contact resistance (ICR) between contacts may be measured during the etch process, which is ceased when acceptably high resistance between contacts (at least 200Ω) is achieved.
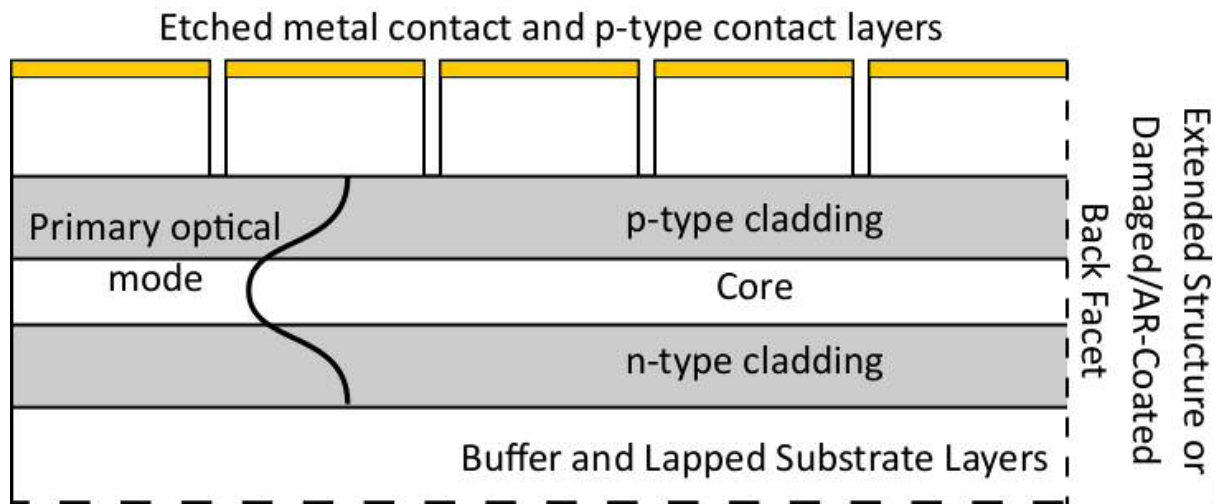
Figure 3.2 Fabrication of top contacts with relation to device layers and optical mode profile

Following this, samples are cleaved to obtain quality facets. While facet quality is not necessary for optical feedback (segmented contact devices are not operated as lasers), striations in the facet may result in the collection of light from the cavity which has followed an optical path unaccounted for by the SCM.

As seen in laser devices the cleaving step is used to determine the length, and number of, complete sections of the device. As a result of uncertainties in the cleaving process, the length of the front and rear sections may differ slightly from that defined by photolithography. Where front and rear sections are used within this method it may be useful to confirm their true length.

The length and facet angle can be varied to optimise the experiment, however in this work we will utilise devices made up of 7 complete contacts, each with lengths of 300µm with 6µm etched separations, and with perpendicular facets (Fig. 3.2).

3.4.3 Sample Preparation

Segmented contact devices are prepared for experimental work by mounting on to a copper block which has been mounted perpendicular to a transistor header using silver conductive epoxy (see also Section 3.2). Multiple wires are attached to the transistor pins for the purpose of changing the configuration of operated sections.
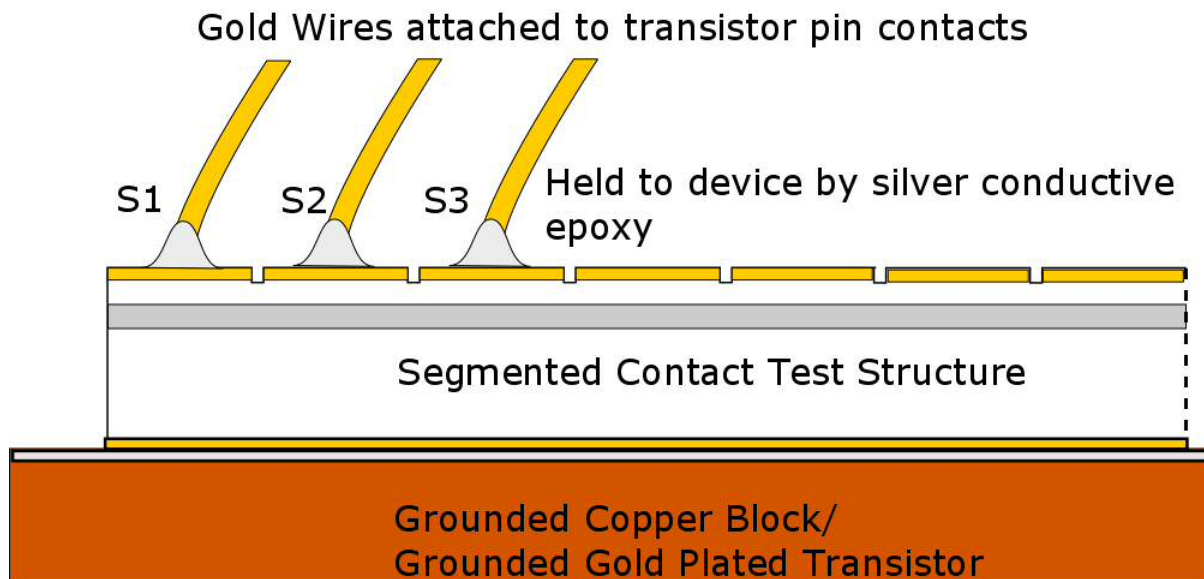
Figure 3.3 Example Preparation of SCM test structure for measurement purposes

The convention used to refer to wired sections is S1, S2….S7, where S1 always refers to the front most section, from which light is collected.

The positions of attached wires may be varied depending on experimental considerations. For example, if there is significant current spreading from the top contacts in the longitudinal direction of the laser (i.e. due to highly doped, shallowly etched top contacts), then sections adjacent to a facet will have a different effective length from the other sections. A comparison of S1 and S2 for modal absorption and loss would therefore be unwise, as this difference in current spreading will lead to non-identical behaviour between the compared sections when operated at the same current. This would be overcome in comparisons of sections S2 and S3. Additionally, the current leakage through adjacent sections may be reduced by grounding the adjacent sections. In this work we will make use of S2 and S3 only, with additional grounded wires attached to S1 and S4.

An additional means for preventing light from making multiple passes in the cavity is to deliberately damage the back facet after mounting (using a scribing tool). Alternatively, anti-reflective coatings may be applied to the facets. In this work we damage the back facets of all segmented contact devices (see Figure 3.2).

3.4.4 Sample Quality Assessment

Mounted samples are first assessed for their electrical contact and optical quality. This is necessary as the modal absorption and loss measurements require compared sections to generate initially identical ASE spectra, which is obtained using identical collection geometry.

As the quality of grown material is expected to be consistent over the small distances between sections (300μm), the ASE generated by each section is expected to only vary with the applied current density and quality of the top contacts. We determine the electronic behaviour of two given sections is identical by comparing their forward-biased current-voltage (I-V) characteristics (Section 3.3.1). Matched section I-Vs are indicative of consistent fabrication (e.g. etching of contact breaks) and mounting quality, and give us confidence in the identical behaviour of the sections.

Small variations in the ICR between sections have been measured (believed to arise from inconsistencies in the etching of contact breaks) and are likely responsible for variations in the measured IVs of sections. The impact of this is minimised by mounting multiple devices and selecting those which exhibit the best matched section IVs. For example, Fig. 3.4 demonstrates IVs matched to within the precision of the I-V-L experiment set-up described in Section 3.3.1. The impact of small differences in IVs in the measurement of modal loss will be observed through testing the repeatability of results between devices in Section 6.4.1.

IV testing may also be used to determine the quality of contacts. Note that in Figure 3.4 there appears to be significant series resistance (indicated by the trend towards a shallow gradient with increasing voltage) within the diode, tending to approximately 5Ω at a value of 1.85V. This is indicative of poor quality top contacts, which may also be linked to variability in the performance between sections in the segmented contact device, as well as potential additional source of heat due to joule heating.
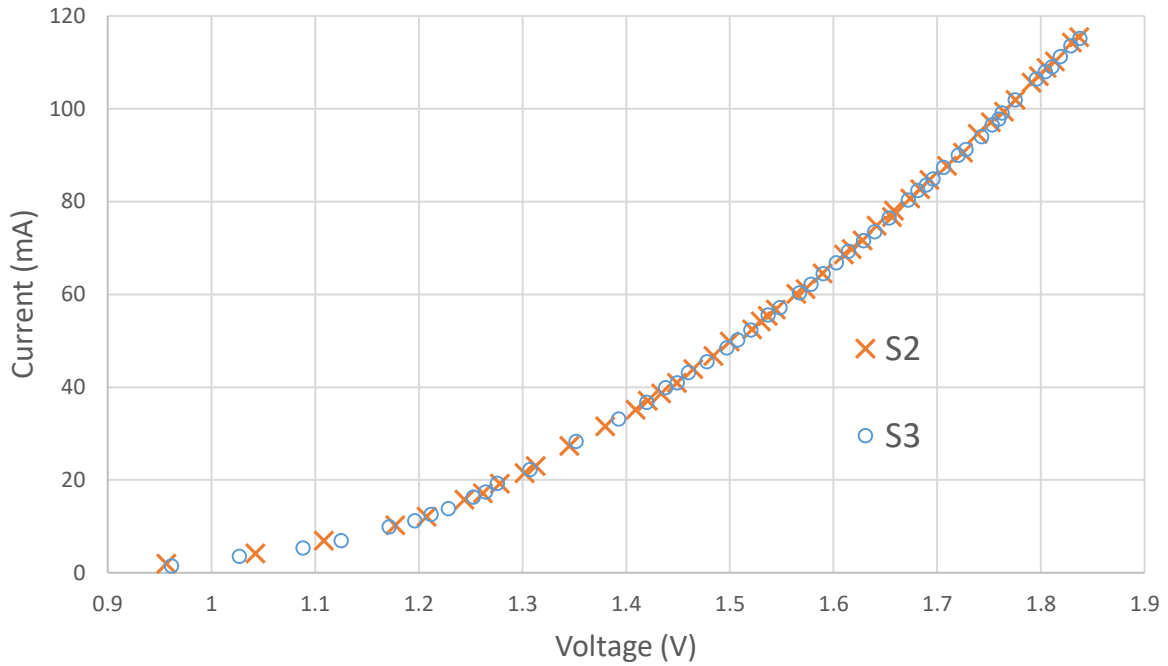
Figure 3.4 Example of well-matched IV characteristics for S2 and S3 contacts of a ridge waveguide segmented contact test structure of InAs QD laser material. Series resistance approximately 5Ω

The quality of the front facet is assessed prior to the mounting of the segmented contact device. Like laser devices, these should appear mirror-like and be free from striations, particularly at the stripe centre and near the top contact. This quality is verified by measuring the nearfield of ASE from the device (Figure 3.5).
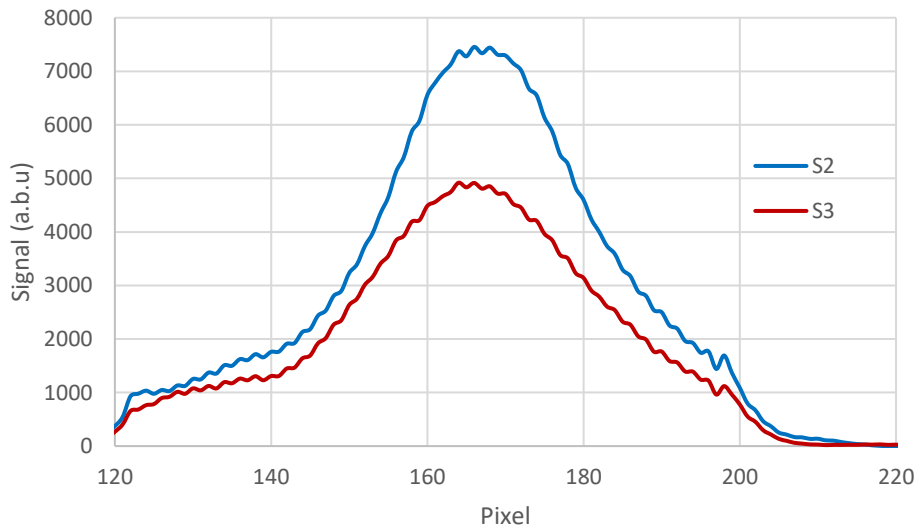
Figure 3.5 Example of consistent nearfields between segmented device contacts S2 and S3, observed with apparatus described in figure 3.7.

The nearfield intensity measured across the facet (i.e. in the plane of the gain medium) when imaged by a camera should have a smooth Gaussian profile, with a peak located at the stripe centre (Section 3.3.2). Small dips in the intensity measured across the facet are frequently observed, and are

commonly due to device residue from cleaving and dust on the surface of the facet. When located near the stripe centre, such defects may significantly interfere with the collection geometry of light. When observed in the nearfield profile, we remove this residue by applying a suitable solvent (e.g. Isopropyl Alcohol) and gently stroking the surface with a soft tool.
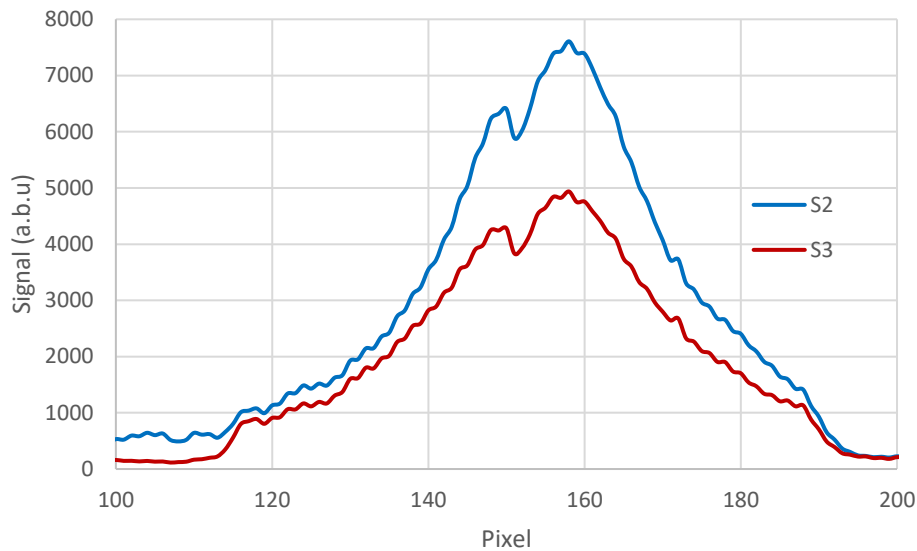
Figure 3.6 Example of segmented contact device with surface defect in close proximity to device centre.

If these dips appear constant despite which section is operated then they are likely due to absorption at the surface of the facet (see Fig 3.6). However, if they vary between the sections we wish to compare, it indicates that the optical mode has been significantly altered during fabrication (e.g. this may occur due to over etching of device features or from "etch-pits" where the etching process has been non-uniform). In this case it is inappropriate to use the device for the segmented contact method.

3.4.5 Standard SCM Experiment

Samples which have passed the quality assessment stage are measured using a spectrometer with a mounted photodiode array camera (Fig. 3.7).

ASE from the sample is focused onto the slits of the spectrometer using a microscope lens with a low numerical aperture. This ensures a narrow collection angle of light from the laser cavity. An adjustable iris mounted onto this lens is used to restrict the collection geometry of the lens further to achieve a collection full-angle width within 10°. This is found to minimise the collection of unamplified light in broad area devices in (Lutti, 2005).
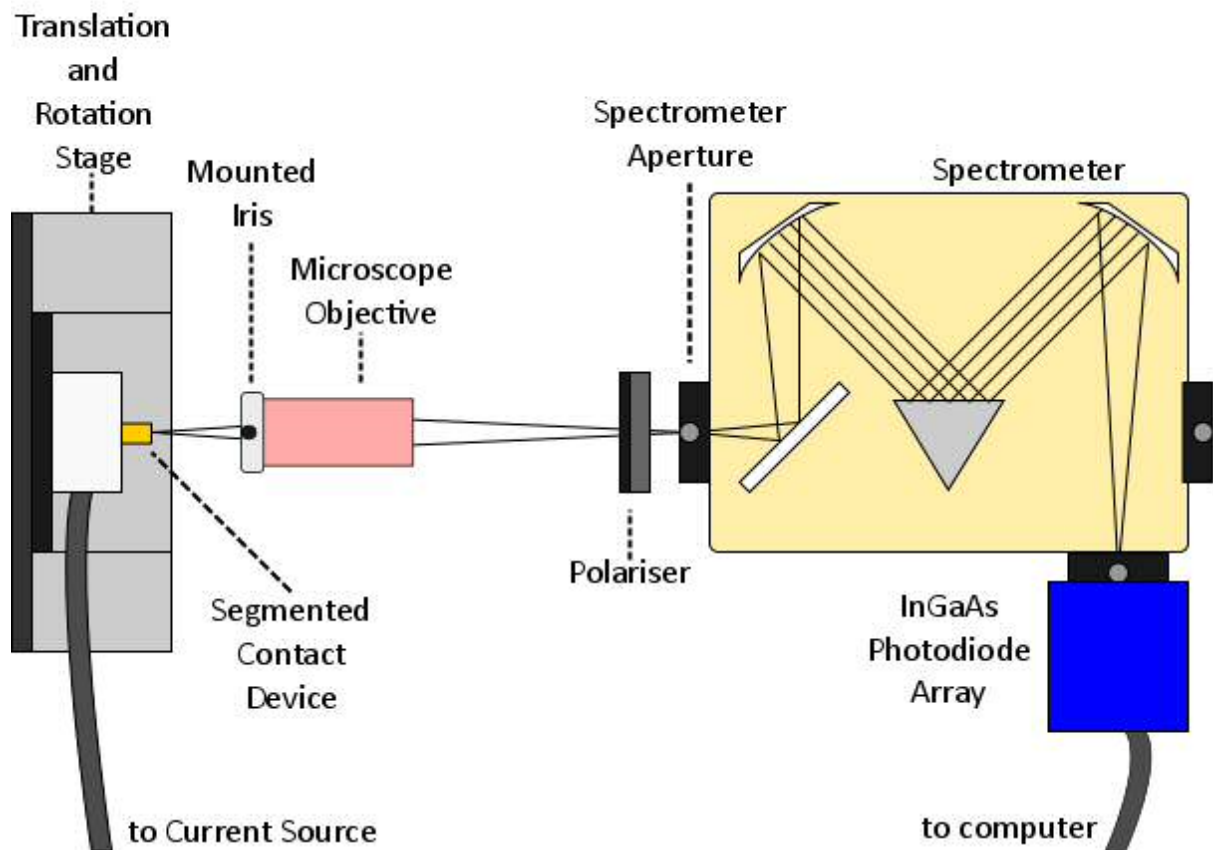
Figure 3.7 Experimental setup for spectrally resolving the ASE from segmented contact test structures (not to scale)

The position of the device's nearfield relative to the spectrometer slits may be determined by setting the spectrometer to its *zeroth* order, and focusing an image of the device at the position of the slits. This allows an undiffracted image of the device nearfield and the slit dimensions to be imaged together. This image is used to orientate the device nearfield perpendicular to and centred on the position of the spectrometer slits. The centre of the contact stripe is found from the peak intensity of the nearfield profile, and the slit dimension is varied to ensure only light from the centre of the stripe is collected. This limits the collection of light reflected from the sidewalls of the device.

Alignment of the device with respect to the microscope lens is controlled by a microtranslation stage with x-y-z translation micrometres, and rotational freedom around the x-y-z axes, giving complete control over sample orientation.

Slit dimension may be used to determine the monochromator's spectral resolution (with narrower slits corresponding with better resolution), however the resolution is ultimately limited by the pixel dimensions. When diffracted by a grating with 1200 lines/mm (blaze wavelength 1200nm) and centred upon 1350nm, the 320x256 InGaAs photodiode array detects light across 246nm, leading

50

to 0.77nm per pixel and an ultimate resolution of 1.54nm (Nyquist theorem requires minimum sampling rate of 2 pixels). By reducing the slit dimension to less than 25µm, we both ensure a narrow collection angle of light from the device and a resolution which is not limited by the slit dimensions. The quoted resolution of spectrometer is 0.25nm, given a slit dimension of 25µm and aperture size, in this case determined by the pixel width, which is also 25µm. Wavelength calibration of the detection system has been previously obtained using the spectral lines of a HeNe laser source.

The different polarisation contributions to gain and absorption may be accessed by passing ASE emission through a polariser in either the transverse electric (TE) or transverse magnetic (TM) position (where the transverse is perpendicular to the growth direction of the laser). This is placed between the lens and monochromator slits, and is necessary for producing modal gain, absorption and loss spectra which are not a convolution of the two polarisations.

When satisfied with the alignment, the modal absorption and loss spectra are obtained by collecting the spectrally resolved light from the device when operating S2 and S3 in succession. Note that the obtained modal absorption coefficients for the unpumped material should be independent of the current density used to operate S2 and S3. Therefore, provided identical behaviour in the current range is expected, it is reasonable to operate these sections with current densities towards the upper limits of the device as the larger ASE will result in a better signal to noise ratio (SNR). We limit this to no more than 1000mAcm^{-2} (pulsed at 5kHz with 1000ns pulse width) as beyond this damage to the top contacts of BA segmented contact and laser devices has been observed.

A dark reading is also taken prior to measurements and later subtracted from the measured ASE. Note there is always a significant dark reading (about 10% of the reading) in the photodiode array measured, largely due the reverse bias current of the photodiodes and the relatively long exposure times of the camera.

The absorption coefficient is then calculated for a horizontal line of pixels which correspond to the diffracted wavelengths of light from the spectrometer (the pixel with the highest intensity is selected from each column). For each pair of readings we apply the following equation:

$$- \quad —$$

<div align="right">Equation 3.1</div>

where   is the separation distance of the two sections (in this case, one section length) and —— is the ratio of collected signals from S2 and S3 respectively, resolved for each pixel. This provides a measurement of the modal absorption and loss due to the difference in the exponential loss of light which passes through different lengths of unpumped material (specifically the modal absorption and loss of light passing through a unpumped S2 section). Figure 3.8 depicts example measurements of ASE from sections 2 and 3 of a segmented contact devices, where the modal absorption and loss is calculated using Eq. 3.1.
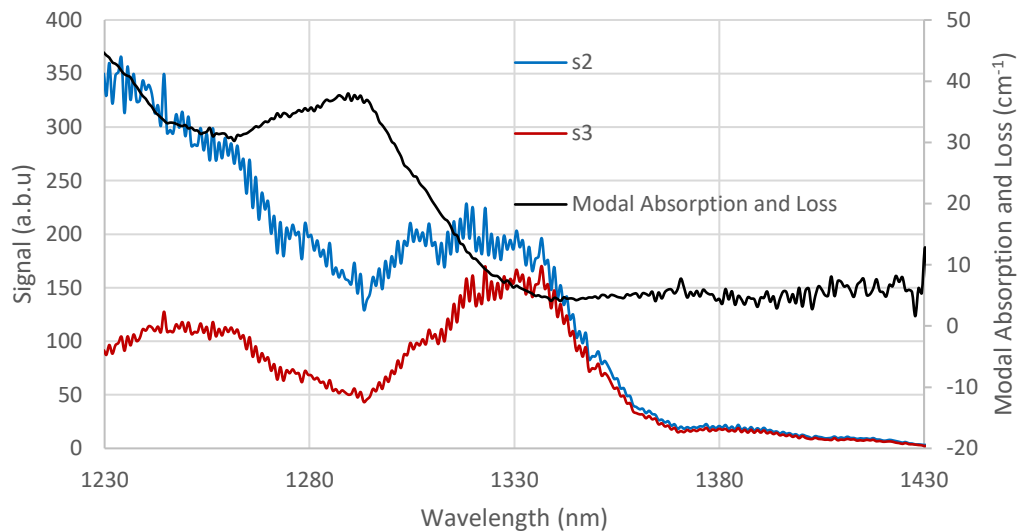
Figure 3.8 Example ASE and resulting modal absorption and loss spectrum for InAs QD sample obtained through Eq 3.1.

The net modal gain may also be found by comparing emission from   (where S2 and S3 are both operated simultaneously) and   with equal current densities with the following expression:

$$\qquad - \quad \overline{\qquad}$$

Equation 3.2

An example of the application of Eq. 3.2 is given in Fig. 3.9. Here the modal gain and loss are found by determining the net optical amplification of ASE passing through the active S2 section. This is usually obtained across a range of current densities. The net modal gain at the lasing wavelength at threshold current density may be compared with the threshold gain condition (i.e. the expected mirror loss) to confirm the experiment's validity. The agreement of the optical mode loss obtained from each of the
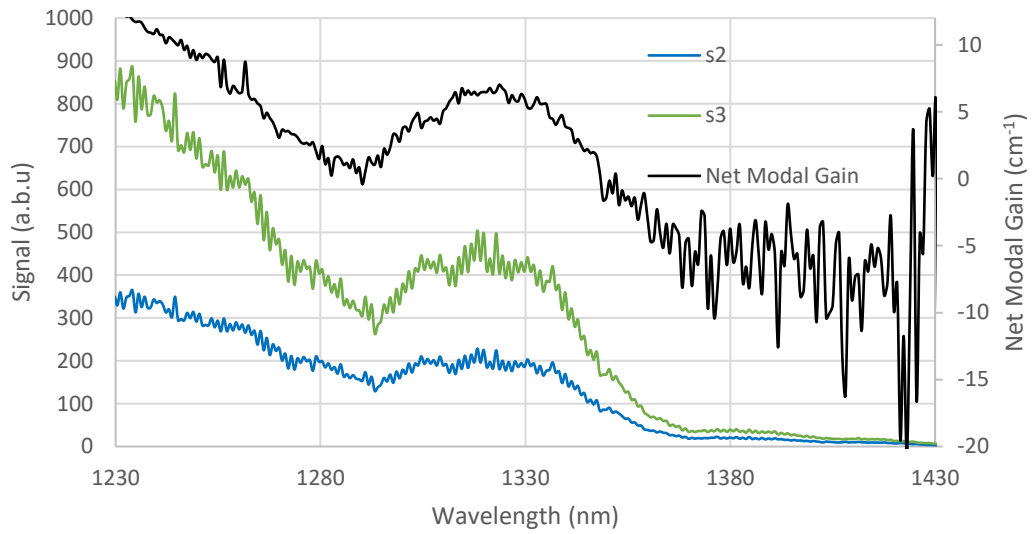
Figure 3.9 Example ASE and resulting net modal gain spectrum for InAs QD sample obtained through Eq 3.2.
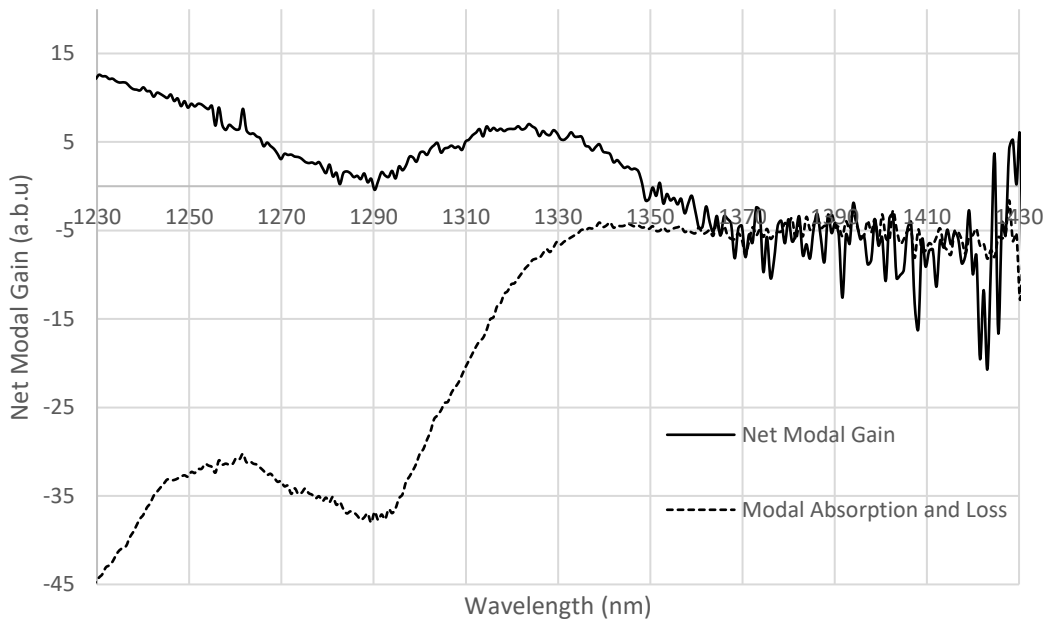
Figure 3.10 Agreement between spectra obtained in Fig 3.8 and 3.9 apparent at long emission wavelengths.

3.4.6 Comments

As is the case in Hakki-Paoli's method for measuring modal gain and loss, the SCM may be used to obtain a range of modal loss values below the band edge, limited only by the decreasing SNR with increasing wavelength. However we note the following disadvantages; unlike Hakki and Paoli's

method or the DQE method, the SCM requires a specially fabricated test structure. While there is significant overlap with the fabrication of cleaved BA laser devices (which are already used in our other laser characterisation methods) the additional fabrication step of introducing electrical breaks in the top contact can be non-trivial. Inconsistencies in the measured ICR between sections and over-etching of the breaks have been observed, and while such defective samples can be eliminated before testing, this process of elimination significantly increases the time between device fabrication and measurement.

I also observed that the measurement of modal gain and loss is less well-suited to determining   . Here the band edge of the S2 section is, similarly to S3, shifted to lower photon energies by Coulomb interactions, which limits the range of measured modal loss values to longer wavelengths where the SNR is reduced. Additionally, where only a single current source is used, it is necessary to change the applied current between a measurement of   and   . Experimentally this can introduce a small difference in current density applied to the sections. This is due to uncertainty in the measurement of current and also, where current spreading in the device is significant, we would expect the relative amount of current spreading to be reduced when two adjacent sections are measured. This introduces further uncertainty in the correct applied current to use between measurements.

These problems are not encountered in the SCM for modal absorption and loss, therefore in our pursuit of achieving the best precision in measuring   we will apply this method. However, while the ASE emission used to interrogate the modal loss is higher here than in the case of modal gain and loss measurements, the SNR can remain challengingly low. This is due to a combination of factors, including the reduced optical power from operation of sections under lower duty cycles (necessary for reducing heat generation in the device); the narrow collection angles of ASE from the facet; and in the case of measurements from sections S2 and S3 the additional absorption of the unpumped material in S1. The impact of low SNR can be overcome through longer measurement durations and optimisation of the measurement system, however limits to this are encountered due to drift in the experimental conditions with time (Section 3.5.1).

3.5.0 Improving Precision in the SCM

In our discussion of modal gain and absorption characterisation techniques we identified the SCM as a good candidate for achieving precise measurement of   (Section 3.4). Precise characterisation of   is of significant commercial value (Section 2.3.1) as it informs manufacturers of the role different design decisions contribute to the value of optical loss, and those decisions

subsequent impact on lasing threshold current and above-threshold slope efficiency (Section 2.3.3). I hope to show in Chapter 4 that the SCM for the measurement of modal absorption and loss can be used to precisely determine   to within a 0.1cm^{-1} margin of error for samples with low modal loss (of the order of 1cm^{-1}).

In order to do this however we must overcome the primary weakness of measuring modal loss by the SCM; low SNR of ASE within the region of interest (below the band-edge of the unpumped material). The low SNR is a result of the inherently low optical power of ASE (note the device is not lasing in this experiment). This is reduced further due to decreasing emission at photon energies below the gain medium's band edge; the use of low duty cycle pumping to reduce the self-heating of devices; and the narrow collection angle of ASE from the segmented contact device (Section 3.4.5).

Imprecise values of ASE and therefore modal loss due to low SNR may, time constraints permitting, be overcome by increasing the integration time of the signal, as the uncertainty of individual signals should be reduced with a square root proportionality with time. For the purpose of defining acceptable experiment durations, we define a long measurement duration as being in excess of 5 minutes, and prohibitively long measurement durations as in excess of an hour. Within a SCM measurement of modal absorption and loss, this measurement duration is made up of the sum of the integration times of signals from two sections and a background reading.

3.5.1 Systematic Drift

Increasing precision in the mean modal absorption and loss (abbreviated as   ) values with increasing integration time assumes a measurement system where random error is the only factor. However, this will not remove *systematic* errors from the measurement. Systematic errors to be already addressed in the SCM for   include a non-linearity response function of the detector, experiment-to-experiment variations in the background noise level; departures from the ideal collection of ASE from devices (such as from poor alignment or optical layout); and non-identical behaviour of pumped sections. Each of these are addressed within the conventional experiment (Section 3.4.5) and the calibration method presented in Chapter 4.

We must also consider the time varying conditions within the experiment, the impact of which on the measured ASE of sections is observable in Fig. 3.11. These can arise from a number of sources, including changes in the alignment of the segmented contact device with respect to the lens (due to relaxation of translation micrometres controlling the translation stage and spectrometer aperture), instability in the current source, instability in the detector sensitivity, or a change in the

background noise level across the experiment duration (see also Section 3.6.2). Each of these will introduce a change in the measured ASE between the two sections, resulting in an apparently different value for   . This problem is exacerbated with longer measurement durations, as the net change introduced by time varying systematic errors, or *systematic drifts*, have been observed to increase with experiment duration, within the time periods under investigation.
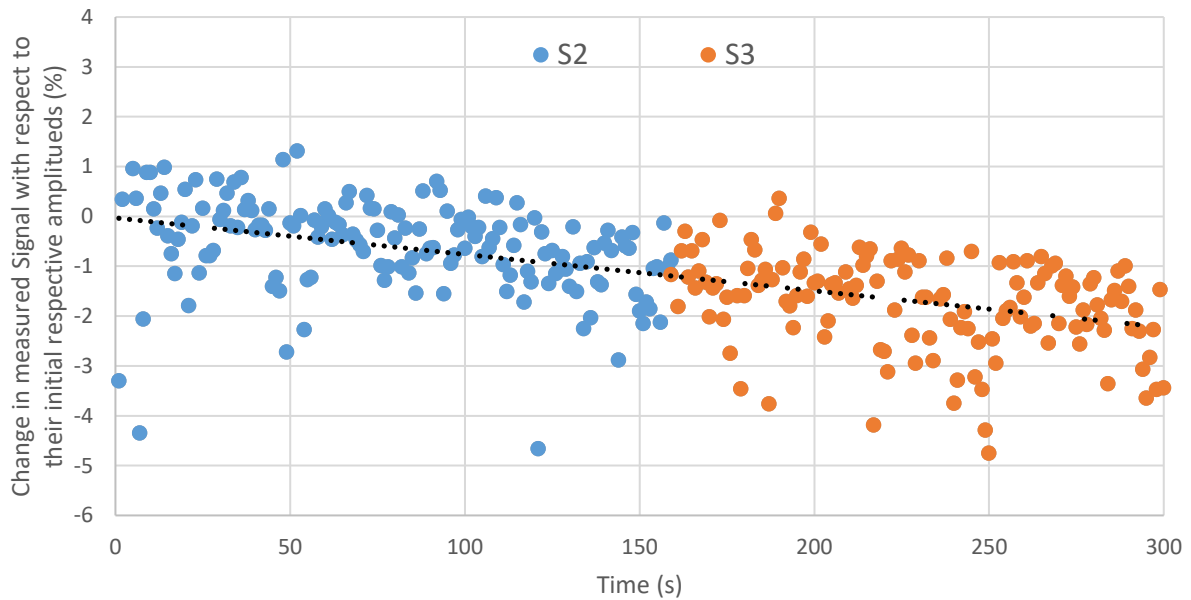
Figure 3.11 Percentage change in background corrected signals (measured across 5 pixels at 1340nm (below the material band gap) for an InAs QD segmented contact device. Note initial measurement of S2 taken at t=0s while initial measurement of S3 is taken at t =150s. Data in S3 is then shifted by -1.23% to demonstrate the continued drift throughout the experiment.

If we assume the systematic drift acts purely multiplicatively upon the true signal, and is linear with respect to time (we propose a time varying sensitivity of the detector could account for this); then we may plot the drift in the signal as a function of a percentage change from its initial value (found by 1st order linear regression). Given this, the data shown in Fig 3.11 demonstrates a multiplicative drift of -2% across the 300s experiment duration. From the mean of the distributions from S2 and S3 we may calculate a value for the modal absorption using Eq. 3.1. The resulting modal absorption and loss value obtained from data presented in Fig 3.11 is 4.23cm^{-1}.
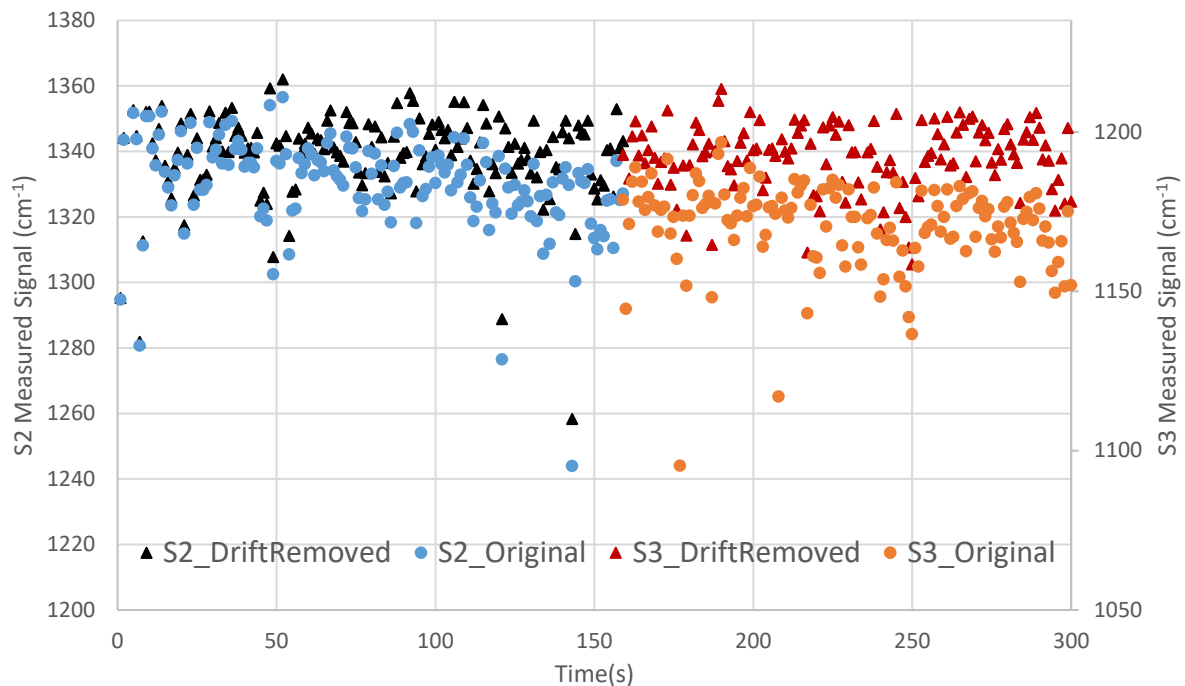
Figure 3.12. Original signals as used in Fig. 3.11, with the adjusted signals calculated by correcting for the difference in signal given the proposed linearly varying multiplicative drift observed with respect to time = 0s

If the systematic drift in Fig. 3.11 is purely multiplicative, then the trend line fitted through this data may be used to correct for the time dependent shift (Fig. 3.7). The value for the modal absorption and loss derived for this adjusted distribution is 3.86cm^{-1}.

However, it is equally valid to assume the variation is due to a linear *additive* drift. A similar correction to that observed in Fig. 3.12 can be made under this assumption, perhaps by surmising the background reading has drifted since it's measurement at the start of the experiment. The modal absorption derived from this correction would instead give 3.63cm^{-1}. We believe a combination of both such drifts are possible in our apparatus.

Distribution	Modal Absorption and Loss (cm^{-1})	Standard deviation (cm^{-1})
Original	4.23	0.35
Corrected for Linear Multiplicative Drift	3.86	0.26
Corrected for Linear Additive Drift	3.63	0.25

Table 3.1 Summary of modal absorption values obtained from data presented in Fig 4.1, and the corrected values of (A+α_i) values given corrections to the observed linear drift.

Both of our assumptions suggest that the systematic drift observed in Fig. 5.1 leads to an overestimation of the modal absorption by at least 0.3cm^{-1}. Furthermore, we show that correcting for this drift by analysis of the time series data does not improve our precision below 0.1cm^{-1}. Rather

than rely upon assumptions in the correction of the data, we will instead consider how drift in the measurement may be minimised.

3.5.2 Overcoming Systematic Drift

Here we consider how those systematic drifts mentioned in Section 3.5.1 may be addressed.

Changes in the device alignment are easily observed by imaging the ASE using the image reflected onto the photodiode array when using the spectrometer's "zeroth order" of diffraction. After making significant changes to the position of the device using the translation stage at the beginning of a measurement, the position tends to slowly drift across many minutes to a "relaxed position". This is especially noticeable where the translation components (e.g. micrometres) used have included elements that provide a constant restoring force, usually created by a spring, for the purpose of facilitating movement in the reverse direction. This constant restoring force is capable of causing a change in the position of the device, what we call the "relaxation" of the translation element, with respect to the lens. This has the impact of altering the position of the peak of the device nearfield with respect to the spectrometer slits, resulting in a change in signal intensity. This would typically be observed as a reduction in signal strength. If the relaxation is sufficient, the optical collection geometry may vary enough such that light which has not travelled directly through the centre of the device (i.e. scattered light) is collected, resulting in an incorrect value of $(A+\alpha_i)$. (Lutti, 2005)

This is minimised by allowing the translation stage to reach its relaxed position before measurement. Small adjustments made to the micrometres after the stage has reached a relaxed position are not observed to incur further relaxation of the translation stage (confirmed by checking the device nearfield before and after a long rest period of ~10 minutes). These measures are expected to minimise, if not completely remove the effect of drift due to alignment changes.

Variations in the detector sensitivity and background noise level are less easily controlled. Both are expected to have some temperature dependence; and background noise in particular is expected to increase rapidly with detector temperature. In our detection system, the temperature of the photodiode array is kept low (200K) and constant by a thermoelectric cooling, the operating power of which is handled in one of two modes: constant temperature or constant power.

Under constant temperature, the detector's temperature is continuously measured and the cooling power adjusted accordingly to maintain it at a user defined level. This has the advantage of

allowing the detector to adapt to changes in environment (i.e. environmental temperature). In practice, however we found the software monitoring of temperature and adjustment for cooling power leads to unnecessary variation of the detector temperature, likely due to imprecision in the measurement of the detector temperature.

Constant cooling power is observed to achieve a more constant temperature, however it does leave the system sensitive to variations in the environmental temperature. Like the thermoelectric cooling of the device, the environment temperature may also be actively controlled, however this must be done precisely to obtain the desired effect. We also observe that the cooling power delivered to the camera is unstable when operated close to its maximum capacity (observed from the software's measurement of the detector temperature). While the cooling is subsequently limited to well within its limits (75%), it remains a possibility that instability in the applied cooling power is not completely removed. Operating without the thermoelectric cooler leads to prohibitively large background noise.

For these reasons, we opt to use a constant cooling power of 75% of its maximum capacity, and minimise temperature changes by not actively heating or cooling the environment of the experiment during measurements.

Lastly, we consider the background light level in the environment. This is minimised by operating the experiment in a blacked out environment. We also take the precaution of minimising stray light from experiment equipment within the environment (e.g. monitors, light emitting diodes of equipment).

We may conclude that while the above measures will help to minimise systematic drift, its complete removal may not be practical nor possible. Indeed, all the data taken throughout this work was undertaken using the above described steps. This includes the example of systematic drift shown in Fig. 3.11.

Given this, we will instead aim to minimise the *impact* of systematic drift. As the impact of systematic drift in this system has become more evident with the introduction of longer measurement durations, we address it by effectively minimising the time difference in the measurement of compared sections.

To do this, we may consider the limiting condition, where there is no time difference between measurements of both signals; and also the background reading. Under such conditions, a multiplicative change would be equally applied to both signals, and in taking their ratio will disappear. An additive change meanwhile will be equally applied to both signals and background measurements, and will be removed when adjusting for background readings in the measurement.

This limiting condition can be approached by rapidly switching between measurements of these three signals with a period which is short with respect to the drift observed. To achieve this between the ASE signals of S2 and S3, we must switch which of these sections is receiving pulsed current. We automate this process by introducing a computer controlled switching relay between the pulse generator and segmented contact device, and switch between either grounding or providing pulsed current to each of the sections we want to measure. To frequently sample the background reading, we use a computer controlled shutter mechanism which interrupts the optical path between the segmented contact device and the spectrometer.

Switching between which section receives pulsed current is effectively a *modulation* of the length of unpumped section through which the ASE is measured. Increasing the switching rate between sections, and increasing the sampling rate of the background reading, causes the experiment to approach the limiting condition of simultaneously measuring all three signals. We will explore the full application of this modulated approach further in Section 4.

BLOOD, P. 2015. *Quantum confined laser devices : optical gain and recombination in semiconductors*, Oxford : Oxford University Press.

BLOOD, P., LEWIS, G. M., SMOWTON, P. M., SUMMERS, H., THOMSON, J. & LUTTI, J. 2003. Characterization of semiconductor laser gain media by the segmented contact method. *IEEE Journal of Selected Topics in Quantum Electronics,* 9**,** 1275-1282.

CASSIDY, D. 1984. Technique for measurement of the gain spectra of semiconductor diode lasers. *Journal of Applied Physics,* 56**,** 3096-3099.

COLDREN, L. A. & CORZINE, S. W. 1995. *Diode Lasers and Photonic Integrated Circuits,* New York, Wiley.

CRUMP, P., ERBERT, G., WENZEL, H., FREVERT, C., SCHULTZ, C. M., HASLER, K. H., STASKE, R., SUMPF, B., MAAßDORF, A., BUGGE, F., KNIGGE, S. & TRÄNKLE, G. 2013. Efficient High-Power Laser Diodes. *IEEE Journal of Selected Topics in Quantum Electronics,* 19**,** 1501211-1501211.

HAKKI, B. & PAOLI, T. 1975. Gain spectra in GaAs double–heterostructure injection lasers. *Journal of Applied Physics,* 46**,** 1299-1306.

HOFSTETTER, D. & THORNTON, R. L. 1998. Measurement of optical cavity properties in semiconductor lasers by Fourier analysis of the emission spectrum. *IEEE Journal of Quantum Electronics,* 34**,** 1914-1923.

LUTTI, J. 2005. *Optical properties of InP/AlGaInP quantum dot laser heterostructures.* PhD Thesis, Cardiff University.

SMOWTON, P. M. & BLOOD, P. 1997. On the determination of internal optical mode loss of semiconductor lasers. *Applied Physics Letters,* 70**,** 2365-2367.

VOLET, N., STANTON, E. J., DAVENPORT, M. L., SPOTT, A., CHANG, L. & BOWERS, J. E. Refined procedure for gain measurement in Fabry-Perot semiconductor lasers. 2016 IEEE Photonics Conference (IPC), 2-6 Oct. 2016 2016. 534-535.

Chapter 4   Modulated Segmented Contact Method for Precise Measurement of Optical Mode Loss

4.1   Introduction

In this chapter, we introduce the modulated approach to the segmented contact method (SCM) for the measurement of modal absorption. We begin with the motivation for this work (Section 5.2), namely reducing the impact of time varying experiment conditions (or systematic drifts, Section 5.2.1) arising from the use of long integration times in the pursuit of precisely measuring small differences in ASE. The method for determining the measurement precision is outlined in Section 5.3. An explanation of the modulated SCM experiment and some of the challenges in its application are addressed in Section 5.4, with a comparison between this and the conventional method provided in Section 5.5. Concluding remarks summarising our findings and how they will be used in later Chapters are given in Section 5.6.

4.2   Measurement of Experiment Precision

Here we will outline how the measurement of the   spectrum through SCM is used to determine   at the *lasing wavelength*, and likewise how the *precision* of the measurement of   relates to the precision in the value determined for   .

Signal due to ASE obtained from a segmented contact device and background readings are collected by each pixel of the photodiode array (which correspond to the different wavelengths in the   spectrum). Each set of signals are integrated across multiple exposures, recorded as a time series, and used to calculate a mean value for the overall integration time. The mean of the set of background readings are then subtracted from the mean ASE signal values to obtain a set of *background subtracted* ASE values. Provided there is a linear response in the detector system, these background corrected ASE signals are used to calculate the   spectrum described by Eq. 3.1. Noise appearing in the measured values for ASE from pixel to pixel will lead to an apparent variance in the values of   .

Conventionally,   is assumed to be equal to the   spectrum when measured below the material band gap. Historically this approach has been reasonable: trends in   below the band edge appear small with respect to those above the band edge. Also, this region is typically poorly resolved, and so within previous experimental limits appears flat. We will later show that for

long integration times a true, observable trend in the modal loss below the band-edge may be observed in below band-edge values of   . Consequently, we must reconsider how we determine   .
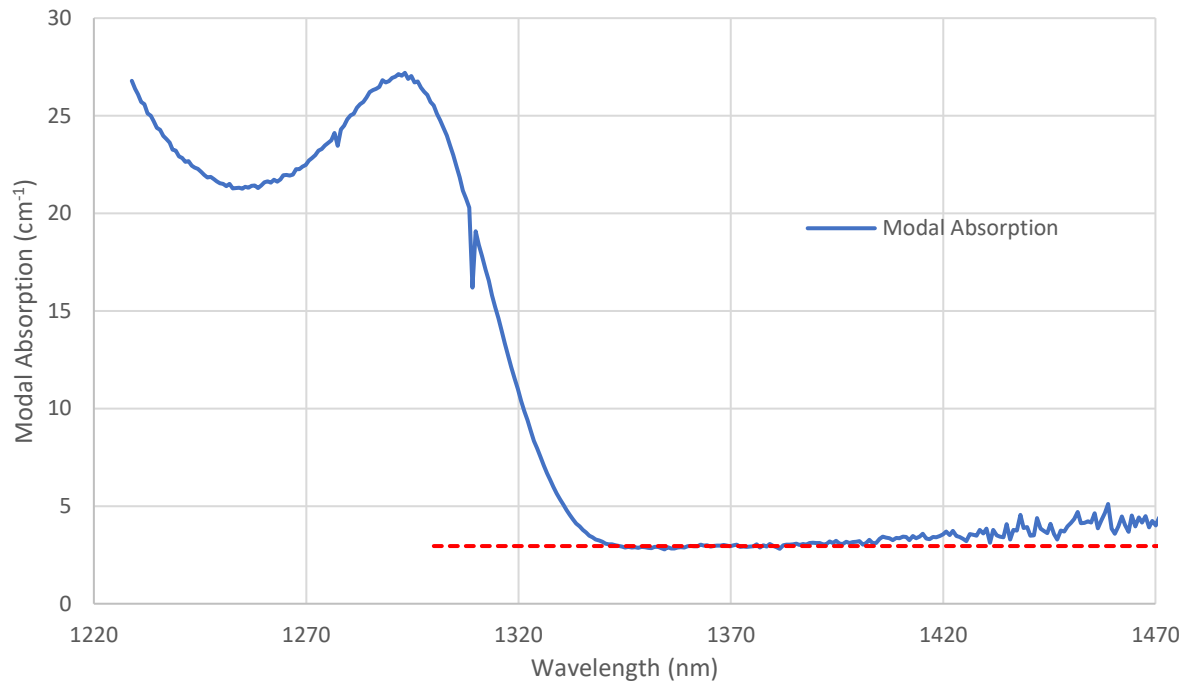
Figure 4.1 Measurement of   from modal absorption and loss data by backward extrapolation of the below band edge behaviour. Convention extrapolation of optical mode loss in red dotted line

In the conventional method, the value of   at the lasing wavelength is determined from an *extrapolation* of what is assumed to be a constant value (i.e. a straight line as demonstrated in Fig 4.1). However, a non-constant value of   requires we determine what form the extrapolating function takes (e.g. linear, polynomial or exponential). We note that the trend in modal loss observed may be due to a combination of factors, including dispersion in the waveguide, wavelength dependence of absorption, each observed in multiple device layers. It is therefore inappropriate to assume the extrapolating function takes the form of any individual contribution (for example, fitting the $\lambda^{1.5-3.0}$ dependence observed in the Drude model), nor is there a requirement that the fit is performed with respect to photon energy or wavelength. It is possible that the appropriate trend with which to extrapolate the value of   would become apparent through modelling of   in these structures. We will investigate this further in Chapter 6.
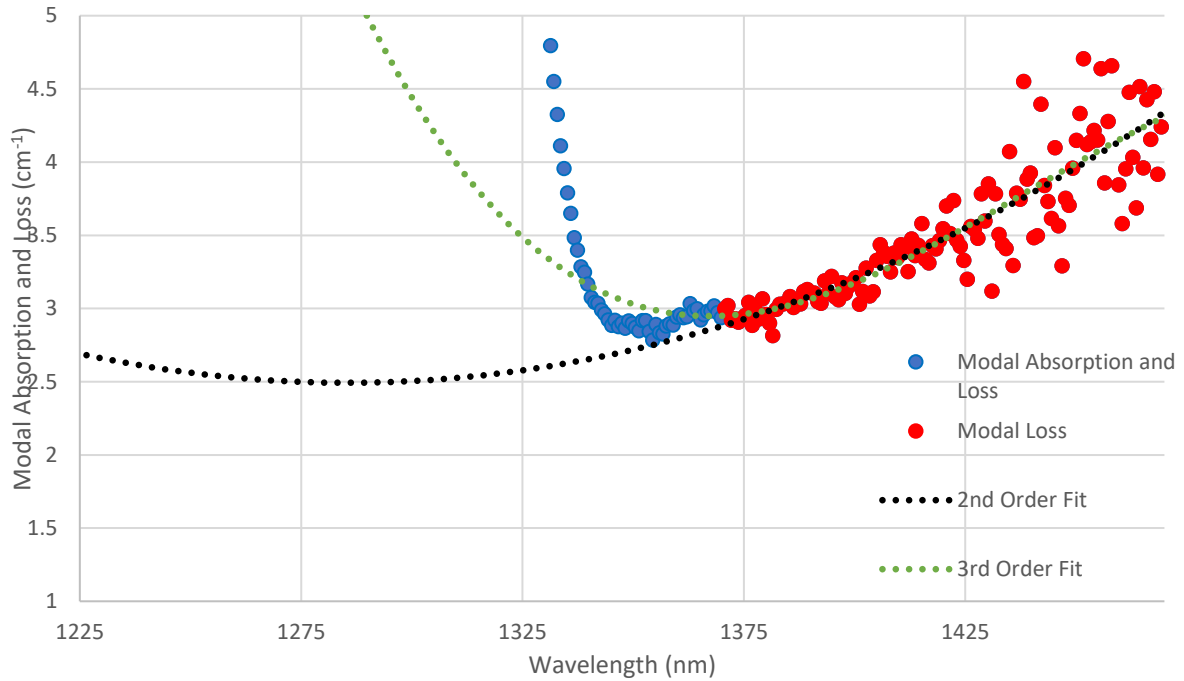
Figure 4.2 Examples of polynomial fits of modal loss data (taken from modal absorption and loss data above 1370nm)

For now, we will consider the choice of fit based upon our qualitative understanding of the modal loss and what we observe in the data. Firstly, the modal loss due to both FCA and IVBA this close to the band-edge should only *decrease* with decreasing wavelength (Section 2.3.3). Similarly, we would expect that dispersion effects will lead to a greater penetration of the optical mode into the cladding layers with increasing wavelength, leading to larger modal loss. This is confirmed in later modelling for the waveguide structure of this device in Chapter 6. We observe that polynomial least square fits of the data in Fig. 4.2 lead to an increase in the modal loss with decreasing wavelength (below 1370nm and 1300nm for 2nd and 3rd order polynomial fits respectively).
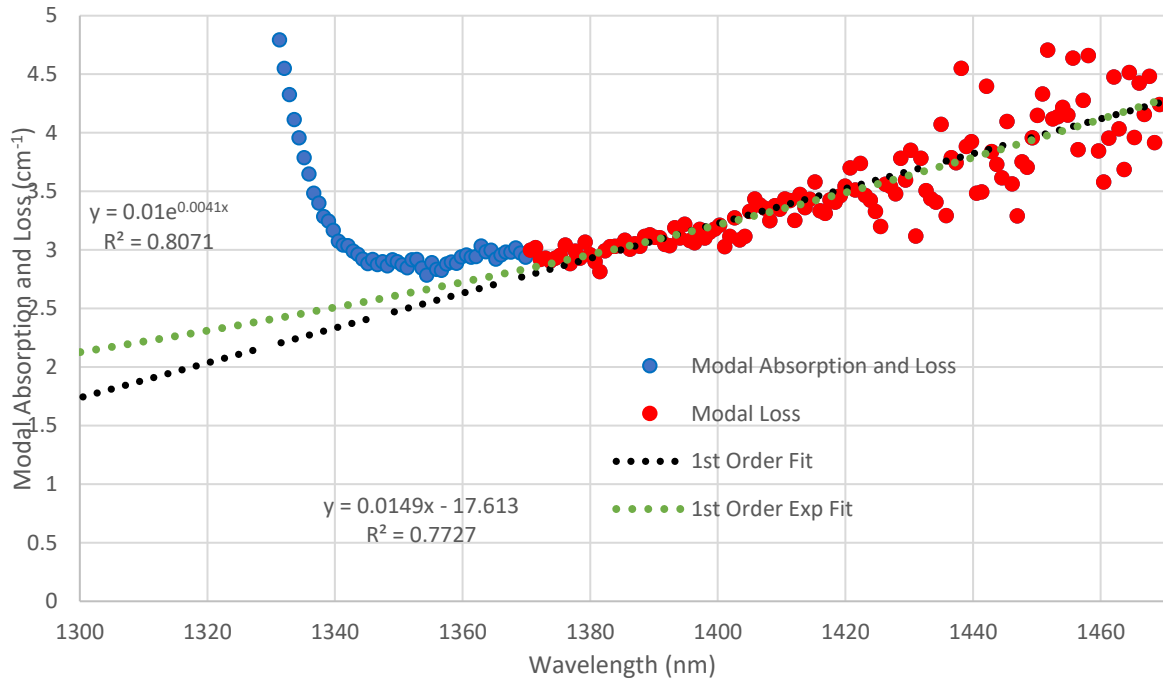
Figure 4.3 Examples of polynomial fits of modal loss data (taken from modal absorption and loss data above 1370nm)

Exponential fits used in Fig. 4.3 implicitly assume that modal loss cannot increase with decreasing wavelength. So too will a linear fit of this data, although it will also eventually lead to unphysical values of negative modal loss. Additionally, analysis of the residuals (shown in Fig 4.3) suggests that the exponential is a better reflection of this data.
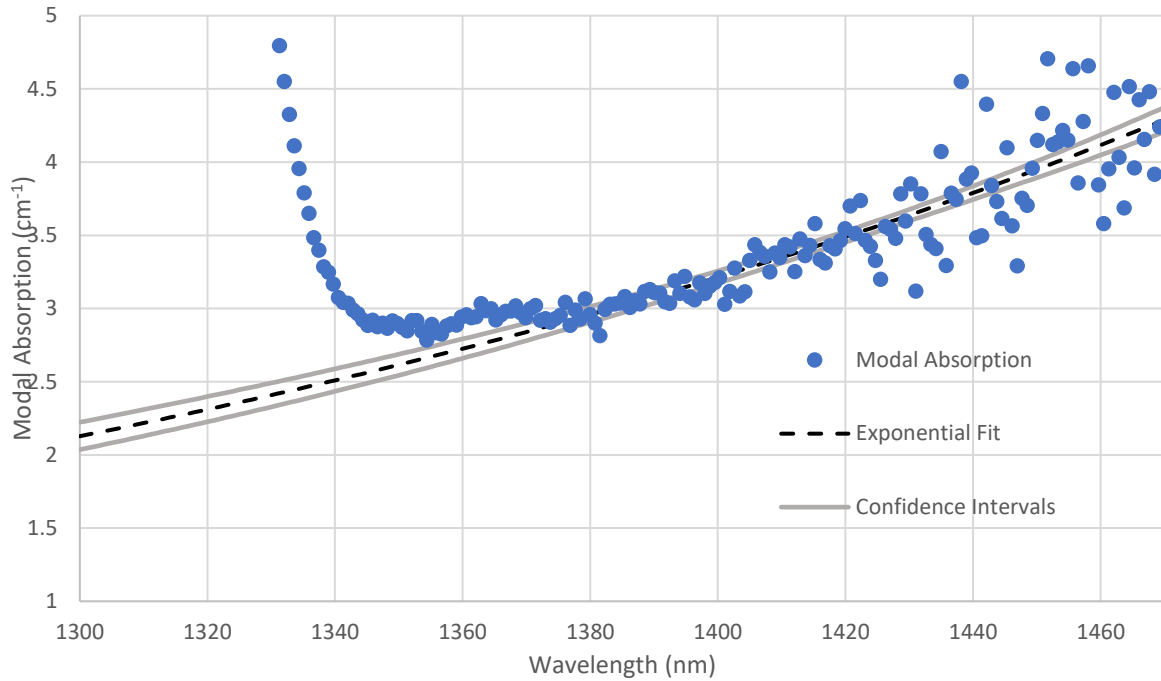
Fig. 4.4 Exponential fit and associated 95% confidence intervals for below band edge behaviour of modal absorption measurement from SCM. Fitted to data between 1370 and 1470nm.

Whichever fit we decide to use in our extrapolation, it is helpful to also determine their *confidence values*. Confidence values for the data are a reflection of the uncertainty in the calculated coefficients of the fit due to the variance and discrepancy with measured modal loss. This is an effective method for determining how the imprecision in the original *measurement* of　　　　goes on to affect the certainty in the extrapolated value for　at the lasing wavelength. This is because this method allows us to see how the uncertainty increases as we extrapolate to wavelengths further away from the measured data. Note that this has serious implications for determining modal loss at wavelengths significantly shorter than the band-edge. For example, short 1mm cavity lasers constructed from material of InAs QD material (segmented contact devices of which are used to generate data in Fig. 4.1-4.4) will have a laser emission which utilises the QDs first excited state (close to ~1200nm). The impact of imprecision in the below band-edge measurement will increase when extrapolating across longer wavelength ranges and so result in much poorer precision.

From the above we have demonstrated how we will obtain the uncertainty in determining from the confidence intervals of the extrapolating function, which we assume to be a first order exponential. Systematic drift in the signal however is expected to be *correlated* between pixels, and is therefore not expected to contribute to the variance in the above calculation. Rather, we may expect an overall increase or decrease in the modal loss; and also a change in the shape of the modal loss

distribution as the relative impact of systematic drift varies with respect to the amplitude of the measured signals.

As this error from systematic drift is not expected to be observed in the pixel-pixel variance of the modal loss, we must measure it through multiple trials of the experiment across an extended time period. The variance in the value of   observed from the exponential fits of multiple trials would then give the *true* experiment precision. We should expect a larger variance in this trial-by-trial value than that due to the above confidence intervals. We will perform this experiment with the SCM measurement for   and determine the discrepancy between experiment precision determined from the measurement and the *true* experiment precision from repeated trials. We will compare this discrepancy in the conventional method with that found from the modulated approach (discussed in Section 3.5.2) to demonstrate the removal of systematic drift.

4.3.0 Experiment Methodology

The modulated SCM adopts the same apparatus as seen in Section 3.4.5. In addition to this however there is a computer automated shutter for obtaining background readings and a switching relay for the rapid switching between measurement of ASE from S2 or S3. Note that the switching relay will connect each section either to the pulsed current source or else ground.
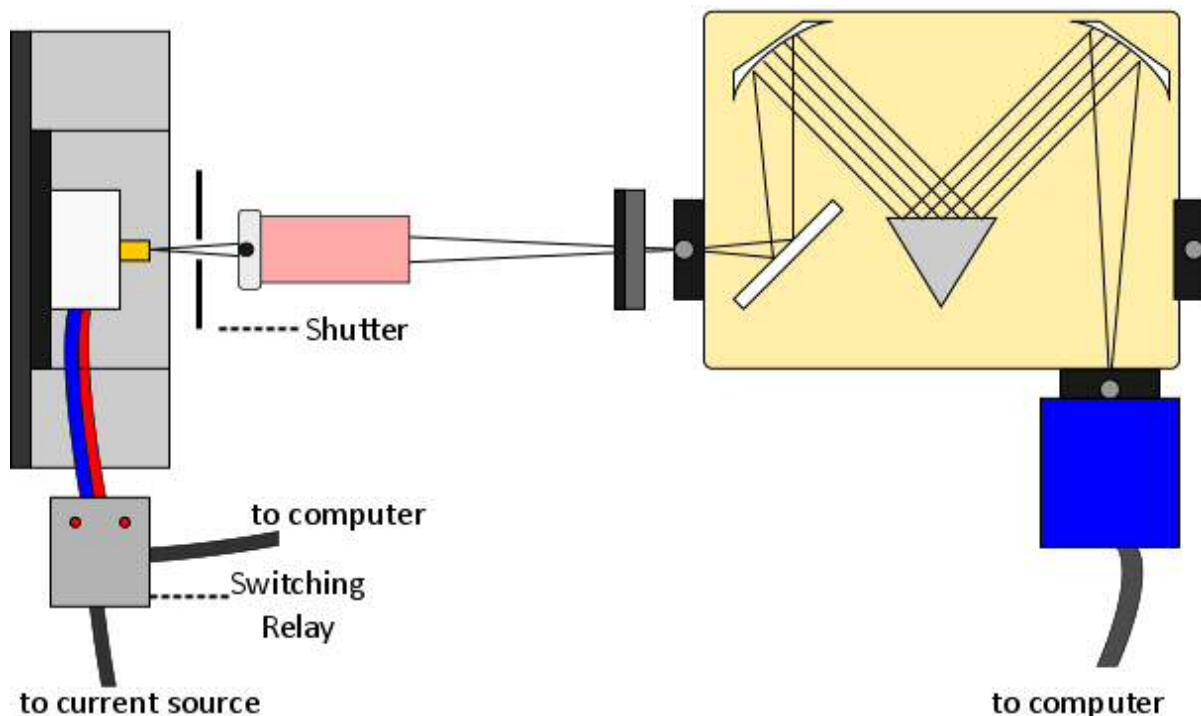
Fig. 4.5 Experiment set-up for modulated segmented contact method. For additional equipment labels see Fig. 3.9.

The switching relay and shutter are controlled by a program (written in Python) which operates while additional software operates the camera system. In this detection system, there is no easy way to implement autonomous communication between the camera operating software and external applications, therefore the switching relay and shutter mechanism are not necessarily operated in phase with the camera's frame rate (see Section 4.3.1).
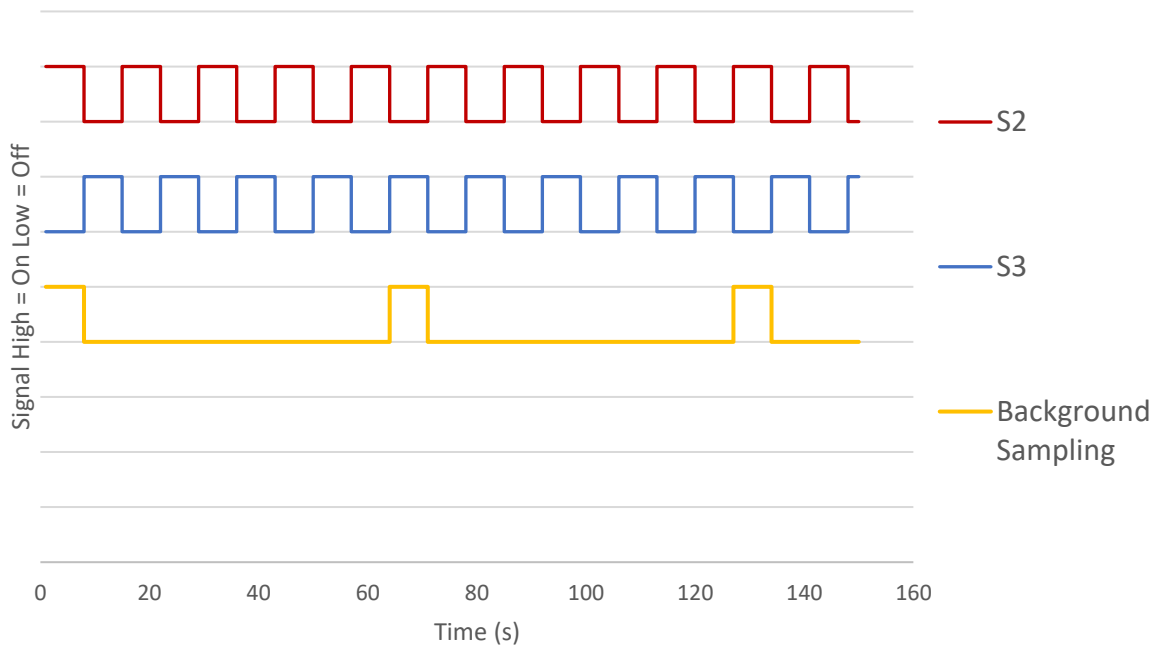
Figure 4.6 Signal sampling for a modulated experiment with a switching time of 7.5s and background sampling after 8 switches

After applying those additional steps towards reducing drift outlined in Section 3.5.2, the camera is set to take multiple exposures of 1s duration each. During this, the switching relay switches current between sections every 7.5s, while the background is sampled less frequently, after 8 cycles of switching (once a minute) (Fig. 4.6). This sampling rate was chosen in order to maximise the integration time which is effectively used to measure the *difference* in ASE between sections S2 and S3. This is important as we are attempting to measure small values of   (~1%) using segmented contact devices with contact lengths of 300μm, which lead to a difference in ASE of as little as 3%. In Fig 3.11, we have observed comparatively large systematic drifts (-1.23%), therefore we have chosen a higher sampling rate of differences between S2 and S3 than between these signals and the background measurement.

Exposures are performed across 200s total integration time. The conventional method we compare against uses the same switching relay and shutter, but instead measures the background across 50s at the beginning of each measurement, followed by 125s each for S2 and S3 signals. This closely matches the integration times dedicated to each signal in the modulated method.

The collected signal is stored using the operating software's video format (Section 5.3), and then interpreted by a second Python program. As the differences in the amplitude of ASE emitted above the band-edge between sections is significant, the program can use these spectra to automatically attribute frames as belonging to ASE emitted by the first or second sections; or to a background reading. It also automatically removes mixed frames (Section 5.4.1). Values for one or more rows of the array are stored as a list of values corresponding to those pixels within the photodiode array's width. This is then output as a time series of values, from which their mean is determined and again analysed using Eq. 4.1.

4.3.1 Signal Sampling

Ideally the camera system should only integrate signals collected *between* the switching and shuttering events, such that we never measure an unknown ratio from two signals. In general, and this includes our own detection system, time series data is collected and readout in a continuous fashion, therefore automated switching will introduce mixed readings where exposures occur during switching events. These mixed frames can be removed provided we know where they occur (i.e. at the observable boundary of switching between signals) such that only pure signals are used during analysis. However, this approach in turn introduces a limit to the useful switching rate. If the switching rate is too quick with respect to the exposure time, then a larger proportion of exposures will be mixed frames. As the exposure time of the camera is effectively set (note the camera system allows time series exposures of no longer than 1s) then we must choose the *switching* rate accordingly.
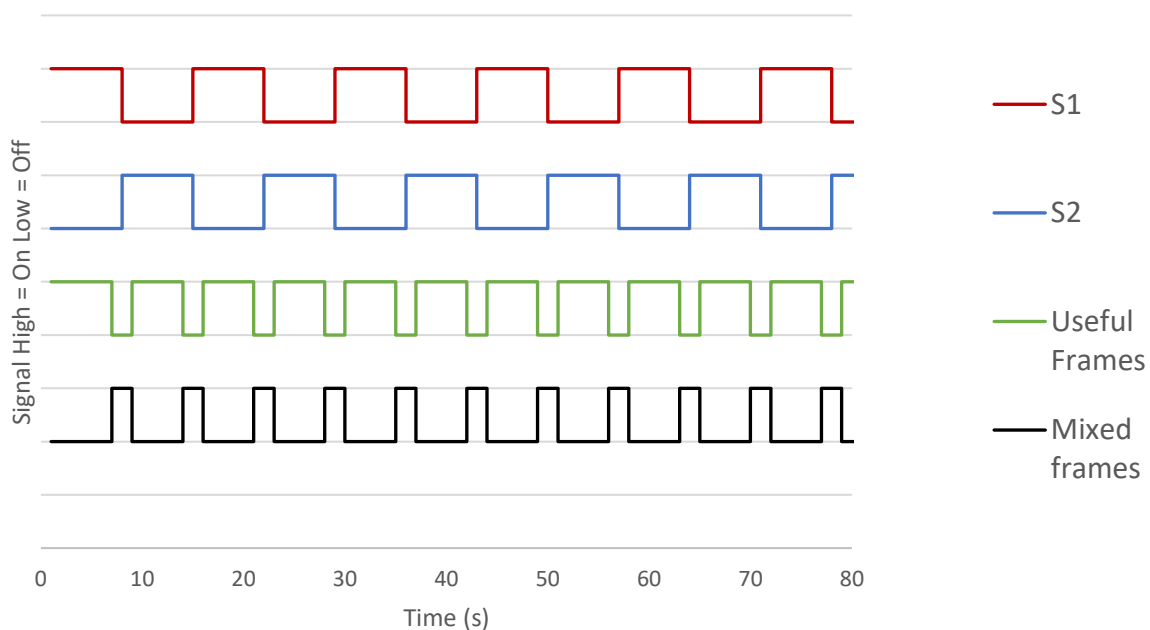
Figure 4.7 Signal sampling for a modulated experiment with a switching time of 7.5s (background sampling not included). Useful frames exist where there is no change in section during its exposure.

69

For each switching event of this detector system, two-three potentially mixed signal frames are generated where the exposure time is 1s (two if the signal switches near to the end/beginning of an exposure, three if this occurs in the middle of an exposure). Thus for the example given in Fig. 5.9, a switching rate of 7.5s switch cycle will result in a loss of roughly 30% of the overall exposures taken.

We believe this decrease in the effective integration time is reasonable for the implementation of the modulated approach and may be optimised in later applications of the method. When comparing the performance of the modulated approach against the conventional method we will retain the same net experiment time.

4.4   Results

For the purposes of assessing the precisions obtainable by the conventional and modulated methods, we will compare the measurement of   by the method of extrapolation from exponential fits described in section 4.2 at 1300nm (the expected lasing wavelength of the devices measured), using data collected below 1370nm (illustrated in Fig. 4.3-4.4). This is repeated for multiple iterations of both experiments in order to determine the true precision of each method. This is expected to be poorer than the precision accounted for by the confidence intervals generated for a single iteration of the experiment.

Both experiments used the same overall integration time (200s) in which to measure both background and section readings. Intermixing of frames in the modulated approach led to an average effective loss of integration time of 31.5%. Data presented in Figures 4.8 and 4.9 were collected by alternating between the conventional and modulated experiment. This ensured that similar experimental conditions were experienced by both methods.

The sample measured was a segmented contact sample fabricated from InAs QD laser heterostructure grown on GaAs, where the stability of the alignment was ensured by those steps described in Section 3.5.2.
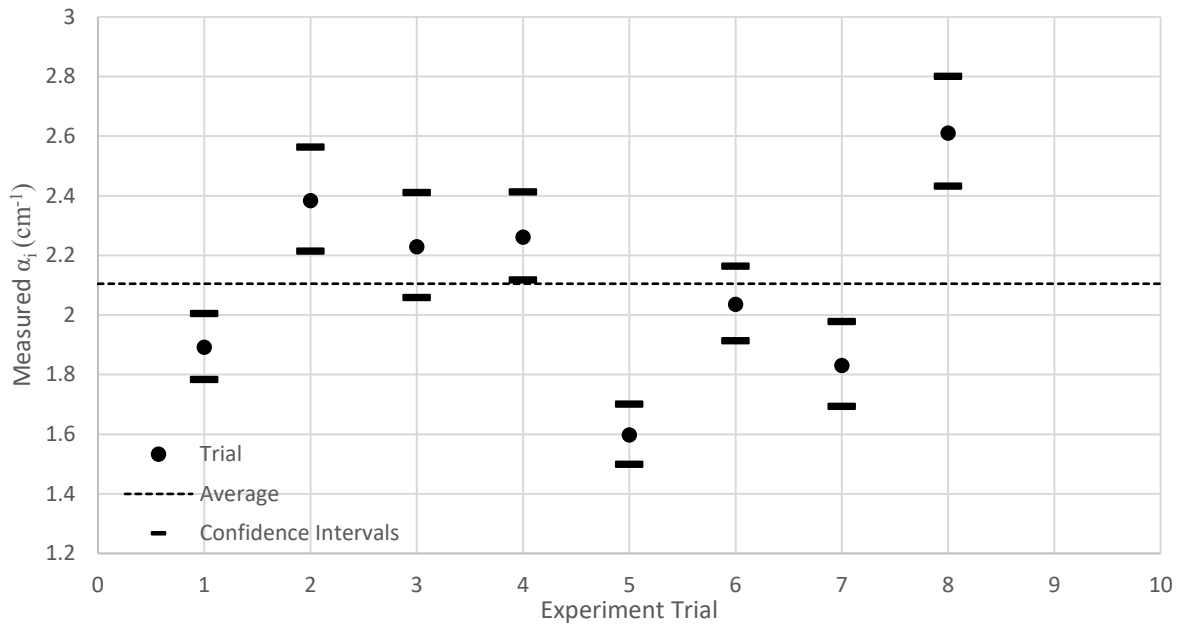
Figure 4.8 Repeated measurements of   across multiple iterations of the conventional SCM method, found by the extrapolation of the below band edge behaviour to 1300nm. Errors given by the 95% confidence intervals of this fit.
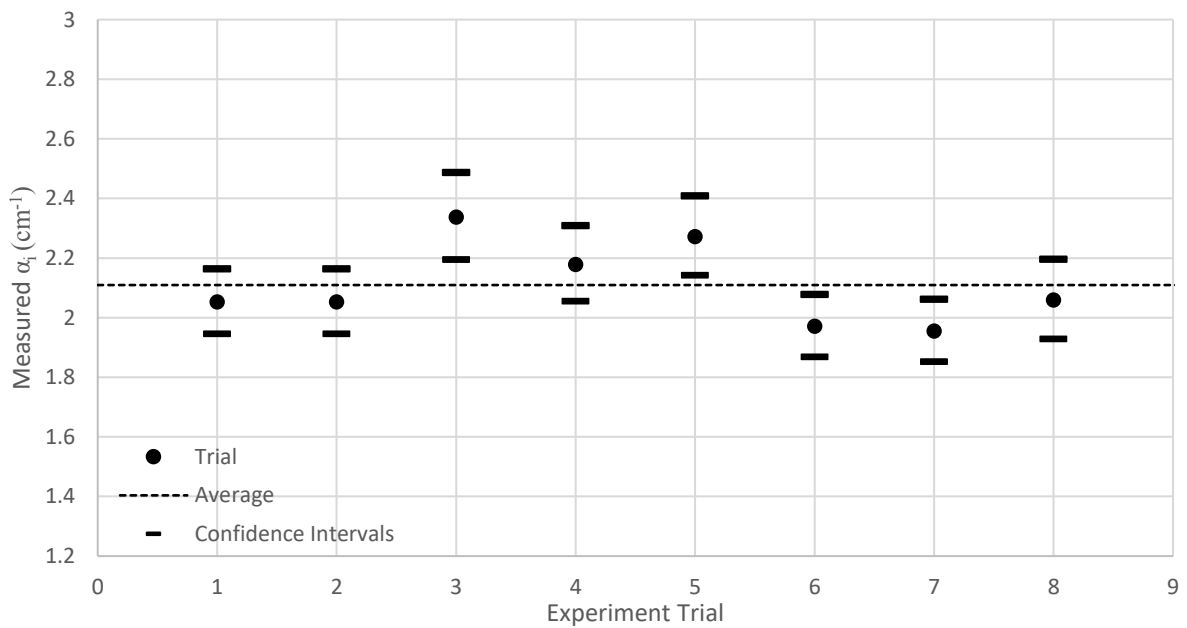
Figure 4.9 Repeated measurements of   across multiple iterations of the modulated SCM method, found by the extrapolation of the below band edge behaviour to 1300nm. Errors given by the 95% confidence intervals of this fit.

From Figures 4.8 and 4.9, we observe the modulated approach reduces both the variance in the fitted   values, and unexpectedly improves the confidence values of the fit.

The first of these effects is understood from our discussion of the systematic drift. The modulated approach, which approaches the limit for simultaneous measurement of the two signals and background values, reduces the impact of systematic drift. Hence the standard deviation in the extrapolated values of   is reduced from 0.33cm^{-1} in the original SCM to 0.14cm^{-1} when modulated. The appearance of this within the measured   spectrum for trial number 5 of Fig. 4.8 and 4.9 is shown in Fig. 4.10. As expected, the apparent noise observed in the data is similar, but the below band-edge trend has been strongly affected by systematic drift.
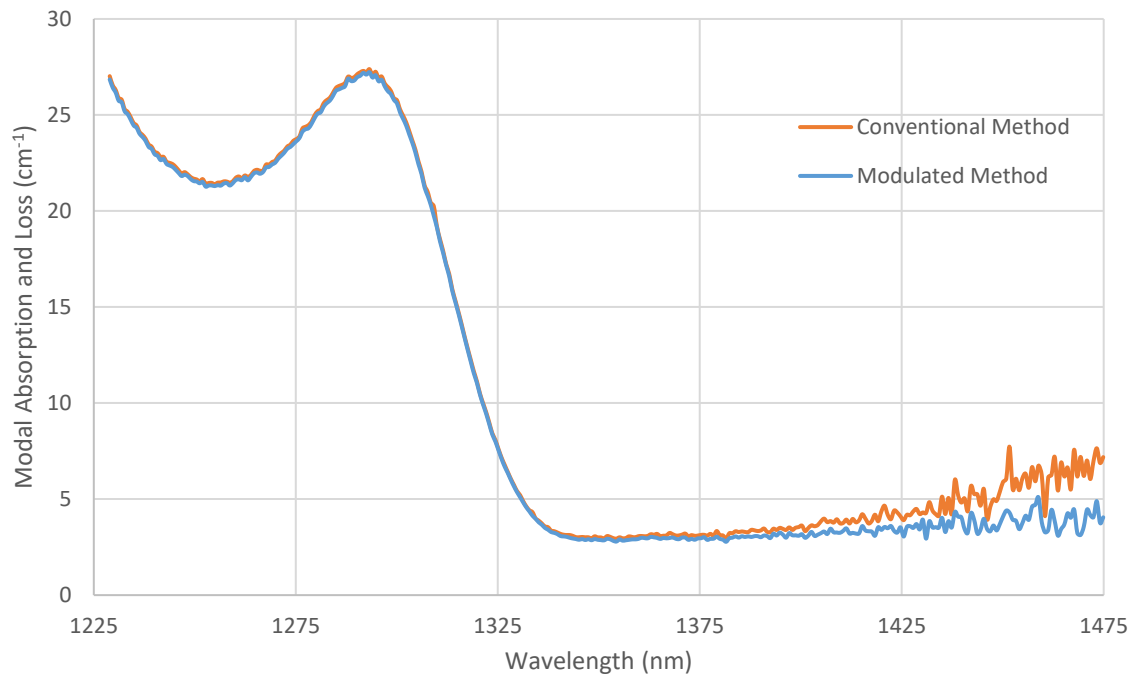
Figure 4.10 Comparison of conventional and modulation modal absorption and loss spectra obtained for trial experiment 5 in Fig. 4.8 and 4.9 respectively

However, the calculated confidence values for each fit were not originally expected to vary. They are observed to decrease from on average 0.15cm^{-1} in the original method to 0.12cm^{-1} when modulated. This suggests our assumption that the systematic drift will not appear in the fitted error is false. An increase in the confidence interval error suggests that the shape of the distribution is less well described by an exponential when systematic drift impacts the result. This is understandable, as the trend in modal loss observed in the measurement changes significantly due to drift (Fig. 4.9), and consequently become less well described by an exponential fit. The change in the modal loss trend observed in Fig. 4.10 is consistent with *additive* systematic drift, as the deviation from the assumed to be reliable modulated modal loss measurement increases with longer wavelengths, just as the ASE of the measurement decreases with longer wavelengths.

We anticipated the confidence intervals of the original method would fall short of the true experiment scatter, while the modulated approach would improve upon this. In the original method, the confidence intervals underestimate the true scatter by 0.18cm^{-1}, while in the modulated method there was an underestimate of just 0.02cm^{-1}. This difference is shown by the improved agreement between the average of the distribution and the margin of error due to confidence intervals between Fig. 4.8 and 4.9.

The remaining discrepancy between the confidence values and scatter found for the modulated method is small with respect to the 0.1cm^{-1} precision we wish to achieve. We believe this remaining difference is due to the remaining influence of systematic drift in the measurement. It may be possible to reduce the impact of systematic drift further by increasing the rate of switching during the modulation method, even at the expense of losing additional frames due to mixed exposures. However, a more reasonable approach (which we will adopt in later measurements) is to introduce an additional 0.02cm^{-1} error due to systematic drift when calculating errors in the measurement from confidence values.

4.5   Concluding Remarks

We have shown how a modulated approach to the SCM for   measurements may be used to reduce the uncertainty in measurements of   . This uncertainty, arising from time varying conditions in the experiment (or *systematic drifts*), has been shown to be largely absent from the uncertainty calculated from the 95% confidence intervals calculated from extrapolating exponential functions fitted to the below band-edge modal loss.

By applying a modulated approach to SCM, we substantially reduce the *true* error of the experiment (obtainable only from multiple iterations of the experiment), demonstrating improved experimental precision from 0.33cm^{-1} to 0.14cm^{-1}. This is despite an effective loss of 31.5% of the integration time encountered in the modulated approach. Crucially the *true error* obtained by the modulated approach is shown to be in excellent agreement with the error obtained from the 95% confidence intervals.

Given this, future measurements of   will be made using a modulated approach to SCM using those switching times used within this chapter. The uncertainty in the measurement of will be found by adding a small correction (0.02cm^{-1}) to the uncertainty derived from the confidence intervals to account for the remaining influence of systematic drift. Measurement of   to precisions

as low as 0.1cm^{-1} will require the combined uncertainty of the exponential fit and this 0.02cm^{-1} correction to be within this limit.

I have found that even with the relatively short integration times (200s) used in the experiments of this chapter, we have demonstrated the measurement of low values of   (~2cm^{-1}) with precisions approaching 0.1cm^{-1}. I will increase the integration times further in later work to approach precisions of less than 0.1cm^{-1}. This compares favourably with precisions observed for the differential quantum efficiency method, of the order or 0.5cm^{-1} in (Slipchenko et al, 2004), and the Hakki-Paoli method, 3cm^{-1} in (Shtenge and Ackerman, 1995).

LUTTI, J. 2005. *Optical properties of InP/AlGaInP quantum dot laser heterostructures.* PhD Thesis, Cardiff University.

S. O. SLIPCHENKO, D. A. VINOKUROV, N.A. PIKHTIN, Z. N. SOKOLOVA, A. L. STANKEVICH, I.S. TARASOV, ZH. I. ALFEROV. Ultralow Internal Optical Loss in Separate-Confinement Quantum-Well Laser Heterostructures. *Physics of Semiconductor Devices,* Vol 38, Issue 12, pp1430-1439.

G. E. SHTENGE, D. A. ACKERMAN, "Internal optical loss measurements in 1.3µm InGaAsP lasers," in Electronics Letters, vol. 31, no. 14, pp. 1157-1159, 6 Jul 1995.

Chapter 5 Amplitude calibration of photodiode array by flux superposition

5.1 Introduction

In this chapter we introduce a necessary step in the precise measurement of modal absorption and loss by the SCM. We begin by expanding upon our motivation for this work (Section 5.1). This is followed by a complete description of the detection system used in this work (Section 5.2). We show a clear non-linear response in the detector system both by increasing background light levels and by increasing the signal strength of ASE of segmented contact devices (Section 5.3). We explore the cause of this non-linear response by considering the components of the photodiode detector (Section 5.4). An experiment for the amplitude calibration of the detector by a method of flux superposition is then described (Section 5.5). The removal of non-linearity by this method is demonstrated and its impact upon the measurement of modal absorption and loss is shown in Section 5.5.4. It's use as a tool for comparing the non-linearity of the detection system under different experiment conditions is also demonstrated. Concluding remarks are given in Section 5.6.

5.2 Motivations

As discussed in Section 4.2,   is typically determined by the SCM for the measurement of modal absorption and loss from the modal loss observed below the material band. Within the usual measurement uncertainties, the below band-edge values for   was assumed to be equal to the value within the band-edge, i.e. at the lasing wavelength of the device.
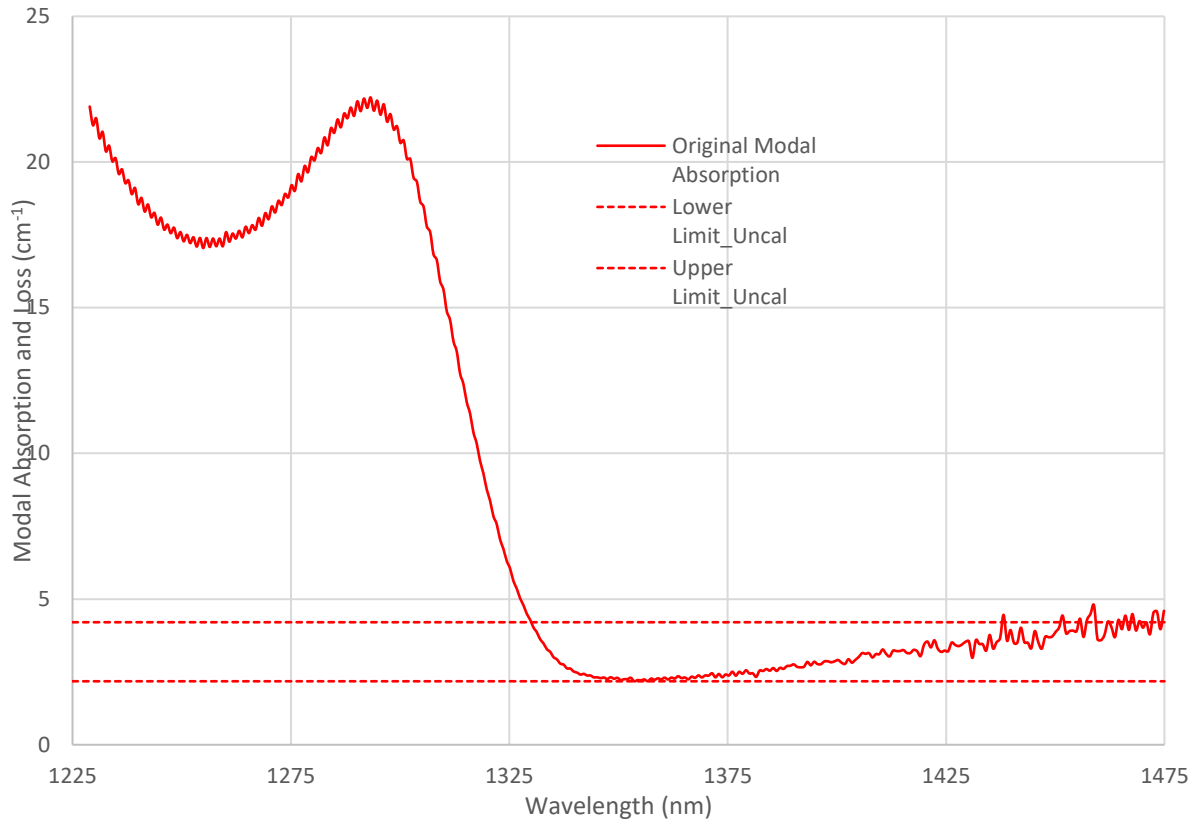
Figure 5.1 Modal absorption and loss obtained by SCM across long integration times for an InAs QD on GaAs substrate segmented contact device. Dotted lines added indicate approximate upper and lower limits of measured modal loss (2.2-4.2cm⁻¹). "Ripple" in data will be discussed in Section 5.6.

In the pursuit of measuring   to precisions with 0.1cm^{-1} we applied longer integration times (5 minutes per section with a 1s exposure time) to this measurement, and also introduced a modulated method for improving the precision further (Chapter 4). This revealed a non-constant value of optical mode loss below the material band edge which increased with longer wavelengths (Fig. 5.1).

Possible physical reasons for this increase include the wavelength dependence of free carrier absorption and IVBA; or wavelength dispersion of the waveguide (these effects are explored fully in Chapter 6); however as changing modal loss of laser waveguides below their band-edge have not been widely reported for these emission wavelengths, possible experimental causes for this trend were investigated. These investigations led to the observation of the non-linear amplitude response discussed further in Section 5.4.

5.3   SCM Detector Setup

ASE from segmented contact devices, diffracted using an Oriel Spectrometer, is collected by a Xenics Xeva 1.7-320 Infrared InGaAs photodiode array (320x256 pixels) camera, with a nominal range of 850nm to 1700nm. Light diffracted from the diffraction grating (600 lines grating with a blaze

wavelength of 1200nm) is imaged along the array x-axis, giving an effective range of about 246nm and maximum resolution of 0.77nm (varying with the dispersion of the spectrometer).

Light incident on each pixel is measured with an InGaAs photodiode whose reverse bias photocurrent is measured by a Capacitance Transimpedance Amplifier (CTIA). A true circuit diagram of this element in unavailable (manufacturer support for the camera system is unavailable), however given information within the manual and software settings we infer that this circuit behaves in a similar manner to that described in (Burr-Brown, 1996), an integrator transimpedance integrator amplifier circuit, where photocurrent from the photodiode is averaged over a long time period by the accumulation of charge upon an integrating capacitor (Burr-Brown, 1996).
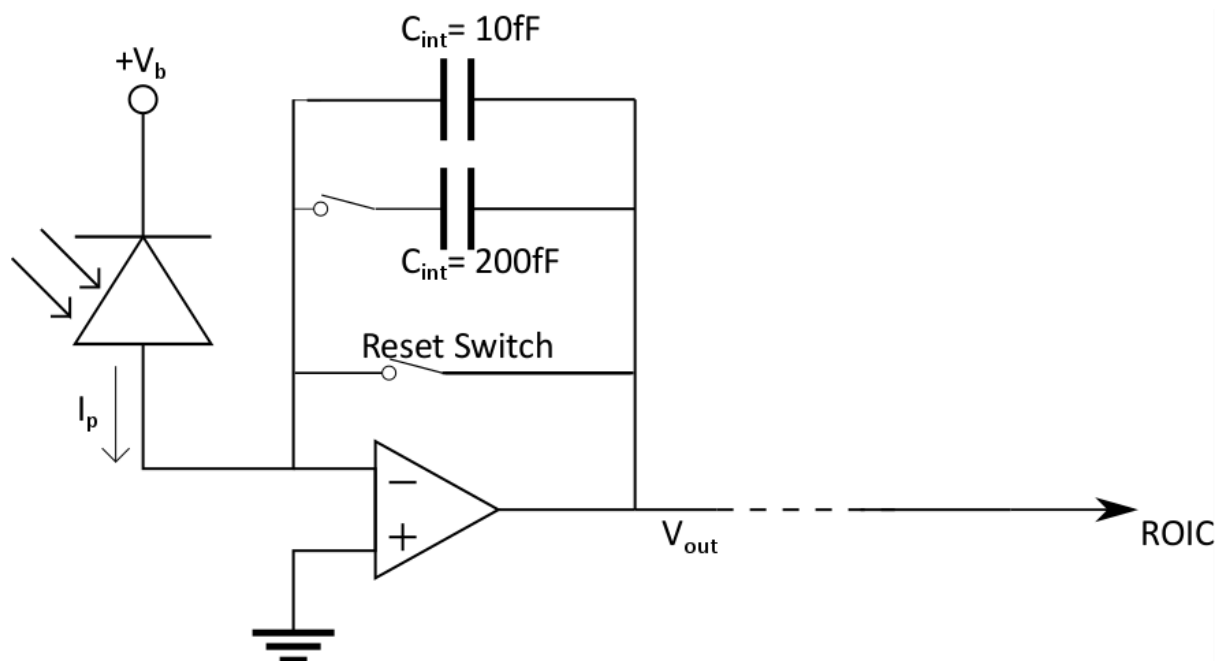
Figure 5.2 Inferred circuit diagram for the linear measurement of photocurrent from a photodiode elements in Xeva FPA camaera. Photocurrent from illuminated photodiode is integrated by a standard integrating TIA circuit, where the integrating capacitance element may be set to a large or small capacitance (low or high gain mode respectively), and readout by read out integrated circuit (ROIC) before discharge via reset switch.

The importance of the transimpedance amplifier element is to measure a linear voltage response for the photodiodes output current, which under constant reverse bias is itself expected to give a linear response with respect to the intensity of incident light. This output voltage leads to a build-up of charge on an *integrating capacitor*, unique to each pixel. The overall capacitance of this integrating capacitor may be set by the high and low gain modes of the operating software, which corresponds to either a single 10fF capacitor or an additional 200fF capacitor (210fF total) respectively). Build-up of charge is read non-destructively by a read-out integrated circuit (ROIC) after a user set integration time, and the integrating capacitor "reset" by discharging via a reset switch.

Note that unless otherwise stated, the low gain capacitor will be used in all experiments. The manufacturer notes that this capacitor reduces overall system noise (which is a combination of the op amp input offset voltage, input bias current and reset switch charge injection) at the expense of requiring greater integration times. This is in turn due to the much higher output conversion factor from approximately 16μV per electron to approximately 0.8μV per electron in the high and low gain capacitor modes respectively. Hence this mode is ideal for carrying out low light level measurements. (Xenics, 2013)

The ROIC is an analogue to digital converter which takes a user defined reference and range voltage (and   respectively) and places the readout voltage on a scale defined by   to a 12 bit resolution. Values for   and   may be optimised to achieve better measurement resolution.

This measurement may either be averaged across many frame exposures and output as a text file, or data from *all* frames may be retained in a video format file (consisting of a list of hexadecimal values for each pixel in the array, with pixel values from each new frame appended to this list). The latter method of data recording is used throughout this work in order to retain time-sensitive information. Values are always given up to a value of 4096 (12 bit resolution).

Proprietary measurement software provided with the camera allows this output data to have a 2-point calibration automatically applied to the data. This is useful for real time imaging of the ASE during alignment, however we will later choose to perform our own calibrations using the raw, uncalibrated video format data.

Dark current due to the reverse bias leakage current of the photodiode is unavoidable in this detection system, and will accumulate with longer measurement durations. The reverse bias dark current of the photodiode is reduced by active cooling of the detector with a thermoelectric cooler (maintaining a temperature of approximately 200K, according to the operating software). The remaining signal due to dark current is accounted for by measuring across at least one exposure (equal in integration time to that for a signal's exposure) where light from the device is blocked by an automated shutter along the optical path, at a distance from the spectrometer (e.g. between device and lens, see Fig. 4.5). While the entire detector system is used within a dark environment, we do not close the shutter of the spectrometer. This is to prevent the omission of stray light in the environment contributing to the dark reading.

5.4   Observing Detector Non-linearity

Initially, we investigated whether the system was behaving non-linearly due to non-optimal measurement conditions, i.e. response of the TIA to very low photocurrents generated at low light levels. To test this, we raised the background light level during the measurement of ASE from the S2 and S3 contacts of a typical segmented contact device. This was achieved by illuminating the slits of the spectrometer with a lamp source which emitted across a broad infrared spectrum. Where the detection system is linear, the background corrected ASE values for S2 and S3 should be unchanged.
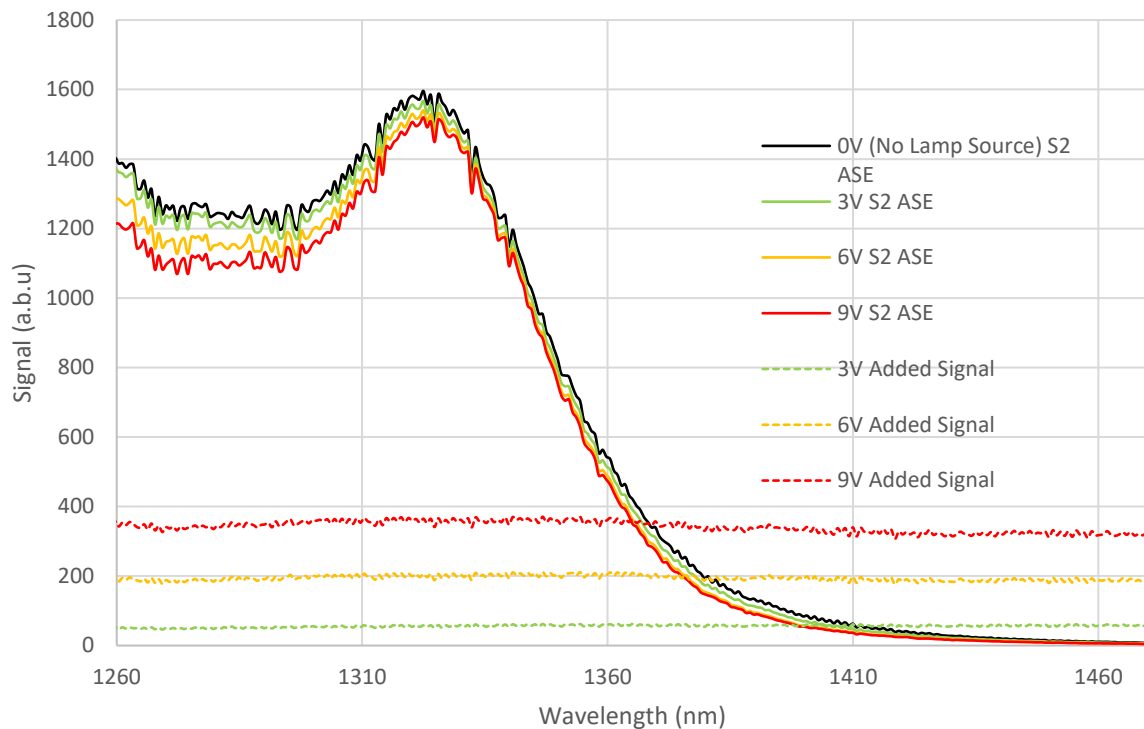
Figure 5.3 Background corrected signal for S2 ASE in the presence of additional illumination from an IR lamp source (see Added Signal). Added signal from lamp shown in above is background corrected with respect to a dark reading taken without IR lamp source.

In Figure 5.3 I demonstrated that by varying the operating voltage of an additional lamp source an apparent underestimate of the ASE signal with increasing background illumination occurs. To demonstrate this effect is not due to a drift of the measurement system with time, we include the effect of this added light upon the measurement of modal absorption. Assuming the ratio of S2 and S3 does not vary between measurements, this could be used as a measure of the non-linearity of the system with a change in the measured ratio of signals.
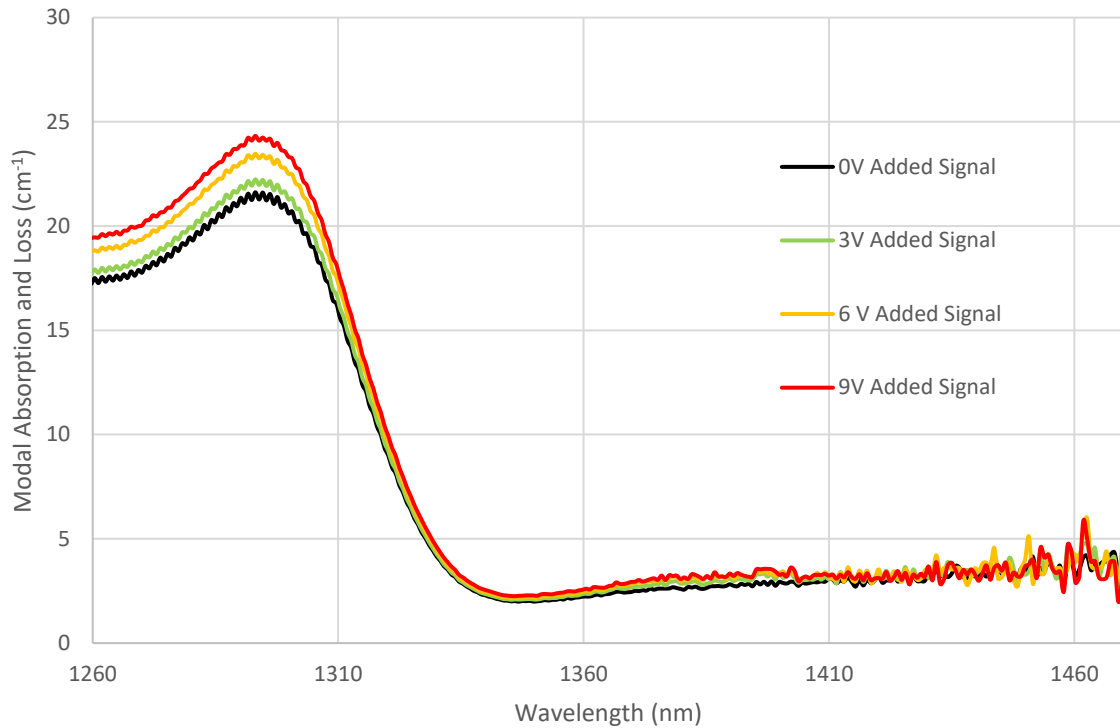
Figure 5.4 Modal absorption and loss spectra obtained in the presence of additional illumination from an IR lamp source, shown in Fig 5.3

The modal loss values at long wavelengths converge as the difference between ASE from S2 and S3 is reduced, and diverge both with increasing values of ASE and increasing difference in ASE between S2 and S3 (i.e. larger values of modal absorption). Assuming the non-linearity is not significantly dependent on wavelength, we surmise that the non-linear effect is present throughout the dynamic range used in the above experiment.

As the operating software provides the utility to perform and apply a two-point amplitude calibration to measurements, it suggests the manufacturer was aware of the need to calibrate the amplitude response of the detection system. This supports the need for calibration of this system. Disadvantages in the system's amplitude calibration tool is it is necessary to achieve complete and uniform illumination of the detector (requiring the disassembly of alignment sensitive components) and the inability to use more sophisticated calibration schemes. We will choose to apply an alternative amplitude calibration scheme which can determine the non-linear response curve of the detector to as high a precision as we require for the precise measurement of   .

Before attempting a calibration of the photodiode array, we consider which element of the detection system has introduced the non-linear behaviour in the hope of identifying experiment

parameters which may minimise its effect. For this, let us consider the elements of the detection system (introduced in Section 4.3) in reverse order (ROIC, integrating capacitor and photodiode).
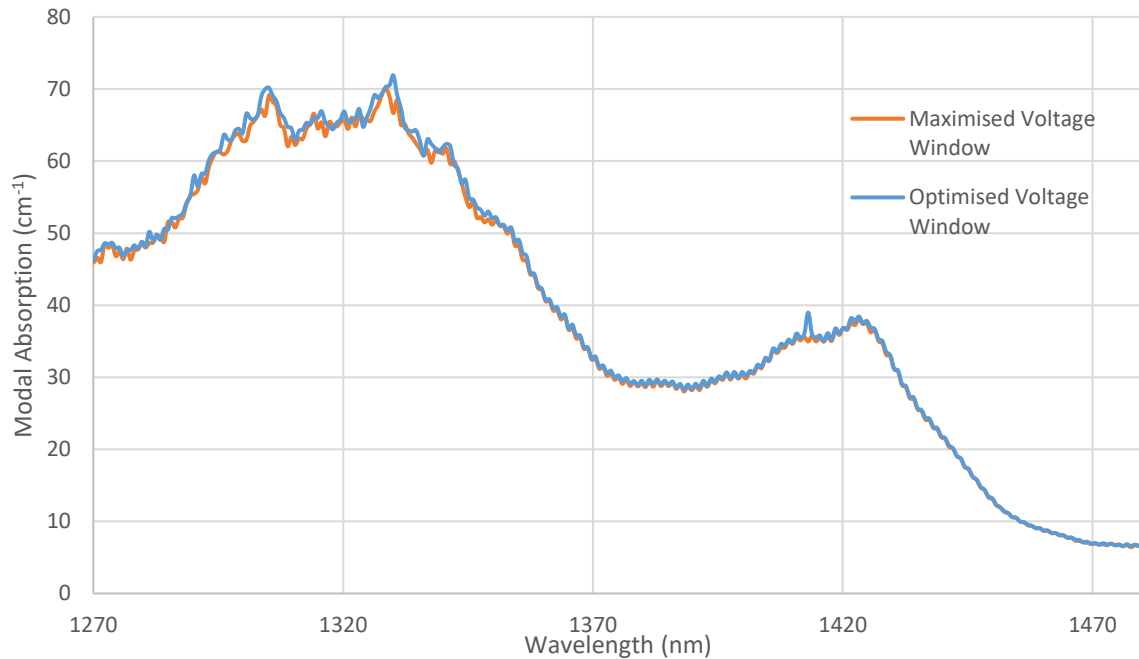
Figure 5.5 Modal absorption and loss spectra obtained when optimising the ROIC element for the dynamic range of voltages. Signal used ~60% and ~90% of total dynamic range of the maximised and optimised voltage windows respectively. Measurement performed for a different InAs QD sample from that of Fig 5.1-5.4.

Linearity of the ROIC element was tested by varying the voltage window (defined by settings and   ) and measuring the modal absorption and loss by SCM, as this is expected to give a constant ratio of light intensities throughout the experiment. A comparison of the maximum window *size versus* a window size equal to the dynamic range of the measured S2 signal showed no significant differences in their measured modal absorption and loss.
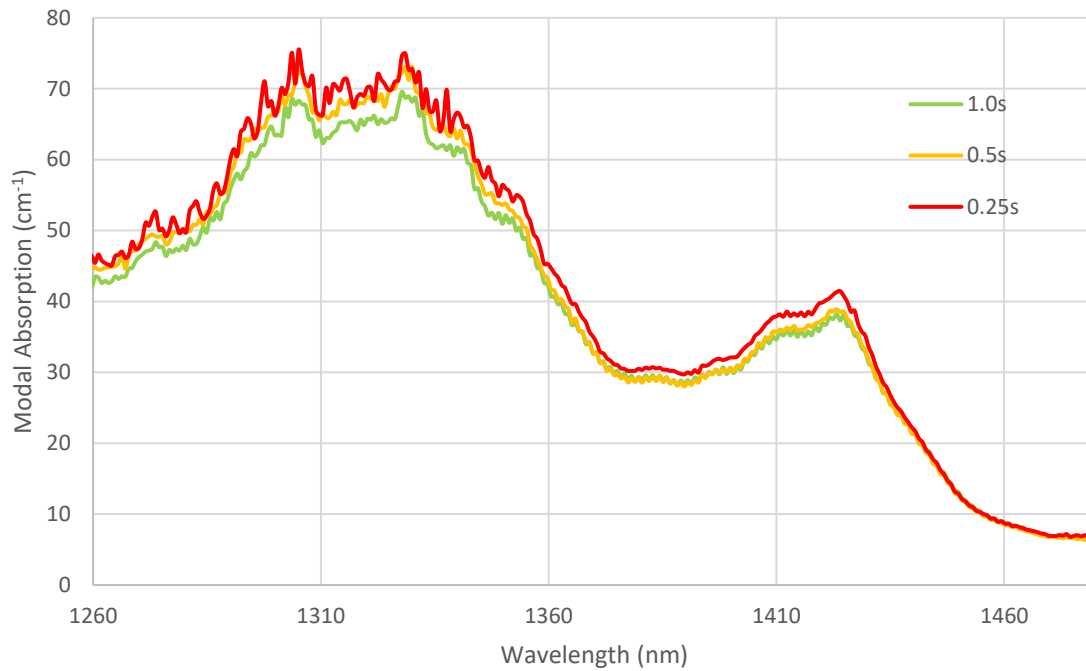
Figure 5.6 Modal absorption and loss spectra obtained by varying the frame exposure time, but while maintaining the same overall integration time of the experiment (120s).

The integrating capacitor of the detection system was interrogated by varying the total accumulation of charge before a reading was taken. This was performed by changing the integration time (i.e. the time before the voltage of the integrator capacitor is readout) while maintaining the same level of incident light from ASE. Changes to the integration time between 1.0 and 0.25s (while keeping the total overall integration time the same (120s) to give a similar level of precision) showed significant changes in the measured modal absorption and loss spectra. No trend towards linear behaviour was observed with increasing or decreasing integration times.

This suggests that the accumulation of charge by the integrating capacitor was *a* cause of non-linearity. This does not exclude other detector elements before this point, such as the photodiode or photocurrent measurement, from *also* contributing to non-linear behaviour. As we saw in Fig 5.3, a higher incident light intensity incident on the photodiode also leads to non-linear response. However, we will later see further evidence to suggest the integrating capacitor element is responsible for the observed non-linearity, when we compare the non-linearity of an experiment when using the low gain capacitor (used in Fig. 5.3-5.6) or the high gain measurement capacitor (Section 5.1).

As we were unable to determine experiment parameters which minimised the non-linear behaviour of the detection system, we describe a calibration method which accounts for it.

5.5.0 Calibration by Flux Superposition

To correct for the detection system's non-linearity, we quantify the non-linearity with respect to signal measured across a row of pixels of the photodiode array using a modified approach to the method of flux superposition (Yang et al., 1994a). From the observed relationship between non-linearity and measured signal, we determine conversion functions for each pixel which, when applied to the measured signal, will give a linear response.

5.5.1 Other Amplitude Calibration Methods Considered

There are many methods with which the non-linearity of a system may be quantified. A common approach is to use the inverse square proportionality with distance of flux of a detector from a known lamp source, and observe the deviation from this trend when measured by the detector system. The disadvantage of this approach however is that it assumes the non-linearity of a detector system under the CW light of a lamp source will be the same non-linear response as that from a pulsed source (our segmented contact devices). As the ASE of segmented contact devices requires focusing using a microscope objective onto the spectrometer slits, the complexity of this approach would be significant.

In addition to this, it is preferable to perform the calibration over a dynamic range of signal intensities which closely matches that which will be measured when exposed to the ASE of a segmented contact device. Note that the light spectrum of the infrared lamp source shown previously in Fig. 4.3 is even across all wavelengths. A calibration using light of this spectrum would require both a large set of measurements which covers the peak values of ASE observed, as well as a large range of ASEs for low values where   is measured. Conversely, if the detector system's linearity were measured with ASE emission from the segmented contact device itself, the emission spectrum is well suited for providing signals at the peak emission wavelength and low signals where limited ASE is measured (e.g. at longer wavelengths). This approach would ensure a representative sample of calibration data is obtained in the minimum experimental time.

A ratio method (a form of which is applied in Section 4.4) can be applied to our optical set up by introducing neutral density filters into the path of the ASE emission. Provided the true spectral absorption of the filter is known, the non-linearity of the system may be quantified from the observed difference from this value in the measured absorption by the detection system.

In practice this experiment proved difficult. We hoped to determine the non-linearity of a single row of pixels of the array, however the alignment of the ASE incident with the photodiode array proved too sensitive to the introduction of additional optical elements (i.e. neutral density filter slides), complicating the analysis. Additionally, this method required the absorption characteristic of each neutral density filter to be well-known, determinable with another measurement system. This creates an undesirable dependency of the detector system being calibrated upon the calibration of yet another system. The flux superposition method avoids this problem.

5.5.2 Experiment for Flux Superposition

Flux superposition relies on one simple core assumption, that if a detector is linear, two signals which are measured independently to have values   and   , when superimposed and measured once more will give a value of   . Note that this is true when combining light intensities from *incoherent* light sources, as is the case for segmented contact devices which are emitting ASE, and *not* highly coherent laser emission.

Any deviation from the condition of superposition can be quantified as:

$$ \overline{} \tag{5.1} $$

For our detector system,   ,   and   would represent signals measured by a single pixel when light from sources   ,   and the superposition of   and   respectively. If measurements taken across the dynamic range of these signals is perfectly linear, then the value of NL will be zero. A positive value of NL would reflect an overestimate of   while a negative value an underestimate of

    .

A common scheme for applying this principle is to take a single light source, split the signal down two paths (and   ) with a beam splitter, use a filter wheel on each part to vary the intensities of each split signal, and superimpose the two signals using a second beam splitter. Shutters are then used to select signal combinations   ,   and   , and the filter wheels used to give a large set of signal combinations within the detectors dynamic range (Eppeldauer, 2003).

The advantage of this method is that variations in the signal originating from the source are applied equally to each signal combination. This is of course provided that any time variation in the source is small with respect to the time over which the three signals are measured. It is also easily automated, allowing a large set of   and   combinations to be measured. However, as discussed

with respect to the ratio method, introducing filters as part of the optical set-up prior to the spectrometer introduces an unwanted change in image position. This is compounded by the additional complexity of the splitting and recombining of signal from a source which is in itself difficult to align.

Our solution to this is to superimpose ASE from two separate SCM devices (Fig. 5.7). We will define these as the target source and the calibration source. The target source will be the device we hope to measure following the calibration of the detector, while the calibration source may be any device with a similar intensity and spectral distribution as the target device. A segmented contact device from the same wafer which has not passed the quality assessments described for use in SCM (Section 3.4.4) makes a convenient calibration source, as this is sufficient to achieve a similar emission spectrum.
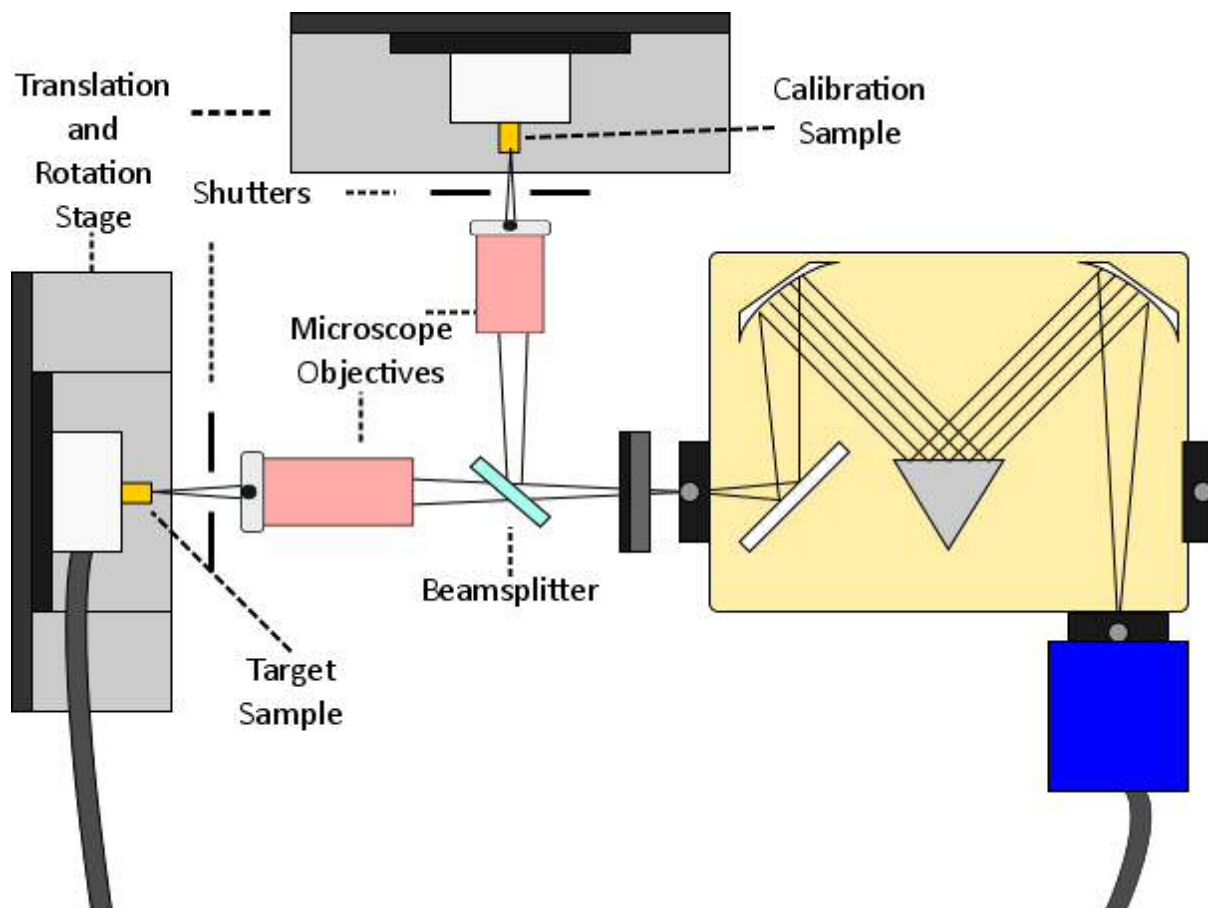
Figure 5.7 Experiment setup for calibration of detector pixels. Unlabelled components expanded on in Fig. 3.7

Both the target and calibration samples receive pulsed current from two separate pulse generators. The intensity of the target and calibration sources may then be changed by raising or lowering the current provided by each pulse generator. In addition, the second of these pulse

generators is triggered by the first, such that current to each device has the same pulse width, frequency and phase. This ensures that superimposed ASE are both incident upon the photodiode at the same time, as well as having the same pulse shaping characteristics as will be used during an experiment.

The target source is first aligned, as described in Section 3.4.5, and the calibration source is also positioned such that it's spectrally resolved output is superimposed over the first. Note that there are less stringent requirements for the alignment of the calibration source, as no assumptions are made as to the identical output of the two save that light pulses arrive in phase.

When satisfied with the alignment, the expected dynamic range of the target sample's peak intensity is estimated, based upon the SCM experiments intended after calibration of the detector. Assuming the rest of the spectral output will scale roughly with this peak emission, we vary the peak of the current pulse for the target and calibration sources in order to obtain non-linearity both for a range of different *total* intensities and *combinations* of intensities.
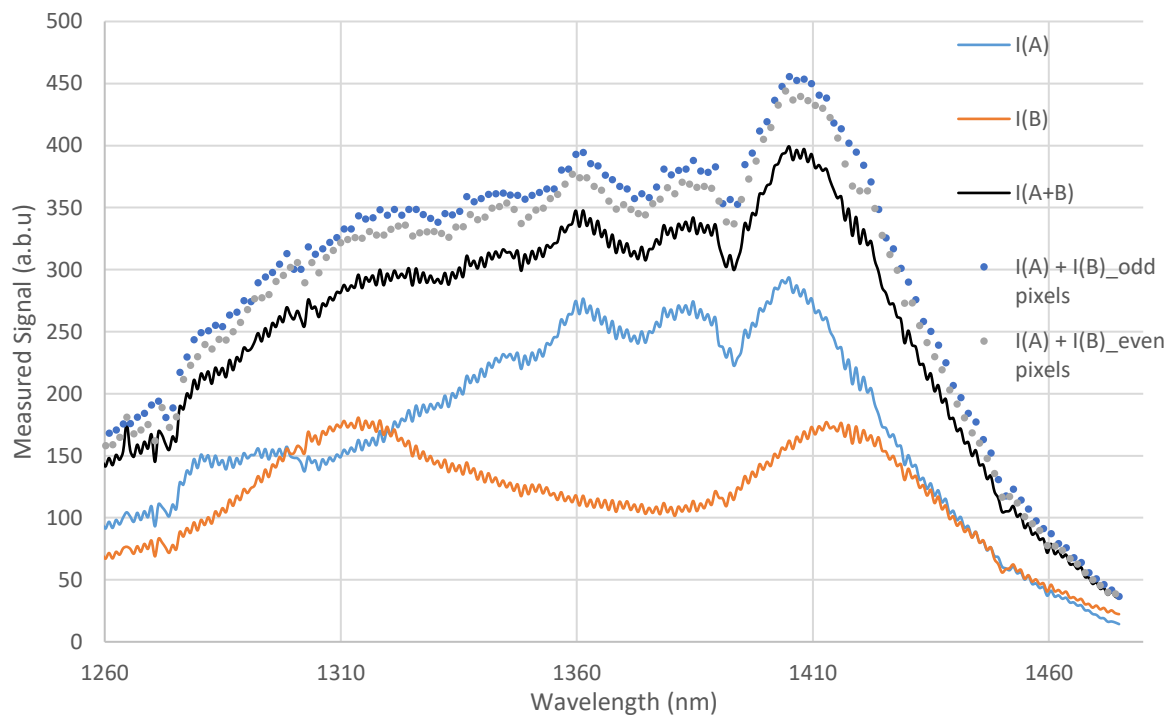
Figure 5.8 Example of a set of background corrected signals measured by flux superposition, with the ideal I(A) + I(B) values plotted for comparison (showing a consistent underestimate in the measured I(A+B) measurement). A consistent difference in the apparent non-linearity of alternating pixels is also observed

In this experiment, we make at least six sets of measurements of the target, calibration and superimposed sources and a dark reading (subtracted from the three preceding measurements) (24

separate measurements in all). An example of one set of measurements and the discrepancy between the expected and obtained values of _____ is given by Fig. 5.8. The peak intensities of the measured signals are used to determine currents for the calibration and target sources which result in an even distribution of signal intensities throughout the dynamic range of the target sample's peak emission. In this work, a sufficient spread of intensities is obtained where the peak output from the calibration source is approximately half of that of the target sources, although a variety of other signal ratios may be used. The total non-linearity of these measurements is then quantified by Eq. 5.1.

5.5.3 Fitting of Calibration Constants

So far we have discussed the measurement of non-linearity in the detection system by the method of superposition. Here we describe how the conversion function required to achieve a linear measurement is determined for each pixel being calibrated.

Our conversion function begins as a general form 3rd order polynomial. This was chosen partly for computational simplicity and with the knowledge that higher-order polynomials will be more sensitive to uncertainty in the calibration signals (Yang et al., 1994b):

$$(5.2)$$

where _____ is our uncalibrated, raw signal as measured by a single pixel.

For each raw signal, a background reading has been subtracted. This has the effect that our conversion function and signals must agree at zero. In doing so, we assume that the non-linearity of the system is not significantly affected by variations in the dark reading. Given this approach, it is reasonable to remove the ____ component __, introducing __ as our *background corrected signal* with a new set of calibration constants.

$$(5.3)$$

This polynomial may be reduced further when we consider that we only require the removal of *non-linearity*. The absolute scaling of the conversion function can be ignored, as the SCM is concerned only with the ratio of two signals. In this case, it will be the *ratio* of the calibration constants of Eq. 5.3 which are important. Note that the non-linearity quantifying function (Eq. 5.1)

can also be shown to be invariant under different scaling factors. As a result we can define a new set of calibration constants, — and —, to give the new function:

$$\qquad \overline{\qquad} \qquad\qquad\qquad\qquad\qquad\qquad\qquad\qquad\qquad\qquad (5.4)$$

which retains the form of a 3rd order polynomial, but with an intercept set to zero and, as ratios are invariant with the absolute scale, the component is effectively set to equal .

A python program was written for the purpose of finding the values of and of the conversion functions for each pixel along a single line of the photodiode array. For each pixel, a two dimensional array of and values is generated, and their resulting conversion functions (Eq. 5.4) are applied to the experimentally determined values of , and determined by the superposition experiment. For each set of , and values, a residual is found using the equation for NL, Eq. 5.1. Each of the six or more sets of residuals obtained from the superposition experiment are summed to find the residual sum (Eq. 5.5).

$$\qquad\qquad\qquad \overline{\qquad\qquad\qquad} \qquad\qquad\qquad\qquad\qquad\qquad\qquad (5.5)$$

The optimum values of and are those which minimise the residual sum. Note that it is possible to add a weighting to this non-linearity residual sum based on the observed SNR of the system. This approach is not taken, pending a thorough investigation of its benefits.

This process is repeated over two iterations, first using a coarse array of values for and ; followed by a smaller window size of finely spaced values for and , the range of values for which are informed by the first iteration. This method was sufficient for finding the calibration coefficients to high precision (i.e. up to the point that changes in incremental changes to the calibration constants resulted in changes to the absorption spectra of less than 0.02cm^{-1}). The computation time for calibration of a single row of pixels across six sets of superposition measurements was of the order of 10 minutes using a standard PC.

An example conversion function generated by this method is presented in Fig 5.9, while the original and conversion function residuals used to obtain this function are presented in Fig 5.10.
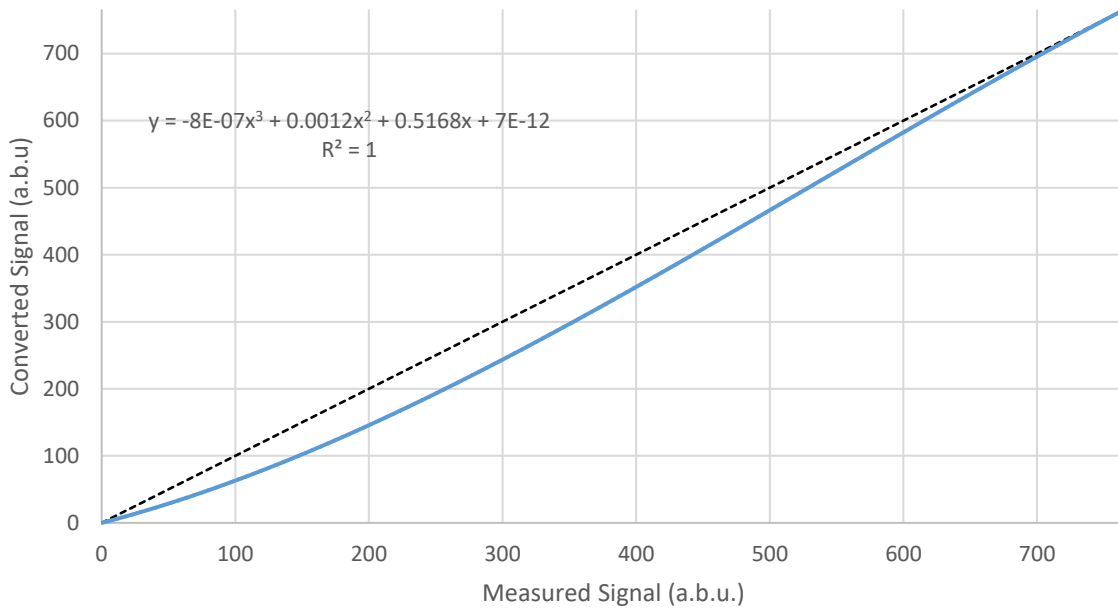
Figure 5.9 Example of a conversion function ($\sigma = 0.00234$, $\mu = -0.146 \times 10^{-5}$ in Eq. 4.4) derived from the above method. Dotted line is reference for 1:1 relationship between measured and converted values. Conversion function normalised to equal the maximum signal measured during calibration (indicating the dynamic range of the calibration). Trend line is a third order least squares fit function performed by Excel where the $R^2=1$ confirms Eq. 5.4 may be accurately described by a general form polynomial.
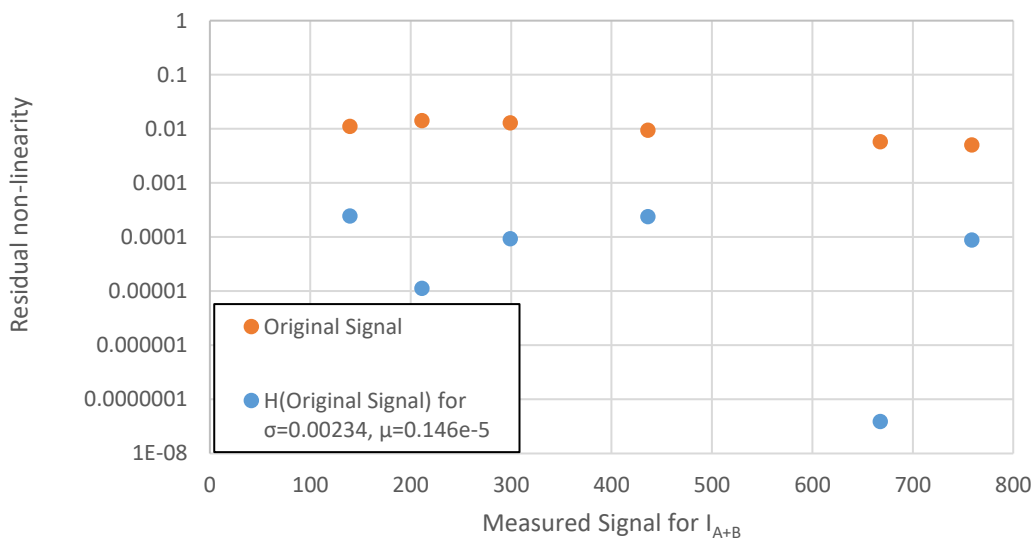
Figure 5.10 Demonstrated reduction in non-linearity residual used to determine the conversion function of pixel shown in Fig. 5.8. For comparison, note that measurement at corresponds to data obtained at wavelength of 1348.2nm in Fig. 5.8.

More complex iterative schemes (i.e. iterating until results converge within a certain tolerance) were not found to have a significant advantage. It is possible to obtain the best fits for constants   and   from the calibration data analytically using linear regression statistics. This

approach will have the advantages of reducing the computation time substantially, provide the most precise values of   and   , and also allow means for quantifying the confidence margins of the conversion function. The application of this analytical approach to the non-linearity equation given in Eq. 4.1 is outside the scope of work in this thesis.

5.6.0 Results from Calibration

We demonstrate the impact of calibration on the modal absorption and loss spectra obtained by the SCM by applying the method of flux superposition to two modal absorption and loss spectra obtained at different fractions of the overall ASE intensities. The intensity was varied by a very small reduction of the iris dimension (originally set to give a collection angle of 10°), to give approximately 20% reduction in peak ASE intensity. This method was chosen as it changed the alignment of ASE with the photodiode array the least. Signals from S2 and S3 for the purpose of this measurement were taken directly after a set of six calibration measurements of target, calibration, superpositioned and background measurements (I_A, I_B, I_{A+B}, and background). All calibration measurements were obtained from 50, 1s long frame exposures using the low gain capacitor, while the modal absorption and loss were found using 500s long integration of a series of 1s duration exposures using the modulated method described in Chapter 4.

In Fig. 5.11, the original modal absorption and loss spectra for the wide and narrow iris experiments are presented, as well as the absolute difference in modal absorption and loss between them. The ASE data used to obtain these spectra is then calibrated using the conversion functions determined for them by the superposition experiment. These calibrated ASE are used to calculate modal absorption and loss spectra presented in Fig. 5.11, as well as their new absolute difference.
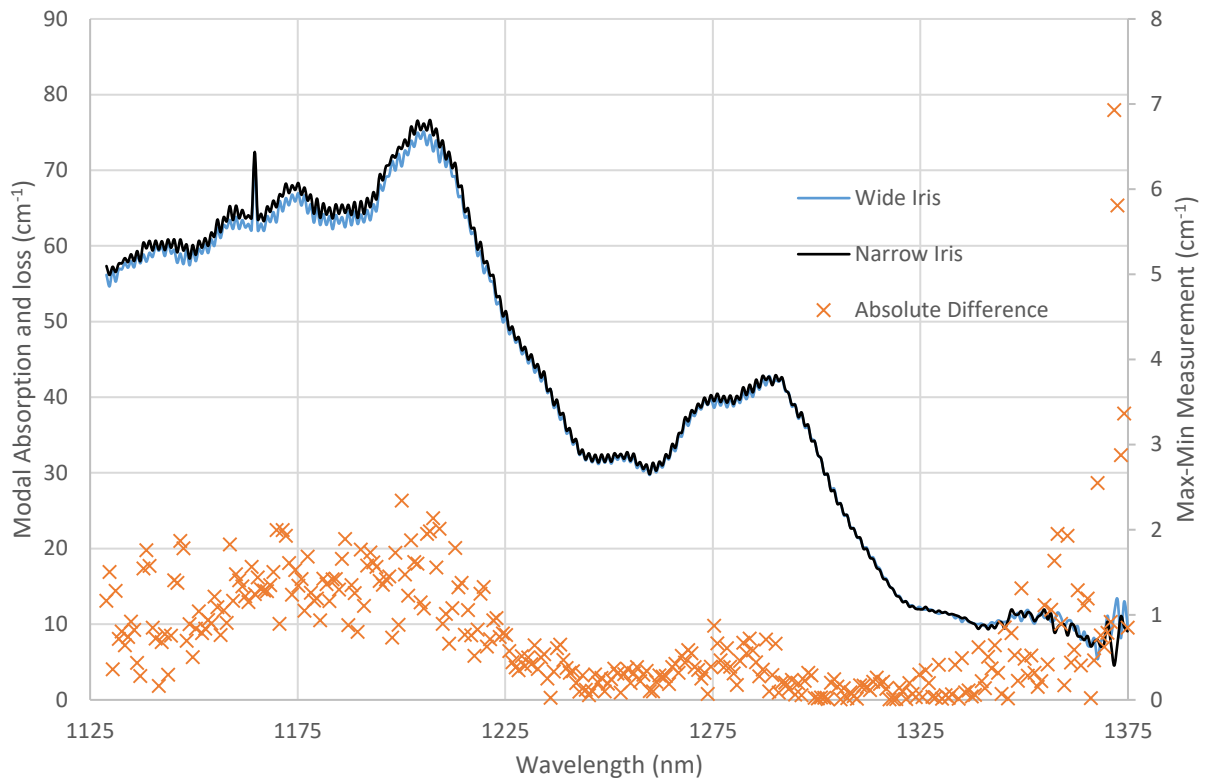
Figure 5.11 Uncalibrated measurement of modal absorption and loss for a segmented contact, ridge waveguide device fabricated from InAs QDs on silicon material at 100% and 80% of original ASE.
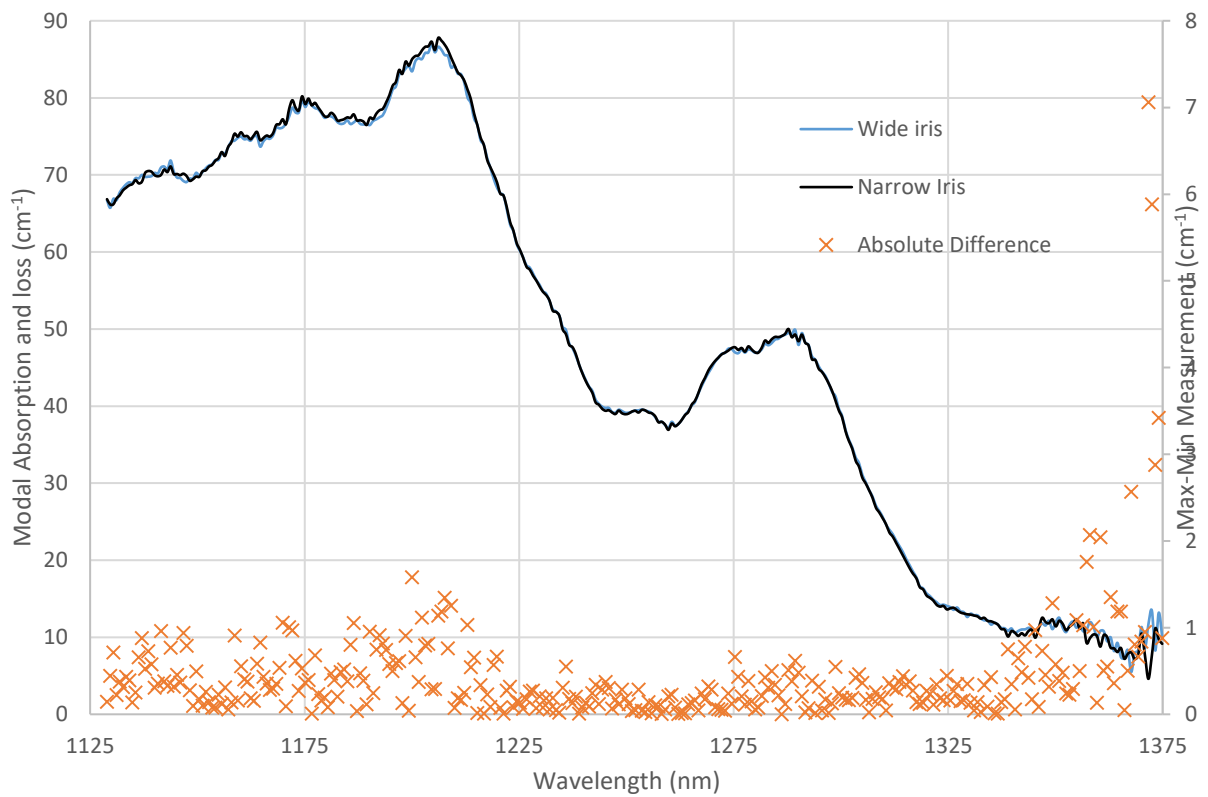
Figure 5.12 Calibrated measurement of modal absorption and loss for a segmented contact, ridge waveguide device fabricated from InAs QDs on silicon material at 100% and 80% of original ASE.

The primary goal of this experiment was to show a reduction in the discrepancy of measurements taken with different amplitudes of ASE by applying an amplitude calibration to the detection system. An improvement in the absolute difference of modal absorption and loss is most easily observed at short wavelengths where the difference in ASE from S2 and S3 is significant. This improvement decreases with decreasing modal absorption and loss values at longer wavelengths, where uncertainty in the measurement becomes the dominant factor. A small increase in the difference measured at approximately 1325nm in the calibrated data suggests uncertainty in the calibration (due to low SNR with longer wavelengths) has contributed additional error. This uncertainty may be reduced with longer integration times and a larger set of superpositions.

As well as showing better conformity between modal absorption and loss spectra measured at different ASE intensities, the alternating sensitivity of pixels (i.e. the "ripple effect") is apparently removed as well as an artefact due to a poorly performing pixel at approximately 1165nm. Note this confirms the ripple effect's origin as being the detector as opposed to the segmented contact device. This was originally confirmed by shifting the centre wavelength of the diffracted spectra with respect to the detector and finding the position of ripples were unchanged.

A significant increase in modal absorption and loss is also observed, particularly for large initial values of modal absorption and loss. We therefore conclude that the calibration has both better agreement in data, but also significantly reduces the noise due to varying sensitivity between pixels. It also suggests calibration is necessary to obtain the true magnitude of large values of modal absorption and loss.
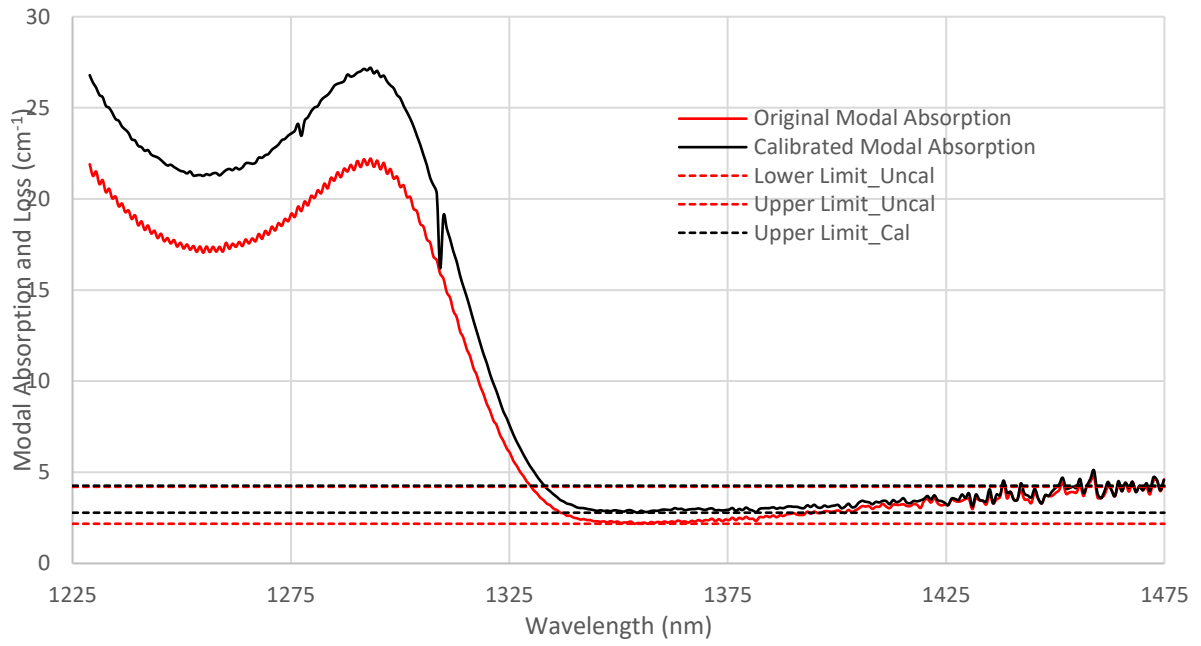
Figure 5.13 Modal absorption and loss obtained by SCM across long integration times for an InAs QD on GaAs substrate segmented contact device. Dotted lines added indicate approximate upper and lower limits of measured modal loss when uncalibrated (2.2-4.2cm^{-1}) and calibrated (2.8-4.3cm^{-1})

We apply this same method of calibration and subsequent modal absorption and loss measurement to the sample which originally motivated this work (Fig. 5.1), using the same method of flux superposition discussed in Fig. 5.13. In this case, nine sets of superposition calibration measurements were performed.

As seen in other calibrations, we observe a small change in the modal loss values where the difference in measured ASE is low. Where the differen in ASE is higher (nearer the band-edge)we see an increase in the minimum mode loss measured of 0.6cm^{-1} (Figure 5.13 at around 1350nm). As the value of α_i at the lasing wavelength is determined by extrapolation of the trend of α_i, it is crucial that this calibration is performed prior to extrapolation.

For the purposes of this experiment, we note that despite a reduction in the upwards trend in α_i below the band-edge, a significant wavelength dependence remains. This dependence is explored further in Chapter 6. Notably, the amplitude calibration has been shown to be crucial to understanding the nature of modal loss using this detector system, therefore a set of calibration measurements will be taken prior to all further experiments investigated in this thesis.

5.6.1 Comparison of Non-Linearity of detector system using High and Low Gain Capacitor Elements

Here we explore the non-linear behaviour of the detector system when using either a 210fF or 10fF integrating capacitor (low and high gain modes respectively) by quantifying the non-linearity using the method of flux superposition.

The experiment is carried out using six sets of measurements of flux superposition, with 50 frames of 1s exposures for each signal measured (background, I_A, I_B, I_{A+B}). In the case of measuring the behaviour of the high gain capacitor element, it was necessary to reduce the intensity of light incident upon the detector system by to approximately 25% of the original value. This was due to limits in the maximum readable voltage by the ROIC element. This reduction in intensity was carried out by reducing the iris dimension of lens and observing the change in peak intensity under low gain. This change could also have been brought about by reducing the exposure time by a factor of four, however for this experiment we wished to compare the gain capacitors under the same exposure conditions.

The residual sum of the non-linearity (calculated from uncalibrated signals using Eq. 5.5) is shown for all pixels along a row of the detection array.
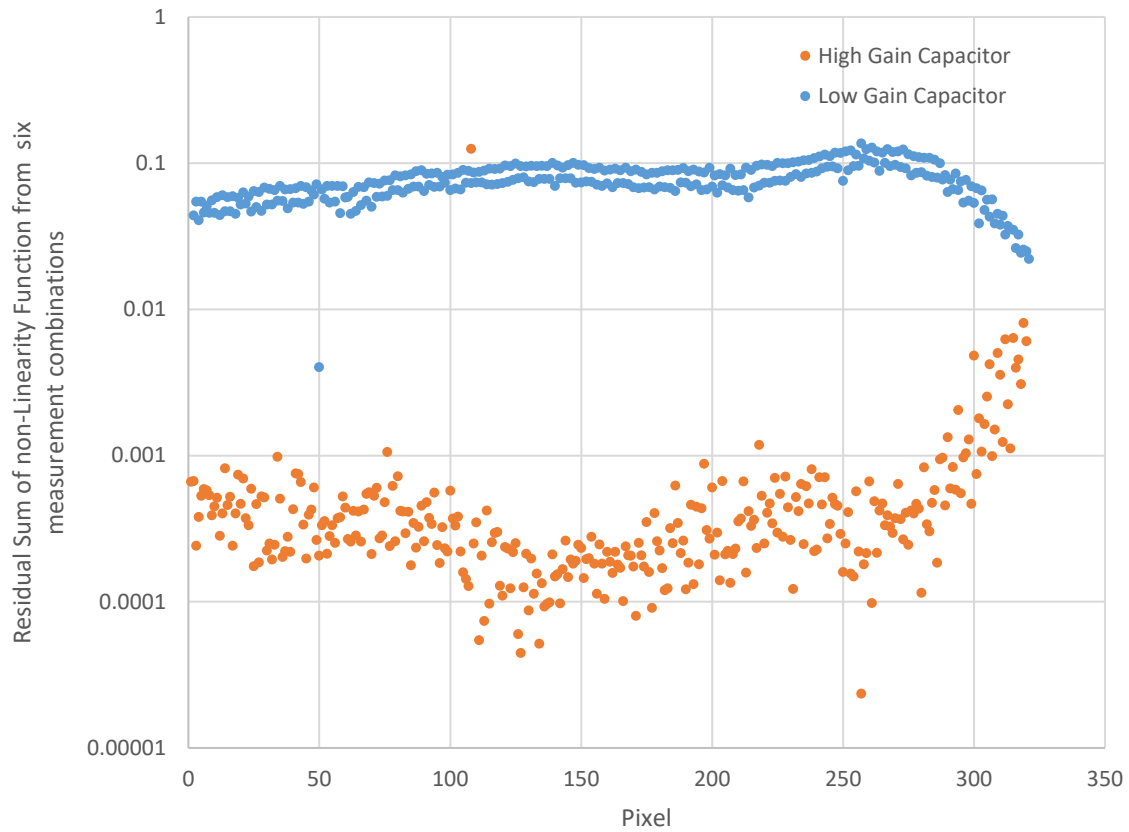
Figure 5.14 Non-linearities calculated from calibration signal generated using an InAs QD SCM device measured under high and low gain integrating capacitors. Intensity of incident light was reduced to accommodate for the sensitivity of the high-gain capacitor. Six sets of calibrations were taken, where each signal was measured across 50 frames with a 1s integration time

As well as possessing a much higher level of non-linearity, the low gain capacitor clearly demonstrates the alternating sensitivity of pixels, and how upon the application of conversion functions this feature is removed between Fig. 5.14 and Fig. 5.15.
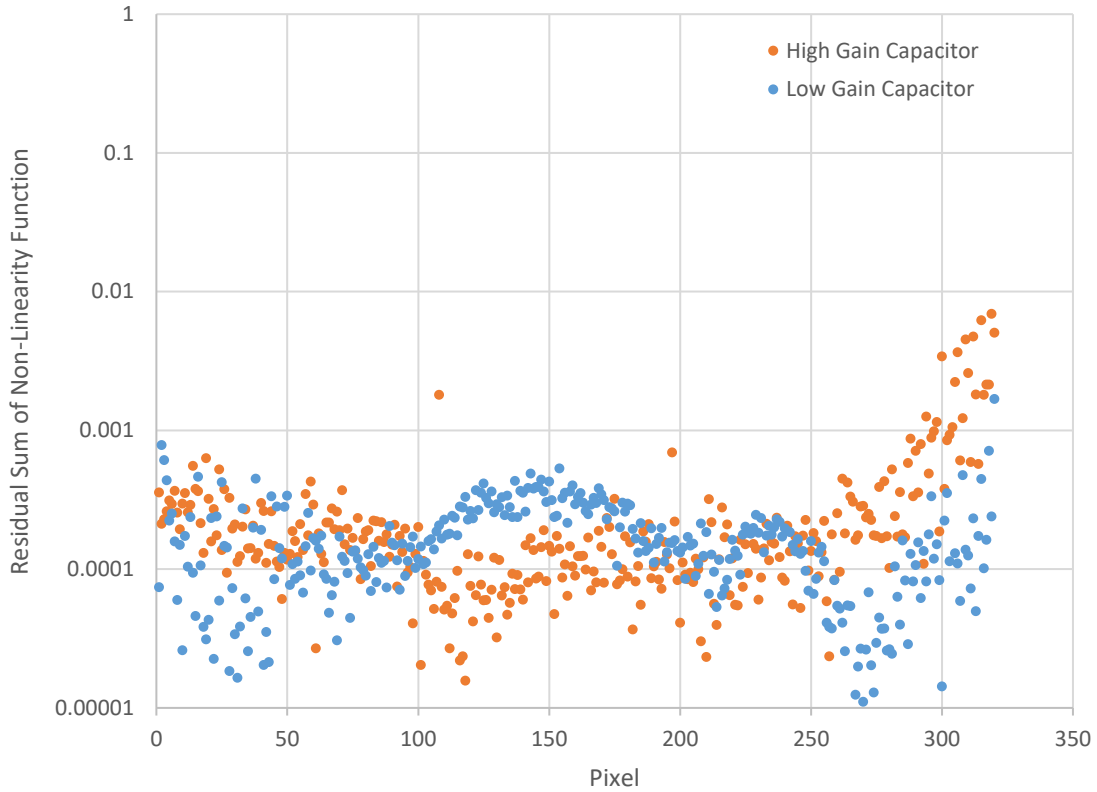
Figure 5.15 Non-linearities calculated after conversion function applied to data leading to Fig. 5.13 (same scale used), by the method described in Section 5.5.3

Removal of this non-linearity by the calibration method described shows a small reduction in the non-linearity of the high gain capacitor, but a substantial reduction in the low gain case. After calibration, the residual sums of non-linearities in both capacitor modes are comparable throughout the detectors range.

The impact of the choice of integrating capacitor used and the impact this has upon the measured modal absorption and loss spectrum was observed by immediately following the calibration of each capacitor with a measurement of the modal absorption and loss by the modulated method using the target sample. The target sample was a ridge waveguide, QDs on Silicon substrate segmented contact sample, as time restraints required that I complete this demonstration while investigating devices which were, unfortunately, not discussed further within this thesis. Due to the smaller width of these structures, a correspondingly smaller current was applied (20mA). For better comparison of the benefits of high and low gain capacitors, we mitigate the increased uncertainty due to lower light levels in the high gain measurement by increasing the total integration time by factor of 4 (2000s total integration time).
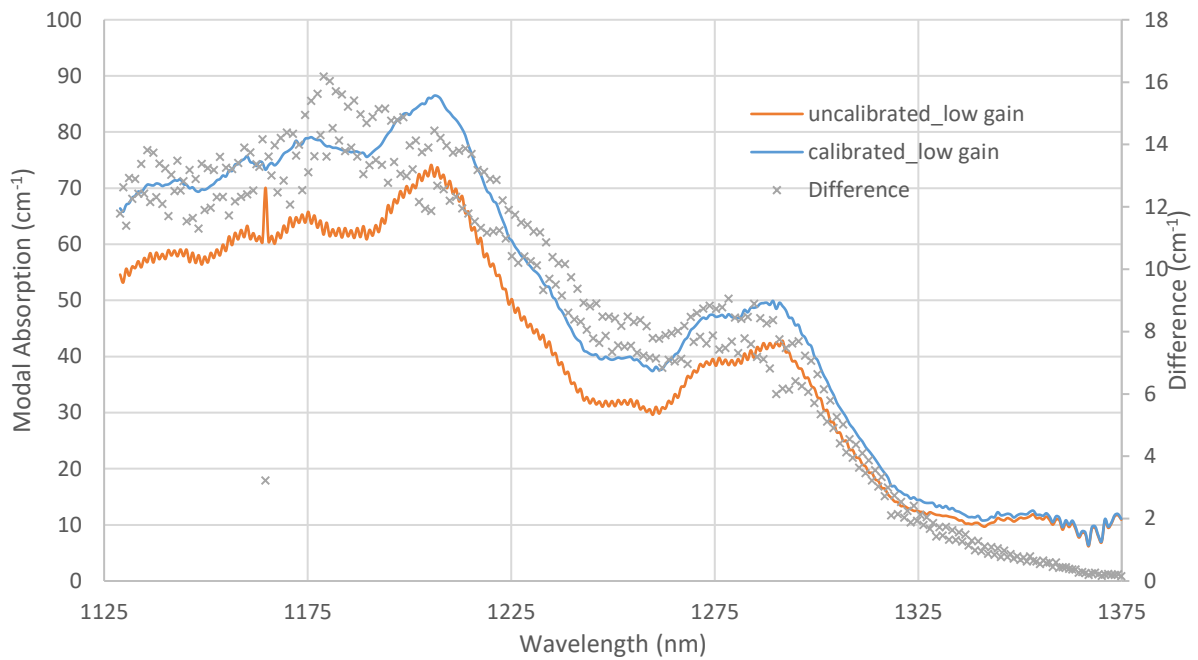
Figure 5.16 Modal absorption and loss spectra obtained using low gain capacitor element, before and after application of conversion functions obtained by calibration of flux superposition
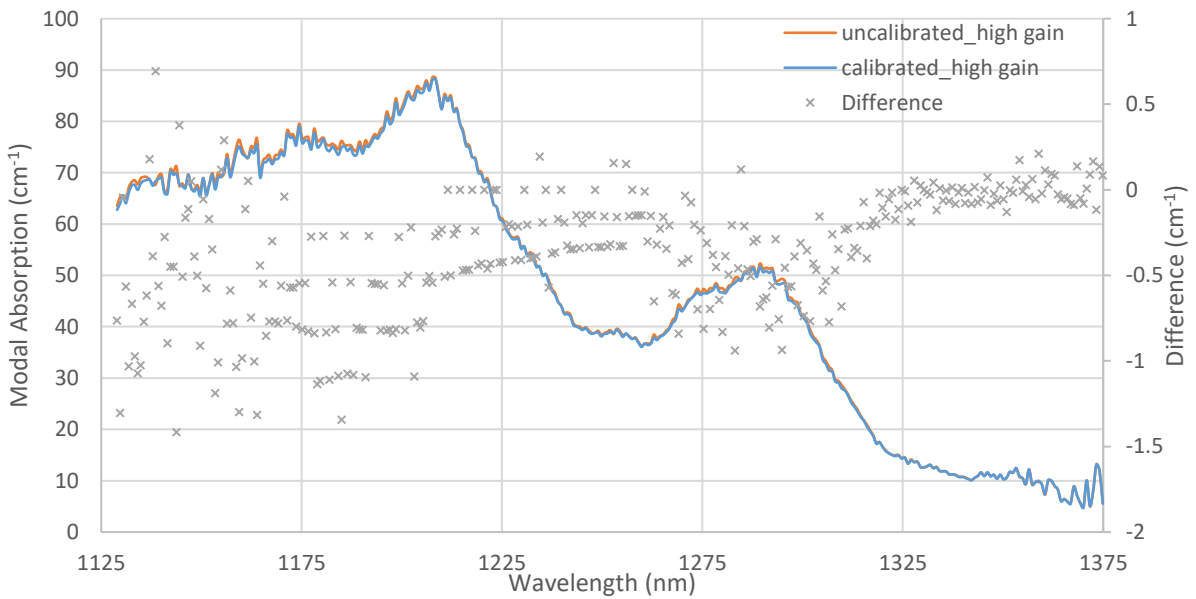
Figure 5.17 Modal absorption and loss spectra obtained using high gain capacitor element, before and after application of conversion functions obtained by calibration of flux superposition

The resulting modal absorption and loss spectra and their values after calibration (Fig. 5.16 and 5.17) demonstrates that changes in the measured modal absorption and loss are proportionate to the changes in non-linearity observed (Fig. 5.14 and 5.15). As such, a much larger change between the spectra of the low gain capacitor is seen than the high gain. We also observe that there is much

better agreement between spectra for small values of modal absorption and loss with low ASE (i.e. at long wavelengths) as this minimises the net difference between raw signals of S2 and S3.

For the high gain capacitor it is arguably unnecessary to perform the calibration when determining low values of modal absorption and loss, as the difference introduced by the calibration method tends to zero. However, without calibration there will remain an error throughout the modal *absorption* regions of the material of up to 1cm^{-1}.

The low gain capacitor meanwhile demonstrates a significant change even at long wavelengths, therefore calibration is always necessary to the measurement of   .

Despite similar effective integration times, the noise in the signal is dramatically reduced when using the low gain capacitor. This is in agreement with the manufacturer's recommendations for the detector system (Section 5.3). The impact of this noise within the above is that features of the short wavelength modal absorption have become exceptionally well resolved when using the high gain capacitor.

Noise notwithstanding, there is excellent agreement between the calibrated spectra of the low and high gain capacitors. This agreement is a strong indicator of the validity of the calibration experiment. This agreement can be regarded as resulting from reducing the non-linearity measurable by the two capacitor modes to a similar magnitude (Fig. 5.14). As a result, measurement of the residual sum of non-linearity of the detector can be used as a figure of merit for the linearity of measurements relying on this calibration.

The cause for the additional non-linearity exhibited by the low gain capacitor appears to be due to a consistent underestimate of the charge accumulated by the superpositioned data. This suggests the rate of charge of the low gain capacitor element decreases with increasing charge accumulation. It is unclear whether this occurs by design (although this is supported by the provision for 2-point calibration by the manufacturer's software) or whether this is due to a gradual degradation of the system.

5.7　Concluding Remarks

We have observed a non-linearity in the detection system used for the measurement of modal absorption by the SCM and identified the root cause of this non-linear response to be related to the integrating capacitor used in the low gain mode of the detection system. We have also developed a means for its correction through a new method of amplitude calibration by flux superposition. The method presented was sensitive to the requirements of spectroradiance detector systems. To our knowledge, there have also been no previous reports where flux superposition amplitude calibration has been applied to detector arrays.

This method of amplitude calibration has been shown to improve the consistency of modal absorption and loss data taken under different experimental conditions, particularly where the difference in compared signals is large. Where the differences in compared signals are small (e.g. modal loss values less than $3cm^{-1}$) we do not observe a significant change. Consequently we have shown that while the removal of non-linear behaviour causes a small change in the values of　, a significant upward trend in the below band-edge modal loss. This confirms that the upward trend observed is not caused by the non-linearity of the detection system.

We have also shown the flux superposition method is an effective means for comparing the non-linearity of light detection systems under different experiment conditions (in this case, using different integrating capacitor values). Within this detection system, we could investigate whether factors such as exposure time, forward bias applied to photodiode or position of ASE upon the photodiode array may be optimised to minimise the non-linearity of the system.

Despite the higher levels of non-linearity before calibration, we believe that with calibration the low gain mode of this detector system is the most suitable means for precisely measuring modal loss by the SCM. Comparison of modal absorption and loss spectra obtained by low and high gain modes demonstrates a reduction in random error with the use of the low gain mode (Figures 5.16 and 5.17), while the non-linearity measured in both systems is comparable after calibration. We expect some noise due to uncertainty in the calibration to remain in the signal. This can be mitigated by increasing the integration time of calibration measurements and using larger sets of measurements. In doing so, it may be useful to adapt a modulated approach to the calibration method, where rapid switching between measurements of　,　,　　and background would be expected to reduce sensitivity of the method to systematic drift.

XENICS, 2013. User Manual Xeva FPA Cameras ENG-2013-UMN002-R002. Belgium. *Issue 2*

Burr-Brown, 1996. Precision Switched Integrator Transimpedance Amplifier Dallas, Texas Texas Instruments Precision Switched Integrator Transimpedance Amplifier

Chapter 6   Waveguide Dependence of Optical Mode Loss

6.1   Introduction

In this chapter we will apply the modulated segmented contact method to the measurement of modal absorption and loss of two samples with differing waveguide core widths. We begin by giving the context and motivation for this work (Section 6.2). This is followed by a description of the two waveguide structures investigated (Section 6.3). Threshold currents and above-threshold behaviour of the two structures are measured, and their modal absorption spectra obtained by the modulated segmented contact method (Section 6.4). The FCA and IVBA of these structures is modelled and compared with the experiment data (Section 6.5). Ultimately, we will comment on the improvement in performance that is gained from changes to the thickness of the waveguide core, and the impact the new methodology had upon obtaining this result (Section 6.6).

6.2   Motivation

The waveguide dimensions and refractive indices of a laser determine the optical confinement of light within laser structures. As outlined in the Background Theory (Section 2.3.0), the overlap of the optical mode with the layers of the device will contribute to its modal gain, absorption and optical loss. The ideal waveguide design would minimise the overlap of the mode with absorptive layers (e.g. doped cladding) to reduce optical loss. It should also maximise the optical confinement factor as this will increase the modal gain and so reduce the current to achieve laser action for the same local gain. Within separate confinement heterostructures however, the ideal waveguide design must compromise between these considerations.
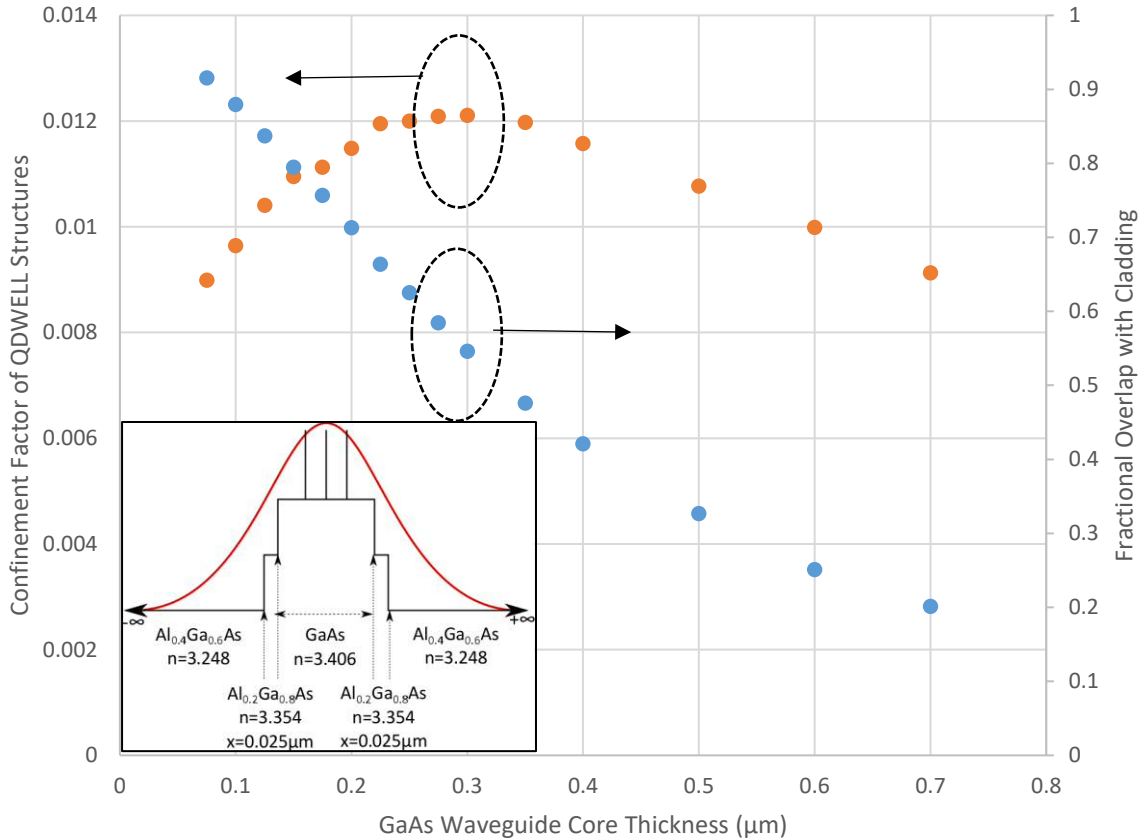
Figure 6.1 Modelled confinement factor (red) for three 80Å wide $In_{0.15}Ga_{0.85}As$ QW; and overlap with the doped cladding layers (blue), given a one dimensional model of the optical modes of a simplified GaAs:AlGaAs waveguide (see inset image) using the real components of refractive index only. Optical modes solved with a one dimensional mode solver (http://www.computational-photonics.eu/oms.html) and confinement and overlaps calculated from Eq. 2.7. Modelled for light with a wavelength of 1.3μm using dispersive relationships for refractive index given in Table 6.1.

Within this chapter we consider how the optical mode is affected by varying the waveguide core thickness only. In Fig 6.1, a simplified model shows that varying the waveguide core thickness has two competing effects: a narrower core will improve the confinement factor of light (until the core thickness is appreciably smaller than the wavelength of light within this medium); while a wider core will result in a smaller overlap of the optical mode with the doped cladding regions.

For the purposes of maximising net modal gain in the example given in Fig. 6.1, a core thickness of less than 0.300μm will not be beneficial. However, despite the decrease in the confinement factor above this value, it is possible that an increase in net modal gain could be achieved with core thicknesses greater than 0.300 μm. This depends upon the relative magnitudes of the *local* gain and loss of the core and cladding materials.

We are also interested in the core thickness due to its role in structures grown directly on Silicon substrates. There is a large lattice mismatch between the investigated devices (GaAs and AlGaAs with InAs QDs heterostructures) and Silicon, which introduces a large strain into the epitaxially grown material. For thinly grown devices, this strain is accommodated by an elastic deformation of the material. With increasing thickness however it becomes more energetically favourable to form defects in the crystal structure of the grown material. These defects form centres for the non-radiative recombination of carriers, and will tend to increase and propagate throughout the device's lifetime through the process of radiation enhanced defect reactions, contributing to reduced lifetime expectancy of the device. As device thickness is of critical concern to this process, reducing the waveguide core thickness may also lead to improved device lifetime performance. While the devices explored in this chapter were grown on GaAs, they are intended as test pieces for devices to be grown directly onto Silicon substrates.

In order to better inform the choice of waveguide core thickness, we aim to improve our understanding of the relationship with optical loss. We will achieve this by investigating samples fabricated with nominally identical structures utilising either wide or narrow waveguide core thicknesses (3740nm and 2440nm respectively). We will measure the resulting changes to device performance in the form of threshold current and above-threshold slope efficiency; and utilise the modulated segmented contact method to obtain their respective modal absorption spectra. From this we will determine the change in behaviour of optical mode loss.

6.3 Waveguide Structure

A generalised schematic of the two waveguide structures investigated is given in Fig. 6.2. Both structures are expected to result in laser emission with a wavelength close to 1.3µm, utilising the ground state emission of the InAs QDs. Differences in the waveguide core thickness between the two structures are given by an expanded view of the undoped core region in Fig 6.3.

Layer Thickness (Å)	Doping Concentration (cm^{-3})
3000	1e19
250	2e17
11000	2e17
1000	2e17-5e16
250	
Variable (see expanded diagram)	
250	
12000	2e18
250	2.4e18
10000	2e18
Substrate Lapped until overall structure approximately 100μm	2e18

Device layer structure (top to bottom):

AuZn Top Contact

Insulating SiO$_2$ — Insulating SiO$_2$

p-type GaAs

p-type Al$_x$Ga$_{1-x}$As (x=0.2) Cladding

p-type Al$_x$Ga$_{1-x}$As (x=0.4) Cladding

graded p-type Al$_x$Ga$_{1-x}$As (x=0.4) Cladding

undoped Al$_x$Ga$_{1-x}$As (x=0.2) Cladding

Undoped Core Region (see expanded diagram)

undoped Al$_x$Ga$_{1-x}$As (x=0.2) Cladding

n-type Al$_x$Ga$_{1-x}$As (x=0.4) Cladding

n-type Al$_x$Ga$_{1-x}$As (x=0.2) Cladding

n-type GaAs

n-type GaAs Substrate (Lapped)

n-type GaAs Substrate (Lapped)

AuGe/Ni/Au Bottom Contact

Figure 6.2 Nominal growth and fabrication details of BA devices investigated in waveguiding study

The general structure of our samples is that of a separate confinement heterostructure, as discussed in Section 2.2.3. Optical confinement is achieved by contrasting the high refractive index of the core region against that of the lower refractive index cladding layers. Beyond the cladding regions are regions of high refractive index GaAs, completing what is effectively a 5 layer "W-type" slab waveguide. The graded doping profile of the waveguide was chosen to minimise the overlap of the optical mode with p-type dopants (see Section 2.3.3), where large local optical losses due to IVBA are expected to occur. The laser structure was designed by research group members Sam Shutts, Stella Elliott and Peter Smowton.

Layer Thickness (Å)	Wide Core Sample	Narrow Core Sample
Wide Core Sample: 1150 / Narrow Core Sample: 500	GaAs	GaAs
80	$In_xGa_{1-x}As$ (x=0.15) QW with embedded InAs QDs	$In_xGa_{1-x}As$ (x=0.15) QW with embedded InAs QDs
600	GaAs	GaAs
80	$In_xGa_{1-x}As$ (x=0.15) QW with embedded InAs QDs	$In_xGa_{1-x}As$ (x=0.15) QW with embedded InAs QDs
600	GaAs	GaAs
80	$In_xGa_{1-x}As$ (x=0.15) QW with embedded InAs QDs	$In_xGa_{1-x}As$ (x=0.15) QW with embedded InAs QDs
Wide Core Sample: 1150 / Narrow Core Sample: 500	GaAs	GaAs

Figure 6.3 Expanded growth details for core region of wide and narrow core width samples

Within the core, gain is achieved by three layers of InAs QDs, embedded in $In_{0.15}Ga_{0.85}As$ QWs (DWELL structure, Section 2.2.4). The overall thickness is changed by varying the width of the surrounding GaAs layers from 1150Å each to 500Å.

Note that while the overall thickness of the core is changed, the inter-DWELL distance between layers of QDs is nominally identical. This is to ensure the only difference introduced between these structures results from the confinement of light by the different waveguides (Section 2.2.4).

6.4.0 Device Measurements

Material was grown in two wafers based on the designs outlined in Section 6.3, and fabricated into multiple BA lasers (see Section 3.2) with lengths of 1, 2, 3 and 4mm and oxide-isolated stripes of 50µm wide, as well as multiple BA segmented contact devices (each with seven 300µm contacts, Section 3.5).

I determined the threshold currents for the above BA lasers were by extrapolation of the above-threshold L-I curve, while their above-threshold slope efficiencies were determined from the P-I curve measured by an integrating sphere (Section 3.3.1). Lasing wavelengths were measured for devices when driven just beyond the point of threshold current (5mA above this level), using the

optical setup described for the segmented contact method (Section 3.4). In all of the above experiments, devices were measured under pulsed conditions, with a pulse width of 1000ns at 5kHz.

Lateral spreading of current beyond the 50µm width top contact was accounted for by measuring the FWHM of the imaged nearfield emission at 5mA above the respective threshold currents, with respect to the dimensions of the facet. This was used to determine the threshold current densities (Table 6.1). External differential quantum efficiencies were calculated from measured slope efficiencies and the corresponding lasing wavelengths measured for each device.

Cavity Length (mm)	Narrow Waveguide Core J_{th} (Acm^{-2})	Error (Acm^{-2})	Wide Waveguide Core J_{th} (Acm^{-2})	Error (Acm^{-2})
1	734	10	448	8
2	201	4	153	3
3	137	2	157	2
4	144	2	186	3

Table 6.1 Lowest obtained values of threshold current densities measured across several BA laser devices. Threshold current densities takes account of current spreading measured from lasing nearfield emission. Errors obtained from error in linear fit to data.

Values presented in Table 6.1 represent the lowest threshold current densities obtained for measurements of four devices for each of the 1, 3 and 4mm cavity lengths for each waveguide structure. In the case of 2mm cavity lengths, as many as eight samples of each waveguide structure were measured.

Both 1mm long devices exhibited significantly higher threshold current densities than other lengths measured. However, these devices also exhibited a significantly shorter lasing wavelength: 1.207µm and 1.210µm for the 1mm narrow and wide waveguide cores respectively; while 1.305-1.302µm and 1.309-1.308µm for the 2-4mm long narrow and wide waveguide core samples respectively. No trend in wavelength was observed with increasing cavity length in the 2-4mm devices.

We believe that the much shorter wavelengths, and much higher threshold current densities, of the 1mm devices indicate a change from laser emission utilising the ground state of the InAs QDs (as in devices 2mm and longer) to utilising the first excited state. This suggests the greater mirror loss

of 1mm long laser devices increases the threshold gain requirement to a value which is achievable with high current densities in the first excited state emission, but not in the ground state.

The more rigorously tested 2mm long devices demonstrate a higher threshold current density in the narrow core waveguide structures than in the wider core (153Acm^{-2} and 201Acm^{-2} respectively). For longer narrow waveguide structures the threshold current densities are lower. This is consistent with lower threshold gain requirement due to reduction in mirror loss with increasing cavity length. However the 3-4mm long wide waveguide core samples contradict this behaviour.

We have greater confidence in the threshold current densities obtained from the best performing 2mm long devices as these drew from a larger set. At least two samples were identified from each set of narrow or wide waveguide samples which achieved the lowest threshold current densities (agreeing to within 7Acm^{-2}). The 3-4mm long samples however drew upon a much smaller set size, such that the quality of samples selected for comparison in Table 6.1 are likely to be variable.

Given the significant changes to device behaviour for 1mm long cavities we will restrict further investigations to the 2-4mm samples only. We also note that values for   at the lasing wavelength will be determined at wavelengths of 1.303μm and 1.3085μm in the narrow and wide waveguide core samples respectively.
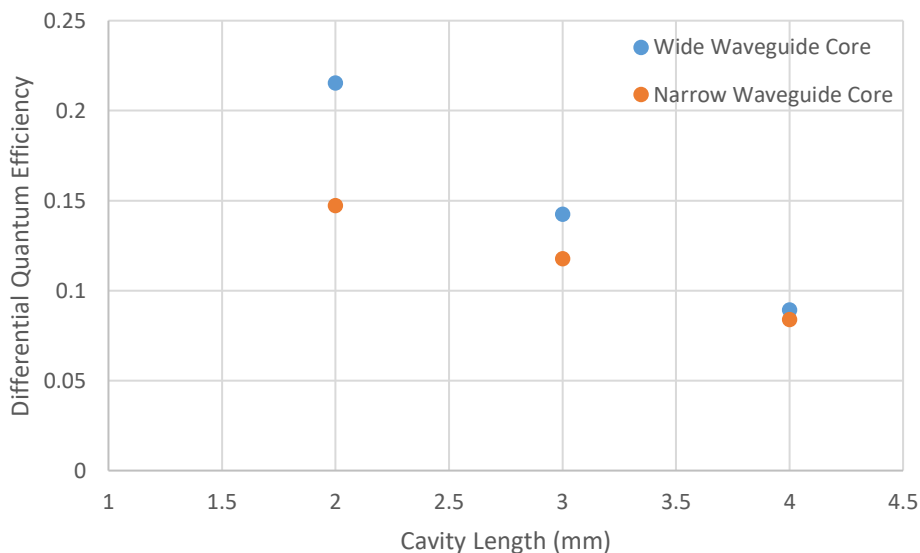
Figure 6.4 DQE measured for wide and narrow waveguide structures for sample lengths of 2, 3 and 4mm, from devices exhibiting the best threshold current density performance presented in Table 6.1

DQE measured from the described BA lasers had insufficiently low scatter from which to determine values for the internal differential quantum efficiency and optical mode loss. However the

above comparison shows a clear trend. The DQE of the wide waveguide core samples is consistently higher (Fig 6.4), particularly in the more thoroughly tested 2mm cavity length samples. This result is indicative of either higher internal differential quantum efficiency, lower optical mode loss or both. The presence of a clear trend in the DQE measurement for both narrow and wide waveguide structures, and the weaker trends observed in the values of threshold current density, imply that the quality of facets was variable, particularly in the case of wide waveguide structures.

6.4.1 Repeatability of the Modulated Segmented Contact Method

We now apply the modulated segmented contact method described in Chapter 4 to precisely measure the modal absorption spectra of narrow and wide waveguide structures. We will use two standard segmented contact devices for each waveguide structure (which have passed the conditions for quality laid out in Section 3.4.4). Following calibration of the detector, each device is measured under the same conditions: 80mA current pulse with 1000ns width and 5kHz frequency. This current is regarded as being both reasonably high for the contact area being pumped, but not so high that damage to the top contacts of the device could occur. The low duty cycle is used to prevent self-heating of the device.

Signal is integrated across 1500 camera exposures, with a switching period of 7.5s, and background sampling after eight cycles of switching (as seen in section 4.3). Length of individual exposures is set to 1s. We will consider the repeatability of the measurement within the range of wavelengths typically used for determining the optical mode loss of devices emitting at 1.3μm, using a spectrometer centre wavelength of 1350nm.
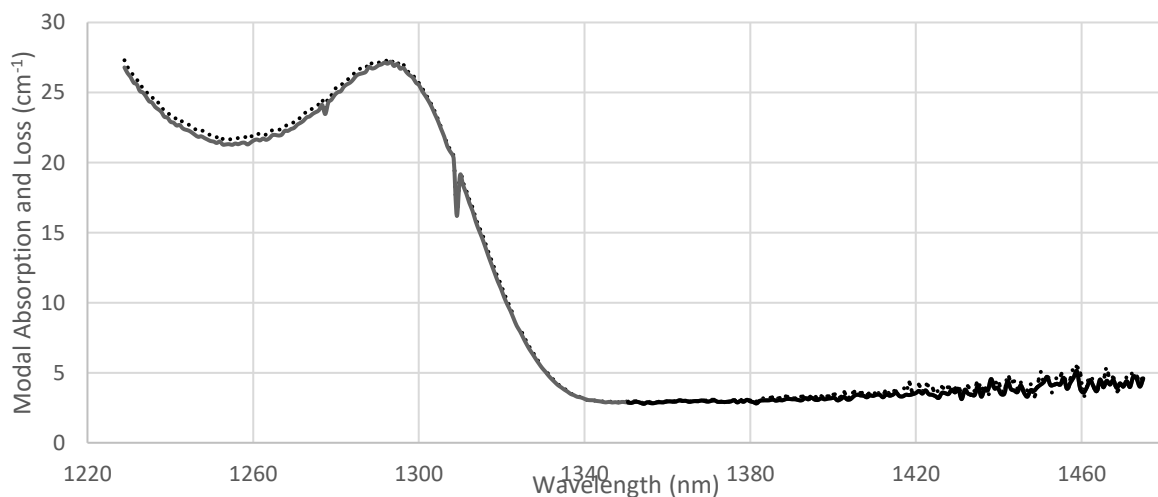
Figure 6.5 Modal absorption spectra obtained from two segmented contact wide waveguide structures (solid and dotted data represent samples 1 and 2 respectively)

In the two wide waveguide core samples (Fig 6.5), the modal absorption spectra measured between Samples 1 and 2 in the range from 1320nm and 1380nm are well matched. There is a small deviation in the magnitude of the peak absorption between the two modal absorption spectra (1290nm). This is located at the suspected ground state emission of the InAs QD distributions.

The differences observed are consistent with a 1° uncertainty in the device's rotational alignment with respect to the polariser (InAs QD emission and absorption is strongly polarised in the TE direction). This uncertainty is due to the low resolution of the image of nearfield signal generated by the photodiode array used to determine device orientation with respect to the detector. However, where the absorption is not strongly polarisation dependent (free carrier absorption), small variations in polarisation orientation are not expected to have a significant impact upon the measurement. This uncertainty could be addressed by aligning the nearfield of the device with respect to reference points on a higher resolution camera. It is also possible that the variation in peak absorption is due to a change in the density of QDs from sample to sample. It would also be consistent with the systematic drift which remains in the modulated approach.

Artefacts in the spectrum at 1277nm and 1309nm are related to poorly performing pixels of the array which were not sufficiently well calibrated.
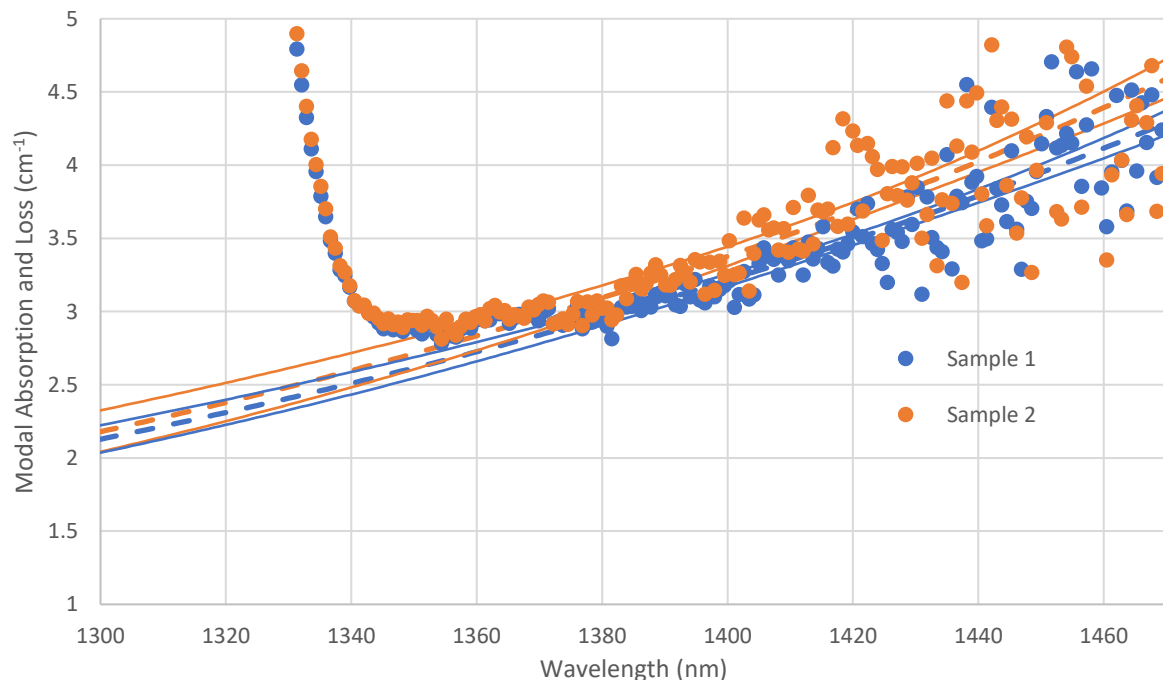
Figure 6.6 Expanded view of modal absorption spectra below the band-edge obtained from two segmented contact wide waveguide core structures (blue and orange data represent samples 1 and 2 respectively). Exponential fits and confidence values are obtained from data below 1370nm.

Small deviations in the spectra are also observed below 1380nm. They are consistent with variations in the modal absorption spectra observed between trials of the modulated method in Chapter 5, i.e. due to systematic drift. The optical mode losses at 1308.5nm for Samples 1 and 2 are $(2.20\pm0.11)cm^{-1}$ and $(2.26\pm0.16)cm^{-1}$, where errors are determined from the 95% confidence intervals discussed in Section 4.2 and added to the residual systematic error of $0.02cm^{-1}$ discussed in Section 4.4.
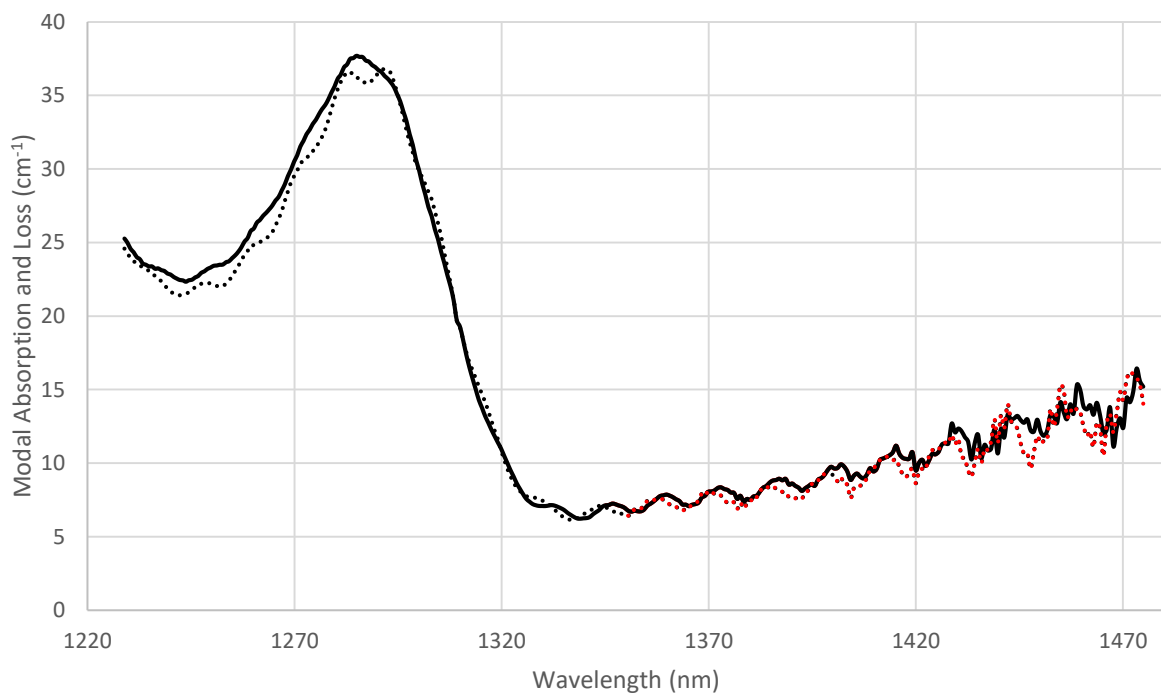
Figure 6.7 Modal absorption spectra obtained from two segmented contact narrow waveguide core structures (solid and dotted data represent samples 1 and 2 respectively)

In the narrow waveguide core samples (Fig. 6.7), we observe what appears to be a sinusoidal variation in absorption, acting in addition to a similar modal absorption and loss curve to wide waveguide cores. The phase of this variation appears to vary from sample to sample, in the below case a shift of about a ¼ period is observed. We will consider reasons for this feature and its variation between devices in Sections 6.5.

Differences in the magnitude of the peak modal absorption are observed, and are once more believed to be due to either small variations in rotational alignment or differences in density of QDs.
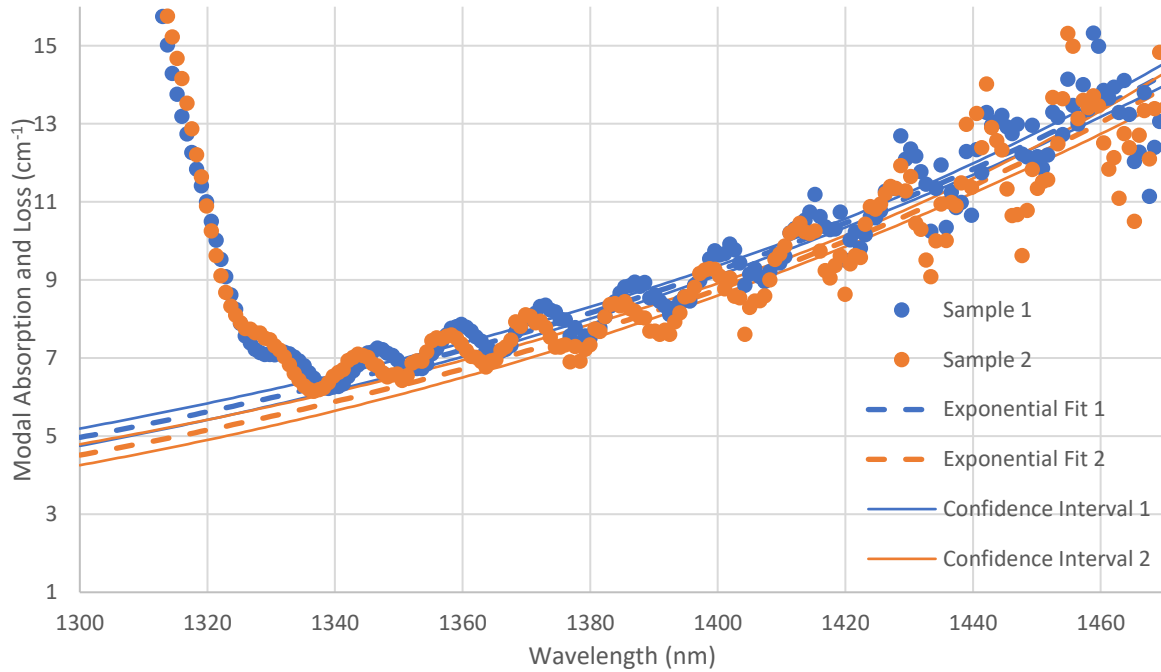
Figure 6.8 Expanded view of modal absorption spectra below the band-edge obtained from two segmented contact narrow waveguide core structures (blue and orange data represent samples 1 and 2 respectively). Exponential fits and confidence values are obtained from data below 1370nm.

Exponential fits to the modal loss below the band-edge appear to have a magnitude offset of approximately 0.2cm^{-1}, the confidence values of which just about overlap throughout the range considered. The optical mode losses at 1303nm for Samples 1 and 2 are (5.06±0.22)cm^{-1} and (4.60±0.26)cm^{-1}. The larger error in confidence values in the narrow core sample is due to the larger deviation from an exponential fit caused by the sinusoidal variation.

The 0.2cm^{-1} offset in the modal loss values suggest uncertainty arising from differences between the two samples measured. A likely cause of this is in the selection of devices where the contact IVs show the best agreement (Section 3.4.4). In previous testing, samples exhibiting large mismatches between their contact IVs (defined as over 3% change in current for a fixed voltage) result in a large increase or decrease throughout the below band-edge modal loss spectrum with respect to well-matched samples. This is due to an effectively higher current density being present in one section than the other which causes a slightly larger or smaller difference in the ASE (throughout all emission wavelengths).

The devices selected for testing in the case of Fig. 6.8 were selected from a set of six segmented contact devices. In the case of wide waveguide core structures this approach was sufficient to achieve excellent agreement between two samples; however in general larger sets of samples may be required to reduce the uncertainty arising from variable device quality.

111

6.4.2 Comparison of Optical Mode Losses
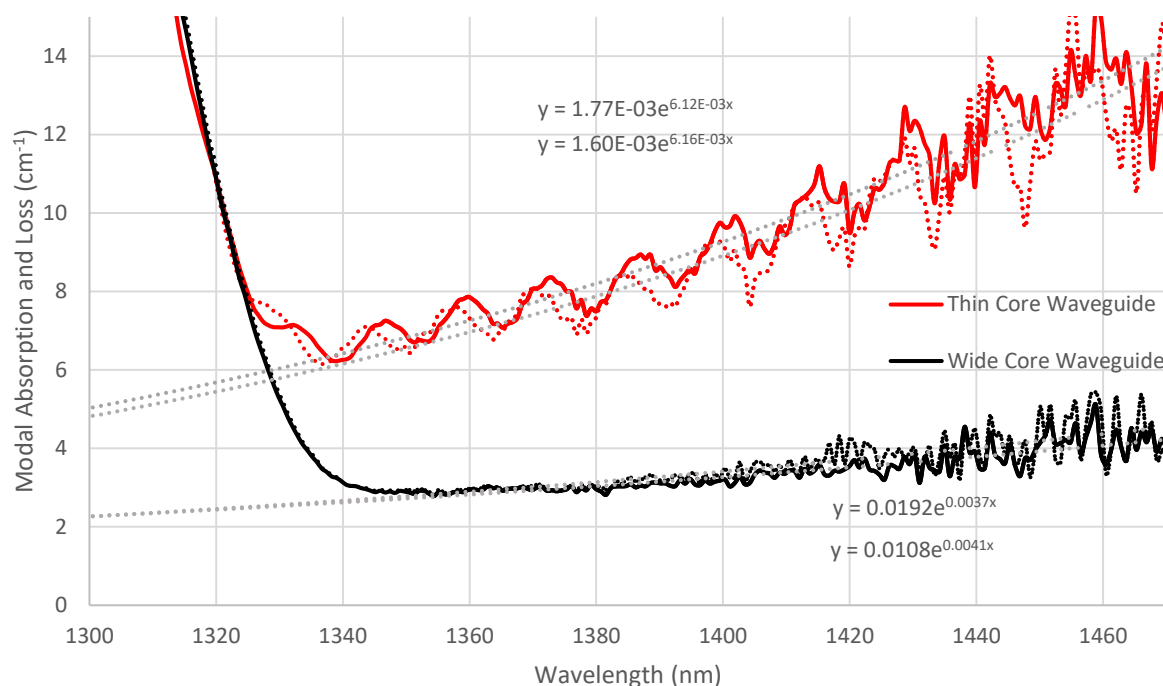
Figure 6.9 Modal absorption spectra obtained for thin core (red) and wide core (black) segmented contact devices. Grey lines indicate the exponential fits to the data, corresponding to inset equations.

Throughout the measurements below the band-edge of the InAs QDs, the narrow waveguide samples exhibit a larger modal loss, consistent with a higher optical mode loss. In both cases, the modal absorption increases non-linearly with increasing wavelength (see also Figs 6.7 and 6.8). There is a much stronger dependence upon wavelength in the narrow waveguide core structures and the corresponding exponent terms in the fitted trend of the narrow waveguide core are much higher than those of the wide waveguide core. This suggests that the observed change in wavelength dependence is not proportional to the net increase in optical mode loss observed.

The higher modal loss of narrow waveguide core structures is consistent with a larger overlap of the optical mode with absorptive layers (i.e. doped cladding). A change in the wavelength dependence could be linked to stronger dispersive effects in the waveguide; the overlap of the optical mode with the absorptive layers increasing with longer wavelengths.

The change in wavelength dependence may also be caused by a change in the dominant mechanism contributing to the optical mode loss. Examples of competing mechanisms are FCA and IVBA explored in Section 2.3.3. The dominant mode loss mechanism will depend upon the overlap of the optical mode with layers of differing dopant type and their respective concentrations.

We will consider the dispersive effects of the waveguide and wavelength dependence of each absorptive layer in our model for the optical mode of these structures (Section 6.5).

6.5 Modelling of Optical Mode Loss due to Doped Semiconductor Layers

To determine the expected contribution to optical mode loss due to mode overlap with doped semiconductor layers, we will solve the primary optical mode of the waveguide structures shown in Figs 6.2 and 6.3 using optical mode solving software Fimmwave (Fimmwave, 2001). Values for the refractive index, FCA, IVBA and their respective wavelength dependences used in Fimmwave will be determined from reported values in the literature (Section 6.5.2) and inference from background theory. We will solve the optical mode across a range of wavelengths to compare with the observed optical mode loss below the band-edge.

6.5.1 Optical Mode Solver

Fimmwave is an optical mode solving software package, capable of calculating possible optical modes in two dimensions of the waveguide and accurately representing a cross section of the waveguide perpendicular to the propagation of light in the structure. In addition to this, it is capable of determining the optical mode given complex values of the material refractive index. The complex refractive indices throughout the waveguide may be determined from either the software's internal library of material properties or, in our case, from user determined values for the real refractive index and absorption values. For automated modelling by the software, the user may also define the material properties as a function of another variable (e.g. wavelength). Note that where the doping of the structure is graded (within the p-type cladding layer), we approximate the graduated doped layer into four layers with decreasing doping concentration.

Fimmwave is capable of solving the mode using a range of mode solver techniques. In this work it will be applying a mode matching method, given complex refractive indices obtained from the user-defined refractive index and absorption values. The resulting primary mode will have an associated effective complex refractive index, the imaginary component of which represents the optical loss of the mode.

As the BA laser devices used are not index guided in the lateral direction, we will simplify the mode solving problem by considering modes in the waveguide for a single vertical slice through the centre of the device (through the contact stripe). All layers of the BA laser are accounted for in the

model except the InAs QDs, which are expected to have a negligible contribution to the optical mode profile. The optical mode will be determined for light whose electric field is in the plane of the layers of the device.

6.5.2 Refractive Index Values for Model

The real components of the refractive indices of the waveguide materials are presented in Table 6.2. As the Fimmwave software allows the material refractive index to be defined as a function of another variable, we have expressed the dispersion relationship as a 2nd order polynomial, fitted to values for the refractive index as a function of wavelength in the range of 1.1-1.5μm from the references given.

Material	A coefficient	B coefficient	C coefficient	Reference
GaAs	0.2857	-0.9481	4.1554	(Skauli et al., 2003)
$Al_{0.2}Ga_{0.8}As$	0.0864	-0.3486	3.6607	(Adachi, 1985)
$Al_{0.4}Ga_{0.6}As$	0.0932	-0.3553	3.5528	(Adachi, 1985)
$In_{0.15}Ga_{0.85}As$	0.689	-2.16	5.11	Sellmeier Equation

Table 6.2 Dispersion relations for refractive index used in optical mode solver of waveguide structures. Apply coefficients to equation as follows: $A\lambda^2 + B\lambda + C$, where λ is expressed in μm.

In the case of GaAs, the real component for refractive index was directly measured in undoped GaAs wafers at room temperature (Skauli et al., 2003). We consider these experimentally derived values to represent the most reliable values of refractive index obtained for this waveguide.

Values for both $Al_xGa_{1-x}As$ alloys were found from a simplified interband-transition model for zincblende material where the composition of Al can be varied (Adachi, 1985). For an Al content of zero however, this model overestimates the values of refractive index given for GaAs. To maintain consistency with the experimentally derived values for GaAs, we correct for this discrepancy by obtaining the *difference* in refractive index between x = 0 and x = 0.2 or 0.4 from Adachi's model and adjust the corresponding values for GaAs from Skauli's measurements.

Refractive index in $In_{0.15}Ga_{0.85}As$ is measured by adjusting the Sellmeier equation for the dispersive relationship of GaAs at wavelengths just below the fundamental band-edge, based on the change of band gap energy from additional Indium content. The values predicted by the Sellmeier equation at x = 0 are in close agreement with those obtained by Skauli, therefore we make no adjustment to those values obtained using the Sellmeier equation.

6.5.3 Absorption Values for Model

From background theory, we expect only FCA to contribute to the absorption below the fundamental band edge in n doped material (Section 2.3.3). Furthermore, our discussion of the Drude model suggests the absorption is wavelength dependent, the trend of which may change with doping concentration. We will consider the experimentally derived values of optical mode loss in these materials.

In (Spitzer and Whelan, 1959), absorption in n-type GaAs were measured with increasing doping levels from the fundamental band-edge up to wavelengths of 20μm. For n-type doping concentrations of 10^{18}cm^{-3} the free carrier absorption is effectively flat, with a value of 5cm^{-1} in the wavelength range we will be considering (1-3μm). Beyond 3μm the absorption increases rapidly, in line with theoretical behaviour for FCA (see Drude model in Section 2.3.3). This flat behaviour in n-doped 10^{18}cm^{-3} GaAs is also observed in (Kozo Osamura and Yotaro, 1972) from the lower limits of the experiment (2.5μm) up to 3μm also, but with a higher absorption of 10cm^{-1}. Osamura goes on to show the flat trend in absorption below 3μm is due to a superposition of the FCA with inter-conduction band absorption (ICBA).

(Spitzer and Whelan, 1959) also shows the absorption due to highly n-doped (5.4x10^{18}cm^{-3}) GaAs. Here the absorption increases from approximately 30cm^{-1}, 38cm^{-1} and 50cm^{-1} for 1, 2 and 3μm respectively. In this case, contribution to absorption from FCA are sufficiently high to cause an increase in absorption with wavelength, despite the additional ICBA in this wavelength range.

As Osamura does not report values for n-type doping higher than 10^{18}cm^{-3} (our model requires doping concentrations as high as 2x10^{18}cm^{-3}) we determine the n-type FCA (and additional ICBA) at the required doping concentrations from a linear interpolation between values observed in the 10^{18}cm^{-3} and 5.4x10^{18}cm^{-3} doped samples reported by Spitzer and Whelan.

Values for the FCA of n-type Al$_x$Ga$_{1-x}$As are not widely reported. If we assume the FCA gives the greatest contribution to the absorption, we may adjust the absorption values found in GaAs using the Drude model (Section 2.3.3) to give their equivalent values in Al$_x$Ga$_{1-x}$As:

$$\overline{\quad\quad\quad}\ \overline{\quad}$$

Equation 6.1

We note the dependence of this absorption upon the carrier's effective mass,   , and refractive index,   . There is also likely to be a change in the scattering rate,   , however this value is not easily found for $Al_xGa_{1-x}As$. We may modify the FCA in the $Al_{0.2}Ga_{0.8}As$ and $Al_{0.4}Ga_{0.6}As$ by considering the change in the ⸺ between these and GaAs. This results in a small reduction to the FCA in these layers.   is found from the dispersion relations in Table 6.2, while   for GaAs, $Al_{0.2}Ga_{0.8}As$ and $Al_{0.4}Ga_{0.6}As$ are found from values given by (Levinstein, 1996) as 0.063, 0.0796 and 0.0962 respectively.

The absorption in p-type ($2.1\times10^{18}cm^{-3}$) GaAs found by (Henry et al., 1983) will account for both FCA due to p-type dopants and IVBA. Henry notes that the absorption should be proportional to the doping concentration, which we will assume in our modelled values. For the sample measured, the absorption is shown to double in the range from 1.3-1.6µm ($27.3cm^{-1}$ to $54.6cm^{-1}$). We will approximate this wavelength dependence with a linear fit.

To infer the corresponding values in $Al_xGa_{1-x}As$, we note the values observed in the far infrared values (10µm-400µm) in (Rinzan et al., 2005). Across this range, p-type $Al_{0.01}Ga_{0.99}As$ and $Al_{0.2}Ga_{0.8}As$ show very similar absorption. We also observe in (Henry et al., 1983), for a range of different III-V compounds (InP, GaAs and $In_{0.53}Ga_{0.47}As$), the values of intervalence band absorption were similar within the 1.3-1.6µm wavelength range (12-14cm^{-1} at 1.3µm and 24-26cm^{-1} at 1.6µm). Significant variations in IVBA are only observed at much longer wavelengths. For these reasons, we approximate the IVBA of $Al_xGa_{1-x}As$ to that of GaAs as observed by Henry.

Material	Dopant Type	Doping Concentration (cm^{-3})	E	F	G	Reference
GaAs	n	2e18	0	3	5.4	(Spitzer and Whelan, 1959)
GaAs	n	2.4e18	0	3.78	6.44	(Spitzer and Whelan, 1959)
$Al_{0.4}Ga_{0.6}As$	n	2e18	0.567	1.3677	6.3835	Drude Model
$Al_{0.2}Ga_{0.8}As$	n	2.4e18	0.3681	0.9506	4.5235	Drude Model
GaAs	p	1e19	0	433.33	-433.33	(Henry et al., 1983)
$Al_{0.2}Ga_{0.8}As$	p	2e17	0	8.666	-8.666	(Henry et al., 1983),(Rinzan et al., 2005)
$Al_{0.4}Ga_{0.6}As$	p	2e17	0	8.666	-8.666	(Henry et al., 1983),(Rinzan et al., 2005)

Table 6.3 Absorptions relations for use in optical mode solver of waveguide structures. Apply coefficients to equation as follows: $E\lambda^2+F\lambda + G$, where λ is expressed in µm.

Gold top and bottom contacts of the device define the boundary conditions of the mode matching solver as perfect conductors.

6.5.4 Modelled Modal Absorption

The refractive index and absorption values throughout the waveguide have been found with reference to the literature (Tables 6.2 and 6.3), and are used with Fimmwave's mode matching solver to determine the modal absorption values (found from the imaginary effective refractive index) for a range of wavelengths (1300nm-1420nm). For wavelengths above the band-edge of the InAs QDs, the modelled values should closely match the optical mode loss, accounting for the FCA, ICBA and IVBA of the doped layers.

The modelled optical mode losses for the wide and narrow waveguide core samples are presented in Fig 6.10. Resonant peaks are observed in the modelled values of the thin waveguide core only, with periodicity of approximately 80nm. This periodicity derives from a resonance of the optical mode with the n-type device substrate. This is made possible by the weaker guiding of the optical mode beyond the cladding layers.

We do not expect the phase of this resonance to be reflected in the experiment data, as the substrate dimension (approximately 100μm) is not known with sufficient precision to predict this.
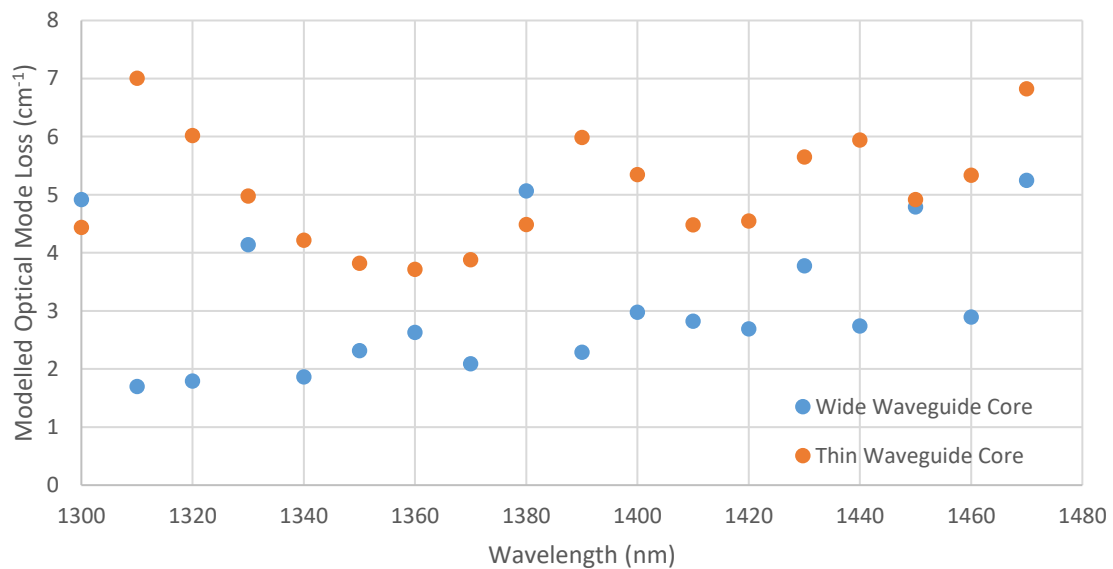
Figure 6.10 Modelled optical mode loss for thin (orange) and wide (blue) waveguide core samples

Across the range of wavelengths modelled, we observe a net increase in the modelled optical mode loss values with wavelength. This is due to the greater overlap of the optical mode with the doped cladding layers. In both cases an increasing value of optical mode loss with wavelength is anticipated. Fig. 6.11 demonstrates the larger overlap of the optical mode with the cladding layers with increasing wavelength which would account for this. We will consider the modelled data further with respect to the experimental values (Section 6.5.5).
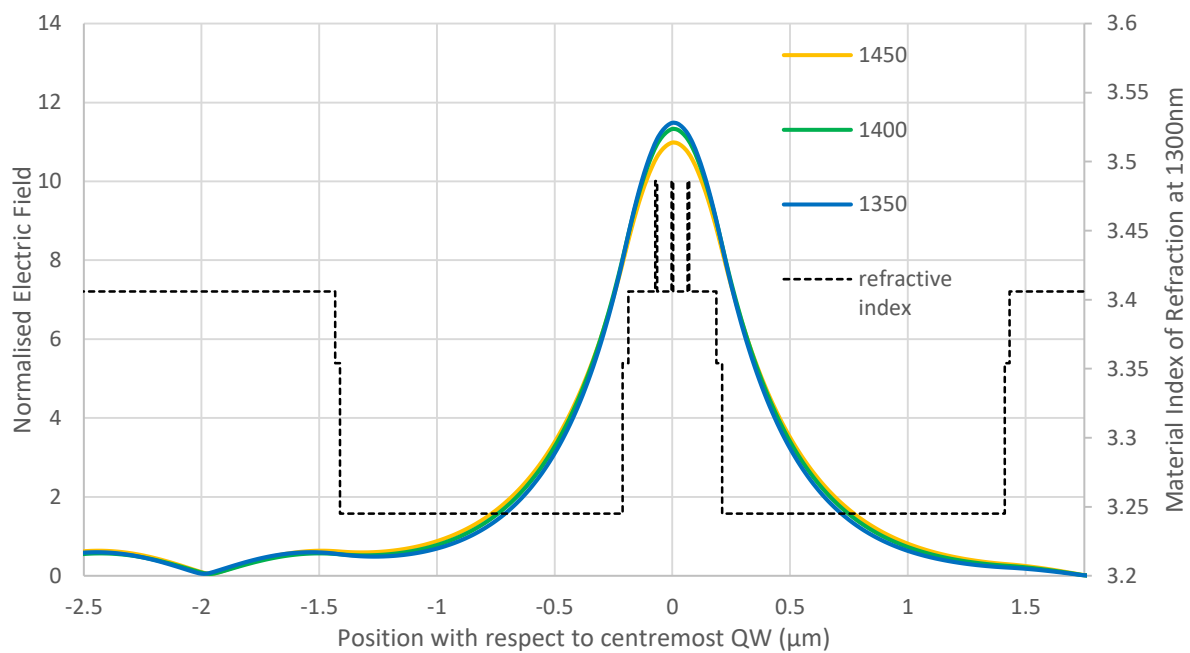
Figure 6.11 Modelled optical mode in wide waveguide core samples for thee different wavelengths. n-type device substrate extends below -2.5μm.

6.5.5 Comparison of Modelled and Measured Optical Mode Loss

Modelled optical loss values for the wide waveguide core (Fig. 6.12) generally underestimate the experimental optical loss by 0.5-1cm^{-1}. This is a reasonable result, as the model does not take account of sources of optical loss beyond below band-gap absorption mechanisms. For example, Rayleigh scattering of light due to small crystal irregularities arising from interface roughness may account for additional loss of light from the cavity.

A number of modelled values of modal absorption and loss give significantly high values of optical loss than the mean. We will assume these are a consequence of the mode solver software being run with insufficiently high resolution in order to determine optical modes which were confined to the core of the waveguide. This is likely, as in order to account for potential substrate modes of the structure a combination of both relatively large features (the substrate was modelled as 100μm) and small features (80Å wide InGaAs QWs). This would result in solutions which were less well optimised for the detailed core structures. We will assume these large outliers result from the poor resolved

solutions, and the resulting trendline given in Fig. 6.12 ignores the four largest values of modelled absorption.
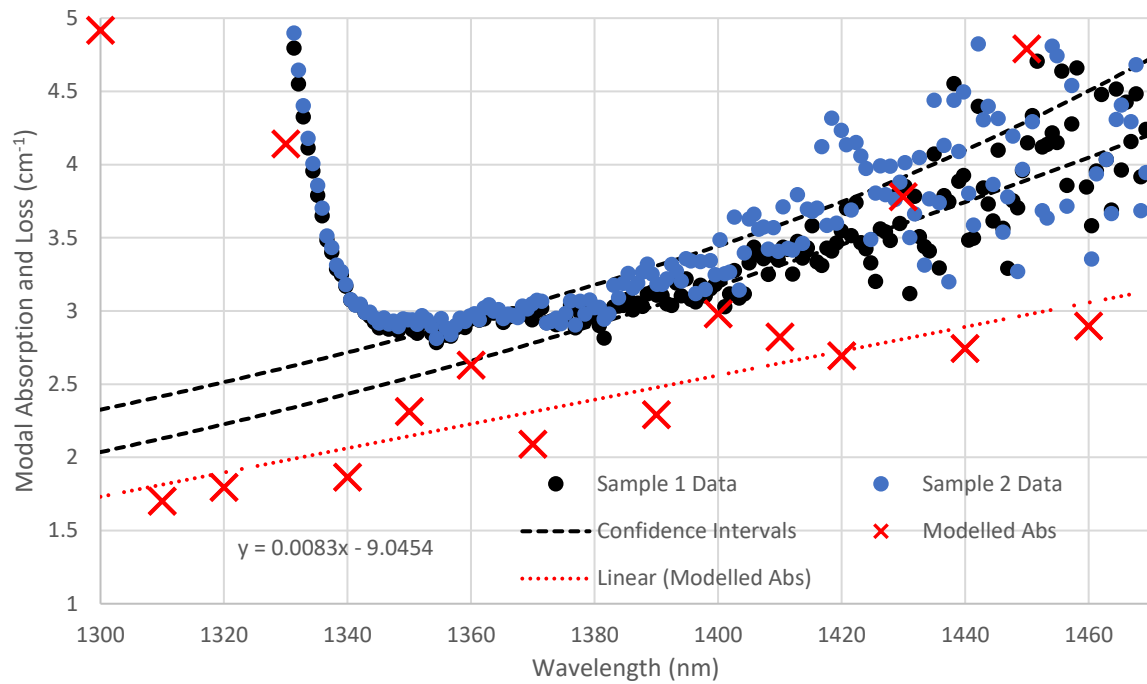
Figure 6.12 Modelled absorption (red crosses) for wide waveguide core samples plotted against experiment values. Confidence intervals from exponential fits are included

The trend in modelled absorption values is slightly shallower than that observed by the experimental data. Small differences in predicted wavelength dependence of this trend are to be expected, given relatively little reporting of the wavelength dependence of the materials and the assumptions this led to in the model. Given this, the wavelength dependence observed in the experimental data is largely consistent with a combination of wavelength dispersion by the waveguide and increasing FCA and IVBA with wavelength in doped semiconductor materials. We will consider the agreement of modelled and experimental values of optical mode loss in this sample further in Section 6.6.
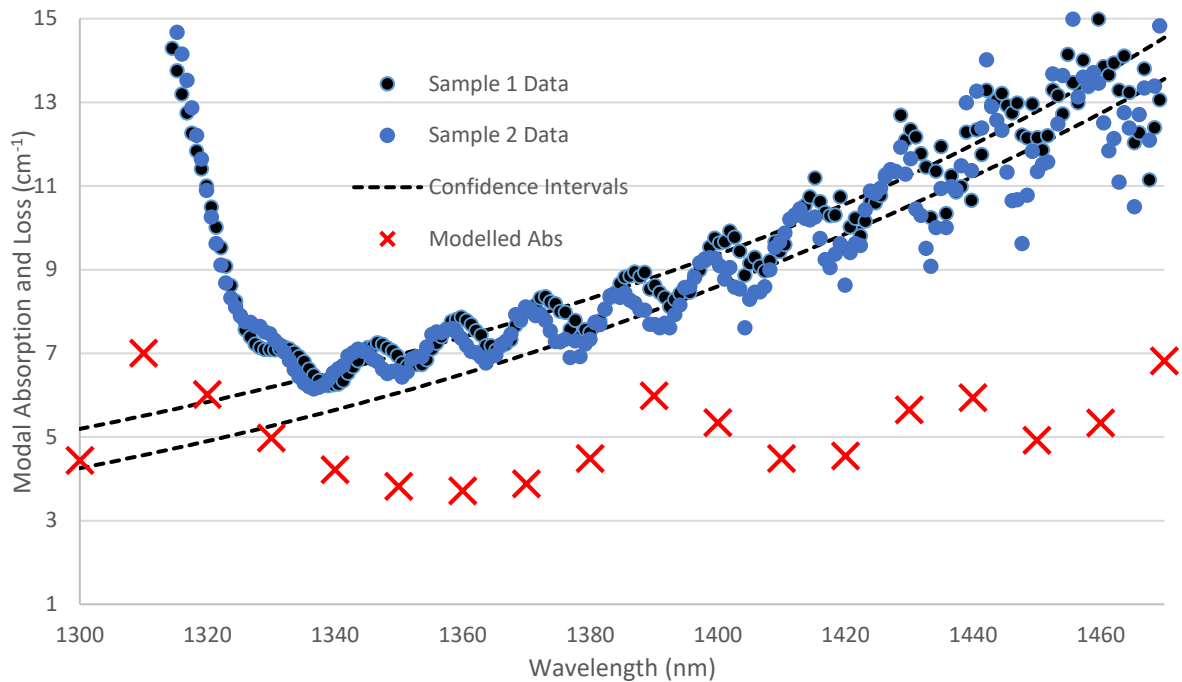
Figure 6.13 Modelled absorption (red crosses) for narrow waveguide core samples plotted against experiment values. Confidence intervals from exponential fits are included

Modelled modal loss of the thin core waveguide samples also underestimates the experimental values, as well as the trend observed (Fig. 6.13). While the modelled wavelength dependence is steeper in the thin core waveguide structures (with respect to the lowest values of optical loss measured), it greatly underestimates the true observable trend. This underestimation appears to go beyond inadequacies in the modelling of optical loss due to doped semiconductors. It is likely that in this model, a significant mechanism of loss present in thin core devices has not been accounted for. I believe it is reasonable to assume the cause of this discrepancy is linked to the introduction of sinusoidal variation in absorption, and shall explore phenomena which could account for both (e.g. resonances with structural features and bend losses).

The sinusoidal variation in absorption with wavelength is present in the modelled values of loss, however the periodicity of this feature is much longer than that of the experimental data (Fig. 6.14(a)). The peak absorptions of modelled data are a result of greater coupling of the optical mode to the substrate of the structure, and are much more present in this device due to how weakly guided the mode is by the thin waveguide core. However, given the mismatch in periodicity, it is unlikely that the modelled substrate resonances of the device could account for the sinusoidal trend observed in the experimental data.
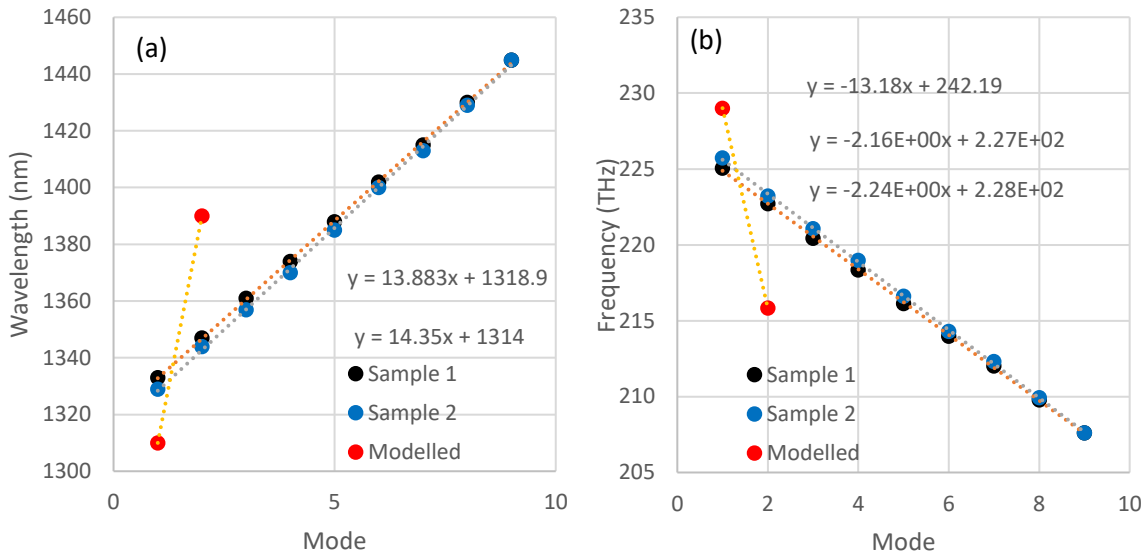
Figure 6.14 Peak wavelengths (a) and frequencies (b) in modal absorption and loss oscillations of thin core waveguides

The frequency separation of peak absorption by the two thin waveguide core samples further supports that this sinusoidal behaviour is not related to resonances with the substrate. Were this the case, then the frequency separation, , and substrate height, , could be related by the simple equation for longitudinal modes:

$$\overline{}$$

Equation 6.2

where is the speed of light and the refractive index of the cavity medium. we will approximate to 3.3 given the device structure is predominantly GaAs and as 2.20THz from the average separation of modes observed in Fig. 6.14(b). This would indicate resonant cavity features of the order of 20µm, which do not reflect the dimensions of the substrate, waveguide core nor waveguide cladding separation.

Investigation of oscillation features within the literature suggests strong parallels exist with the oscillatory trends in absorption observed as a result of bend losses in cylindrical optical fibres. This phenomenon was originally described by (Harris and Castle, 1986) as an oscillatory behaviour arising from the presence of whispering gallery modes in the cladding of optical fibres which are present due to the combination of bend losses and weak guiding of light by the core. These whispering gallery modes then contribute to maxima and minima in the output signal where the whispering gallery modes couple and anti-couple with the fundamental mode of the core.

The similarities of this bend loss behaviour, reported on in great detail in (Tangonan, 1988), to that of our thin core waveguide samples are striking. The periodicities are of a similar order, with peak spacing from 20-40nm observed (varying with radius of curvature) in the wavelength range of 1300-1600nm. The form of these oscillations is that of a smooth sinewave whose amplitude increases with longer wavelengths. Tangonan explains this increase in amplitude is due to a decrease in the phase mismatch of the whispering gallery modes and fundamental mode with increasing wavelength.

The presence of bending in semiconductor laser devices is entirely possible. In the GaAs substrate structures investigated this arises from the small lattice mismatch of $Al_xGa_{1-x}As$ ternaries in the cladding with the GaAs substrate. Over-thinning of the substrate can lead to observable curvatures in the structure. The devices studied are thinned to no more than 100μm with this consideration in mind, however curvature radii which may result in observable bend losses need not be large with respect to beyond what is easily observable under a microscope (note that bend losses are observed for curvature radii from 5-100mm in (Harris and Castle, 1986) and 21.5mm in (Faustini and Martini, 1997). As such, the lack of readily observable curvature in 2mm long segmented contact devices is entirely possible while still incurring bend losses.

The weaker guiding of light by the thinner waveguide core samples is also a key enabling factor in this form of oscillatory behaviour (Harris and Castle, 1986), accounting for its absence in wide waveguide core samples. The stronger wavelength dependence beyond the model of optical loss presented is also consistent with the stronger wavelength dependence that bend losses introduce. Further investigation into the wavelength dependence of optical mode loss should consider bend losses as a potential contributor. This could be supported by precise measurement of device curvature. We will investigate these oscillations further with respect to changing device temperature in Section 6.6.4.

6.6   Temperature Dependence of Modal Absorption and Loss

Understanding of the temperature dependence of optical mode loss may be crucial in the management of laser temperatures for achieving peak efficiency. It may also be useful in precisely characterising the optical mode loss of lasers in conditions outside that explored by the SCM (note these devices are usually tested at room temperature with low duty cycles to prevent self-heating). Variations in the optical mode loss with respect to temperature have not been directly measured in lasers emitting at 1.3μm. The precisions to which optical mode loss may be found by the modulated approach to the SCM will allow us to confirm whether temperature dependence of optical mode loss

could have a significant impact upon the performance of high power laser diodes (i.e. >1cm^{-1} variation from its value at room temperature.

Investigations into IVBA temperature dependence in (Henry, 1983) suggest that IVBA may cause poorer device performance (e.g. higher threshold current density and poorer slope efficiencies) with increasing temperature. In particular, the characteristic temperature of IVBA absorption fitted to the temperature dependence of GaAs suggests it has low characteristic temperature,   , of 180K at 1.3µm and 340K at 1.6µm. GaAs IVBA coefficient at 1.3µm would be expected to vary from 13cm^{-1} at 300K to approximately 16cm^{-1} at 370K (roughly 20% increase in loss). As such, we may reasonably expect that, where IVBA makes a significant contribution to the optical mode loss of the wide or thin waveguide core samples, even small increases in optical mode loss at wavelengths tending to 1.3µm might be observable.

We will also use this experiment to interrogate the behaviour of the oscillations in modal absorption and loss observed in thin waveguide core samples further.

6.6.1 Methodology

The temperature dependence of optical mode loss in both the wide and narrow waveguide core samples was explored for a range of temperatures above room temperature. The experimental conditions under which this was achieved were as discussed for previous measurements of these samples in Section 6.4, except with shorter integration times (200s) and also with devices tested while enclosed in a vacuumed cryostat. This vacuum (reduced to pressures of approximately 1.69x10^{-3}mbar utilising the backing pump of a turbomolecular pump system) was necessary to reduce the thermal conductivity between the device and external environment and so help improve the stability of elevated temperatures. This was crucial for reducing the systematic drift caused by changes in optical power of the device with time varying temperatures which may occur as a result of the active management of device temperature (Section 3.5).

The temperature of devices was increased using a heater within the cryostat and allowed to maintain the desired temperature for approximately five minutes between each measurement of temperature. This allowed temperatures throughout the cryostat to equalise before measurement, with the intention of reducing systematic drift in the measurement as well as ensuring the true device temperature was in good agreement with that measured by the thermocouple of the cryostat.

The position of the device nearfield was observed to drift with changing temperature of the detector, an effect which was reversible with decreasing temperature. Further tightening of the screws of the mounting plate which secured the device within the cryostat greatly reduced this effect, however small drifts in the lateral direction were still observed. We concluded that this drift was due to thermal expansion of components of the device mount. Therefore it was necessary to make small translational corrections to the position of the translation stage between temperature trials. In this approach we assume changes to the rotational alignment of the device have a negligible impact upon the measurement.

Increasing temperatures between room temperature and 370K were measured, representing a temperature range which from previous work in our group was known to be non-destructive. Temperatures were also sampled decreasing from 370K to test the repeatability of the measurement with respect to thermocouple temperature.

For the purposes of comparing the observed shift in band-edge energy with that predicted by the Varshni equation, in this section we will generally express the modal absorption and loss with respect to photon energy. We consider the relationships between the entire modal absorption and loss spectra first before discussing the optical mode loss.

6.6.2 Band-Edge Shift with Device Temperature
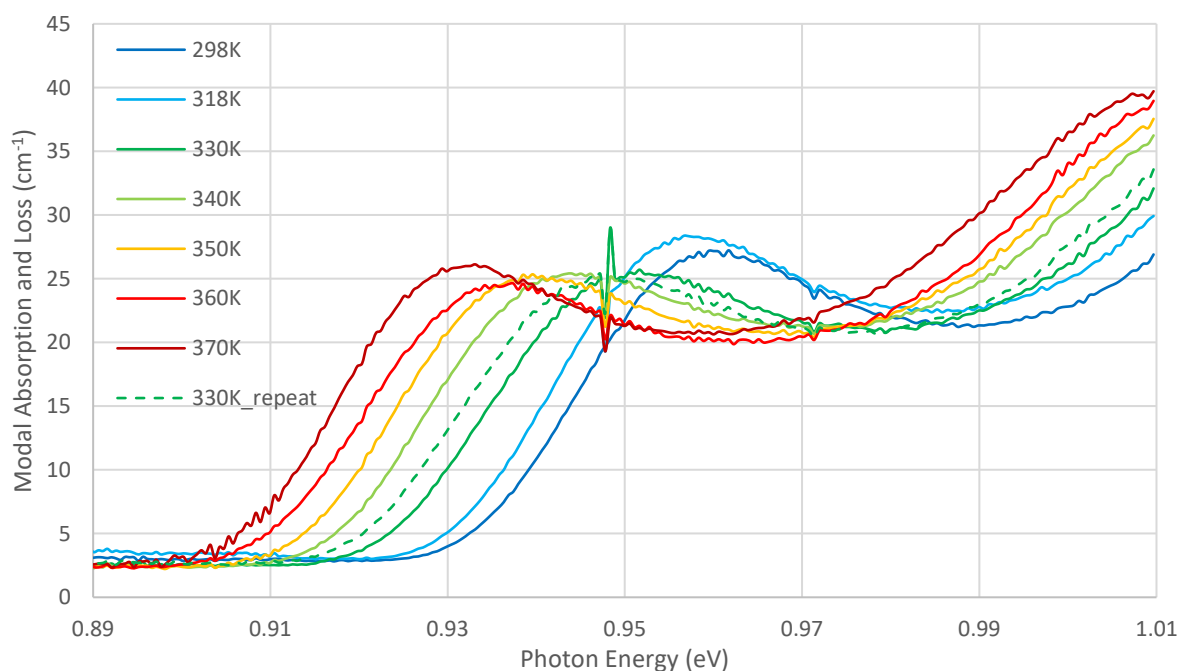
Figure 6.15 Temperature dependence of the modal absorption and loss spectra of wide waveguide core sample
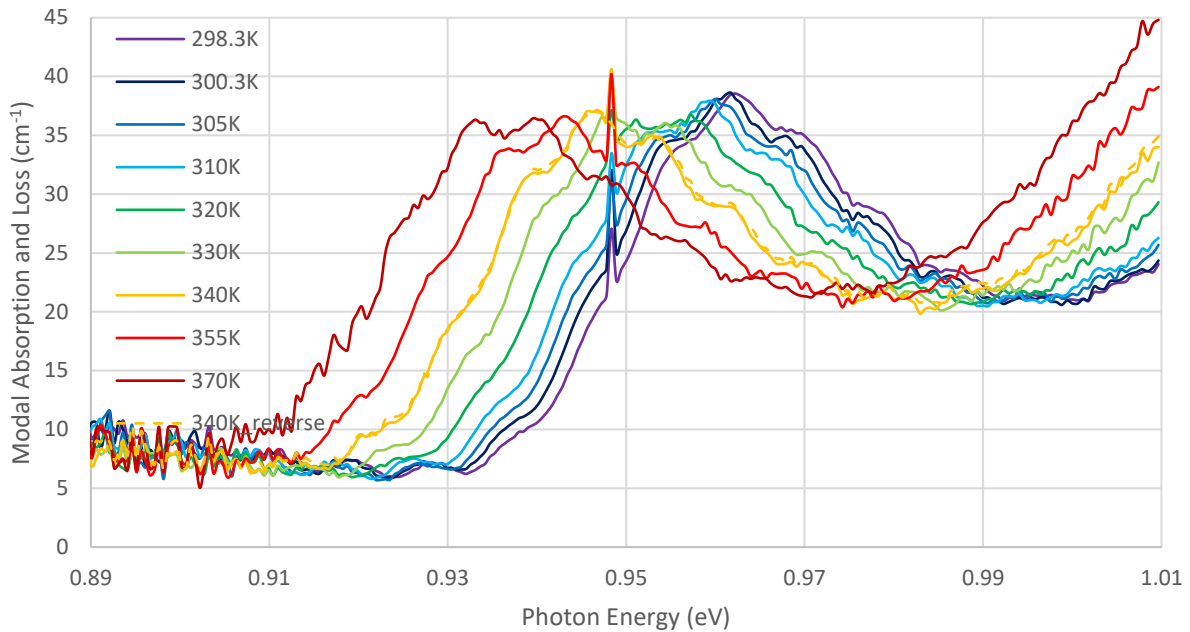
Figure 6.16 Temperature dependence of the modal absorption and loss spectra of thin waveguide core sample

In both samples, the band-edge of the ground state absorption of the InAs QD material becomes red shifted, due to the band gap narrowing of this material with increasing temperature. In wide waveguide core samples, the peak absorption of the InAs QD ground state varies without a clear trend between temperature trials, with most temperatures agreeing at a peak absorption of approximately 25cm^{-1}. In the case of the thin waveguide core sample, this variation occurs only near room temperature, and later tends to a value of approximately 36.5cm^{-1}.

A potential cause of this variation in peak absorption is drift in device temperature during measurement. This would not only introduce a systematic drift in the intensity of light, but also in the true modal absorption and loss of the device. To test for this, we consider time variations in the modal absorption and loss spectra obtainable from ASE collected at different points during the measurement. This is possible as the modulated method allows time varying values of modal absorption and loss to be ascertained. We compare modulated data obtained from the first, second, third and fourth quarters of the time frames used to acquire ASE in Fig. 6.15. We do this for those spectra obtained for wide waveguide core samples which appeared most anomalous.
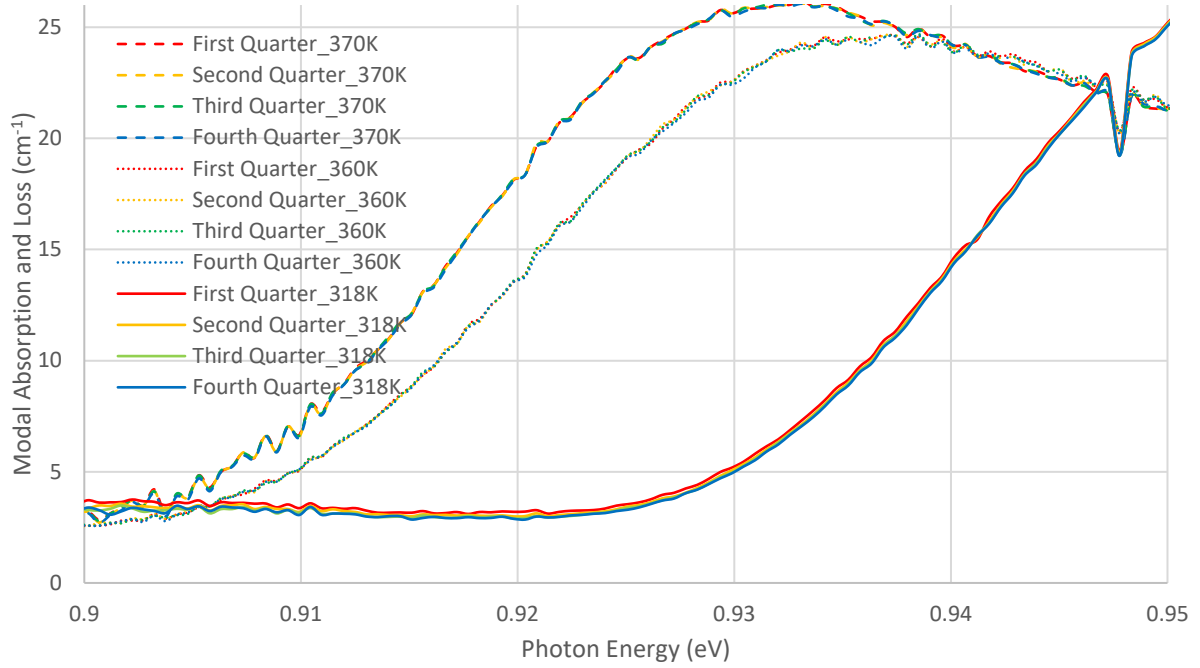
Figure 6.17 Variation in potentially anomalous modal absorption and loss spectra of wide waveguide core samples with respect to time (approximately 50s elapse between each quarter)
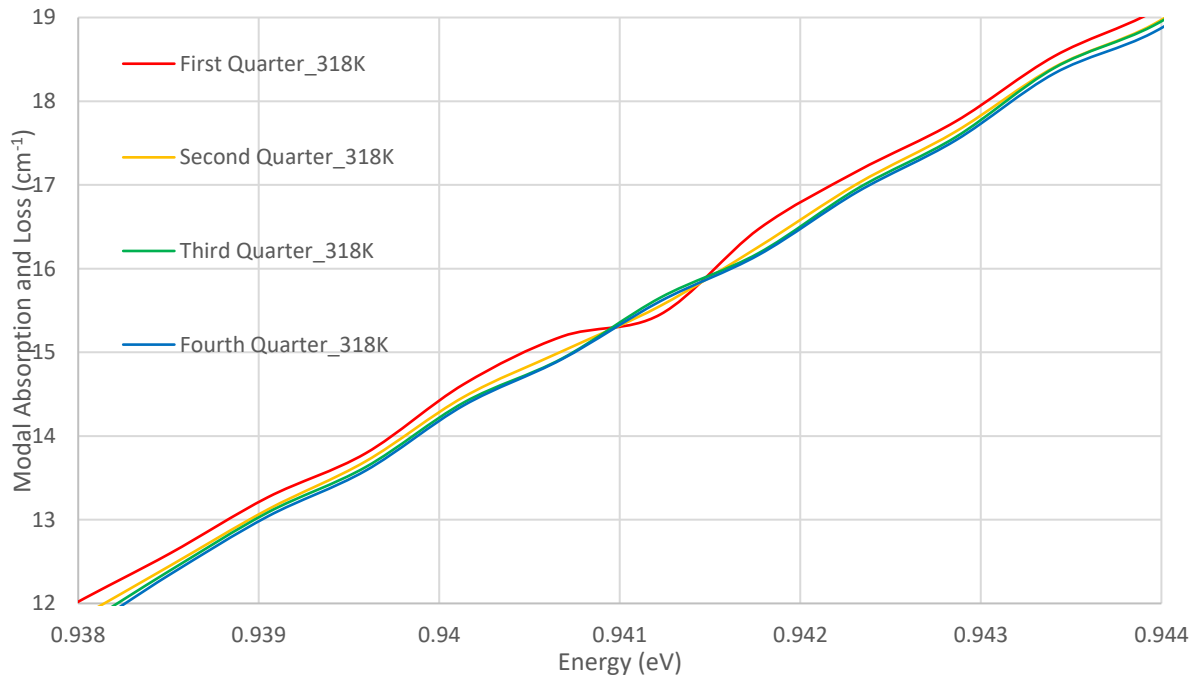
Figure 6.18 Variation in modal absorption and loss spectra obtained at 318K for wide waveguide core sample

Time dependent plots of spectra in Fig. 6.17 suggests that large variations in the band-edge and the absorption peak (of similar order as are seen between trials) are not present. Nor do we see large variations in the peak modal absorption of these spectra. We conclude that the variations in

peak modal absorption of wide waveguide core samples could be due to misalignments of the sample arising from thermal expansion.

In Fig 6.18, the largest shift in band-edge energy of the temperature trials observed is seen in the 318K measurements, with a shift of 0.26meV mesured with respect to absorption lying at the FWHM of the peak absorption. The Varshni equation (Varshni, 1967) may be applied to determine the equivalent change in temperature which would account for this shift due to band gap narrowing:

$$\rule{3cm}{0.4pt}$$

Equation 6.3

where   and   are constants found empirically for the material in question. Values of these coefficients in InAs are given by (Vurgaftman, Meyer and Ram-Mohan, 2001) as

and   . We consider the shift in energy gap which this would incur with respect to the spectrum measured at room temperature only, and may disregard the energy gap predicted by Eq. 6.3 (note that the quantum confinement of dots would cause a larger energy difference than this value). Consequently the observed 0.26meV shift in the band-edge is roughly equal to a 1.0K change in the measurement of modal absorption and loss at 318K, and suggests that temperatures given by the cryostat thermocouple are true to within 1K.
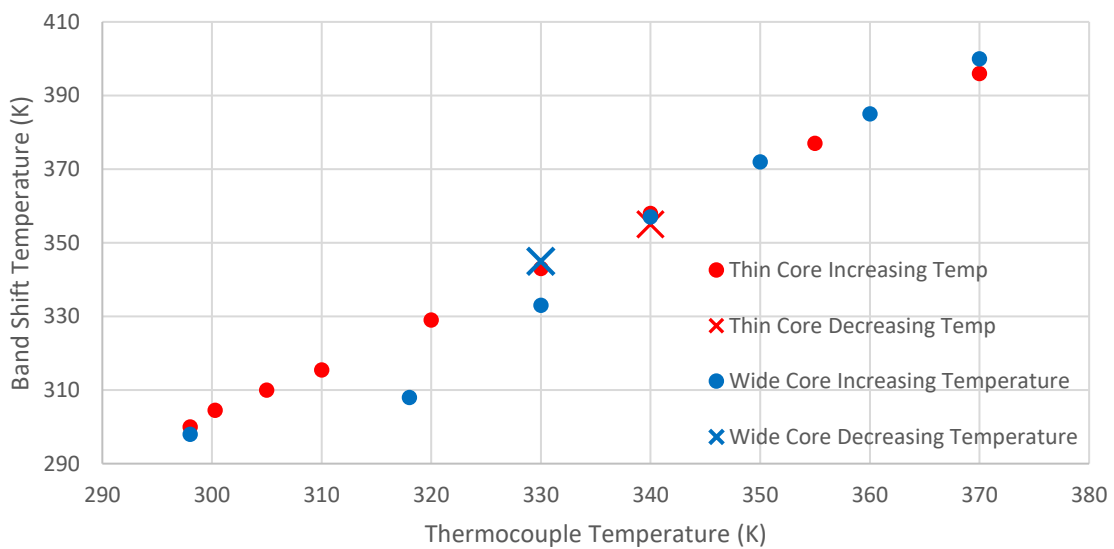
Figure 6.19 Temperature of cryostat as determined by thermocouple and the required temperature required for Varshni equation as applied to InAs material to account for shifts in the band-edge at FWHM of peak modal absorptions

In Fig. 6.19, we extend the use of the Varshni equation to consider if the temperature change as measured by the cryostat thermocouple are consistent with the temperature change suggested by

the observed shifts in band-edge, as measured at the FWHM of absorption peaks. Low thermocouple values for wide core samples appear to deviate from the trend established by the rest of the data. This deviation is rectified in the reverse temperture measurement at 330K, suggesting this deviation was an isolated inaccuracy in the temperature determined by the thermocouple.

In general, there is very good agreement in the Varshni band shifts given by the wide and thin waveguide core samples with respect to the thermocouple temperture. The overall underestimate of the band-shift energy from the thermocouple temperatures is not unexpected, as the Varshni equation is a measure of the band-gap narrowing of *bulk* material. The quantum confinement of InAs QDs means that the band-shift will be dependent both on the band-gap narrowing of the QD material, but also of the ajoining wetting layer (InGaAs QW). The discepancy may also be due to significant miscalibration of the thermocouple. A comparison of the observed band-edge shift with what would be expected due to band-gap narrowing of InAs QDs and adjoining materials would resolve this discrepancy, however such analysis is beyond the scope of this thesis. We do note however that the band-edge shift of the two samples investigated is very well matched. This suggests that the composition of dots and adjoining materials are very similar, confirming the supposition that these samples differ only with respect to waveguide core thickness.

6.6.3 Temperature Dependence of Oscillations in Modal Absorption and Loss of Narrow Waveguide Core Samples
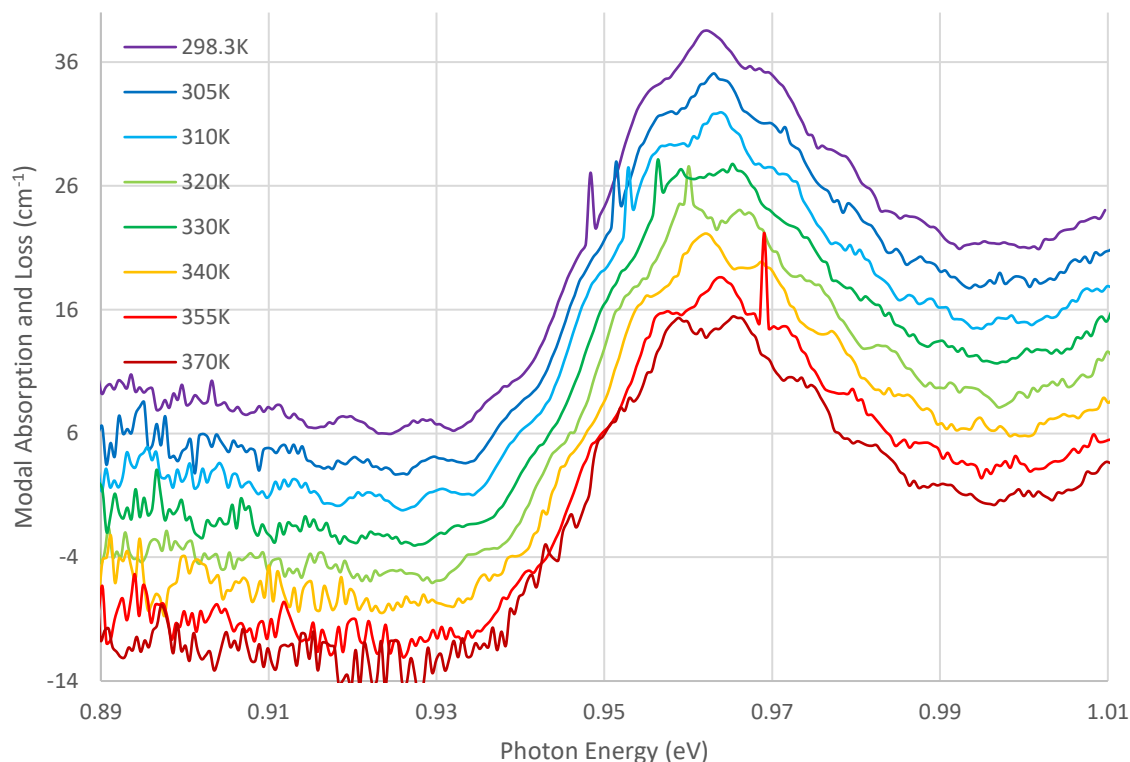
Figure 6.20 Modal absorption and loss spectra of thin waveguide core samples shifted by photon energies described by the Fig. 6.19 for the alignment of the FWHM of peak absorption. For comparison, successive spectra are offset by -3cm^{-1}.

We have proposed the oscillating feature of the modal absorption and loss of thin waveguides is related to bend losses of the structure. In Fig. 6.16, the phase of this oscillation appears to change between measurements of temperature, sometimes with the appearance of maintaining its position with respect to the peak absorption.

This is investigated further in Fig. 6.20 by shifting the spectra by those values described by the band-edge shift in Fig. 6.19. The phase of initial low temperature readings (298.3-310K) are closely matched under this transformation, however the spectra as a whole would suggest that this phase is not related to temperature dependent band-edge shift. A more in-depth study would be required to definitively state whether the phase of oscillations is related to or independent of band-edge shift, however given I will later show the oscillation frequency also varies with temperature (Fig. 6.21), this approach may be ultimately pointless. I would expect that were the root cause of the oscillations purely due to bend loss, that the phase of oscillations would be independent of the temperature

induced band-edge shift. However, changes in device temperature will inevitably generate strain and so a change in device bending, leading to a change in the oscillation seen. The dependence of phase of oscillations upon band-edge would be best interrogated by instead inducing a band-edge shift by reverse biasing the device's unpumped section.

We perform the same analysis of periodicity in wavelength of the modal absorption peaks as was used in Fig. 6.14. This used a range of wavelengths strictly within 1268-1321nm for each temperature reading, as these were well resolved in most spectra obtained. We omit the 320K reading here the oscillations were much shallower than those observed for other temperatures.
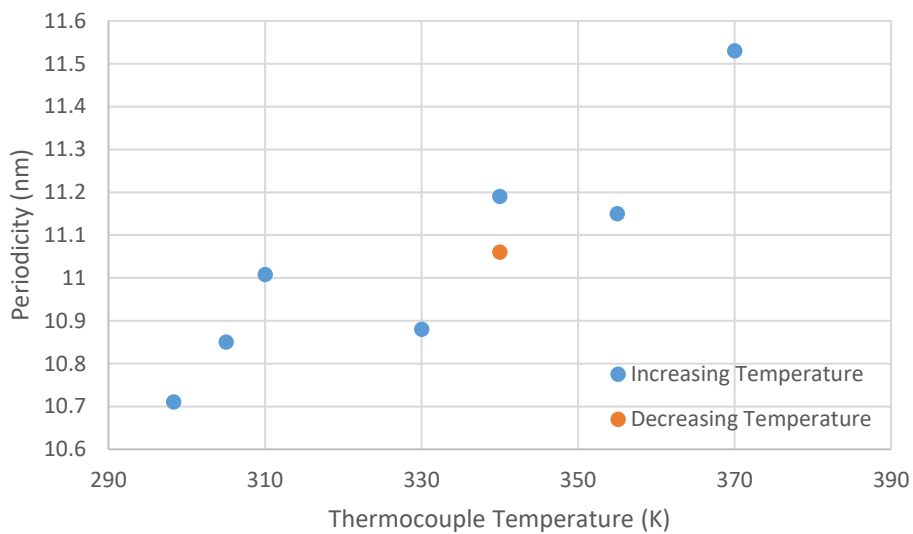
Figure 6.21 Periodicity of peak modal absorption in oscillations in thin core waveguides obtained for wavelengths between 1268-1271nm

We observe reasonable correlation between increasing device temperature and increasing period of the oscillations which is reversible with temperature. This increase accounts for the mismatch of phase of oscillations observed across different temperatures in Fig. 6.16.

Where bowing of the substrate is due to the mismatch of lattice constants of $Al_xGa_{1-x}As$ cladding with GaAs, then temperature dependence of this bowing can account for changes in the bend losses. Notably (Tangonan, 1988) observes an increase in the peak spacing of bend loss oscillations with increasing radius of curvature of optical fibres. The lattice mismatch of AlAs (and therefore $Al_xGa_{1-x}As$ claddings) with respect to GaAs is seen to decrease with increasing temperatures up to a limit of 900°C in (Ettenberg and Paff, 1970). As such a decrease in the radius of curvature of this substrate bowing with increasing temperature may be expected, with an increase in peak spacing which is consistent with bend losses.

The peak spacing of oscillations observed at modal absorption values in Fig. 6.21 (approximately 11nm) is noticeably shorter than those observed at the longer wavelengths of modal loss in Fig. 6.14 (approximately 14nm). This is consistent with increasing peak spacing with wavelength observable in data presented by (Tangonan, 1988) and more recently (Faustini and Martini, 1997).

6.6.4 Temperature Dependence of Optical Mode Loss
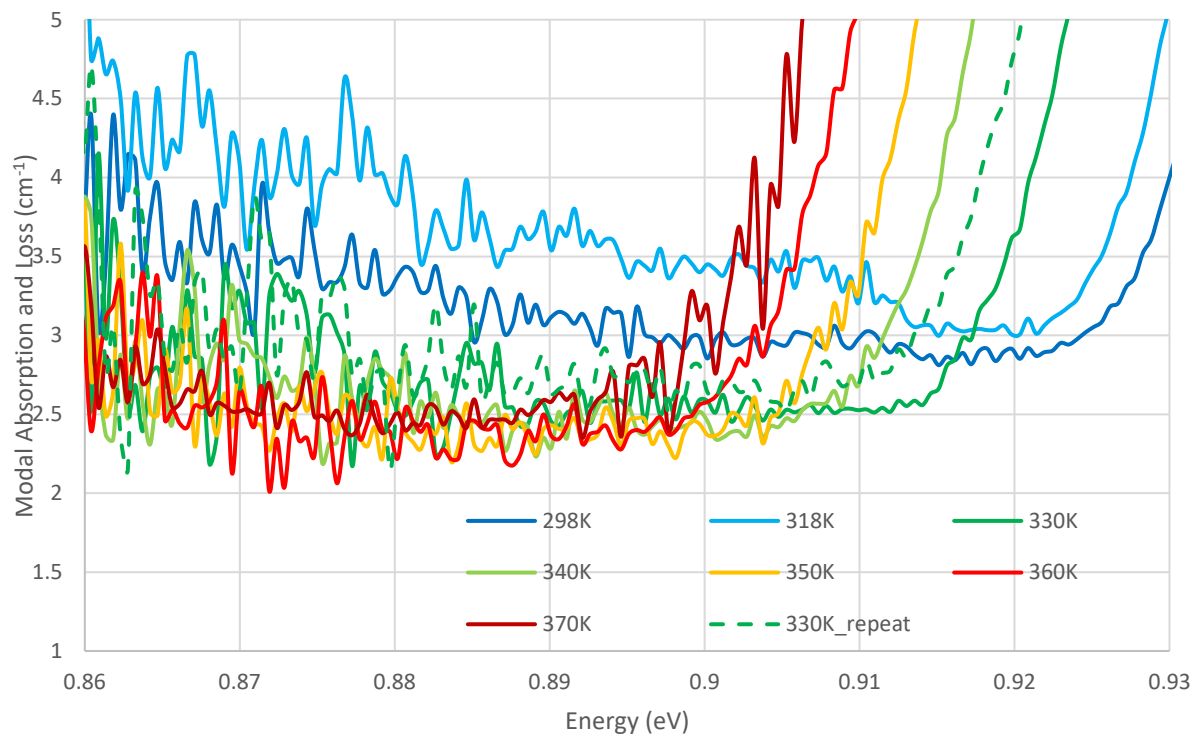
Figure 6.22 Below band-edge optical mode loss with increasing device temperature for wide waveguide core sample

Unexpectedly, there are significant variations in the trend between optical mode loss and wavelength and its overall value in initial increases in temperature (see spectra 318K). This reading also exhibited large discrepancies with respect to the peak modal absorption values and expected band edge shift. Consequently we believe this spectra results from an experimental inaccuracy (e.g. misalignment of sample).

An initial decrease in optical mode losses measured below the band edge mirrors the change in peak modal absorption observed in Fig. 6.15. A reduction in optical mode loss with increasing temperature is unexpected, and cannot be accounted for by losses incurred due to FCA and IVBA. This behaviour was repeatable, suggesting it is not the result of random errors in the experiment.

131
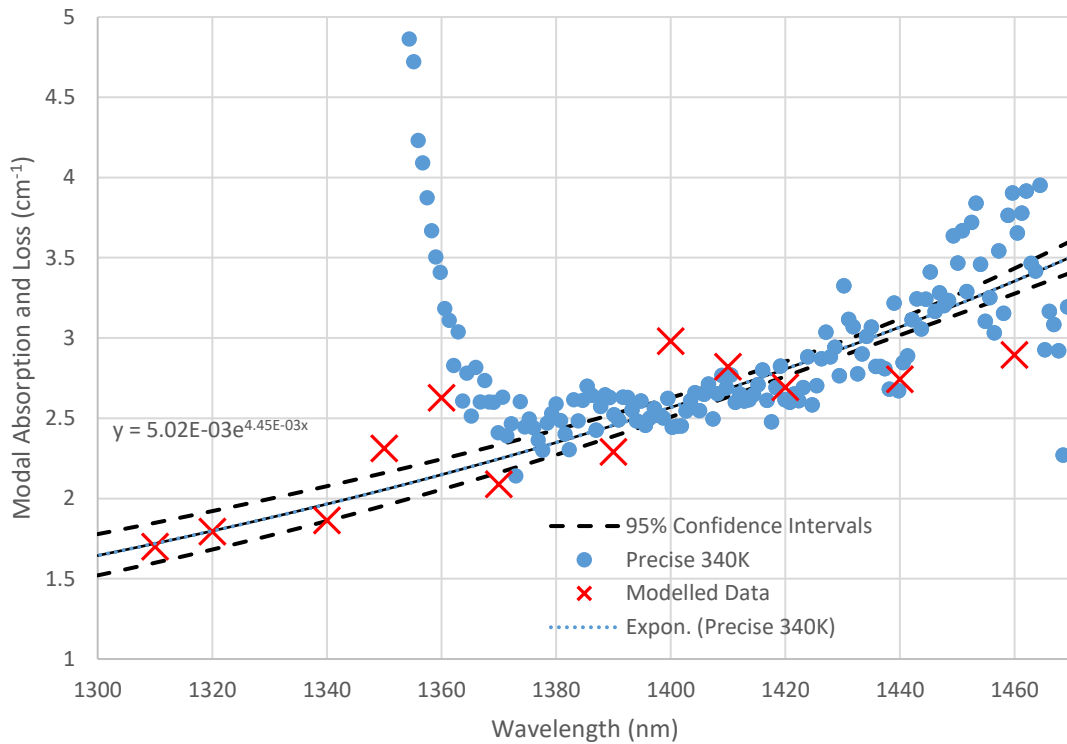
Figure 6.23 Comparison of modal absorption and loss of device at 340K (measured over 500s integration time) with modelled room temperature optical mode loss values

Notably, the modelled values of optical mode loss are in good agreement with the experimental data at raised temperatures (precisely measured optical mode loss of 340K shown in Fig. 6.23). This indicates that the initial discrepancy in modelled and experimental data of wide waveguide samples could be due to failings in the experiment which are resolved with higher temperatures. If this is the case, then the more reliable elevated temperature data would suggest that there is no variation in the magnitude of optical mode loss or its dependence upon wavelength with respect to temperature within the certainties of this experiment.

The elevated temperature spectra shown in Fig. 6.22 demonstrated no apparent trend between the optical mode loss and temperature at photon energies between 0.91 and 0.87eV. This suggests that there is no change in the optical mode loss for a change in temperature between 330K and 370K which exceeds the precision of this experiment (approximately 0.2cm^{-1}).

6.6.5 Temperature Dependence of Optical Mode Loss in Narrow Waveguide Core Samples

The temperature dependent optical mode losses of thin core waveguides (Fig. 6.24) are not as well resolved as those for wide waveguide cores, owing to weaker ASE present in this sample. As such, we fit linear trends to the optical mode loss below the band edge in Fig. 6.25 for comparison.
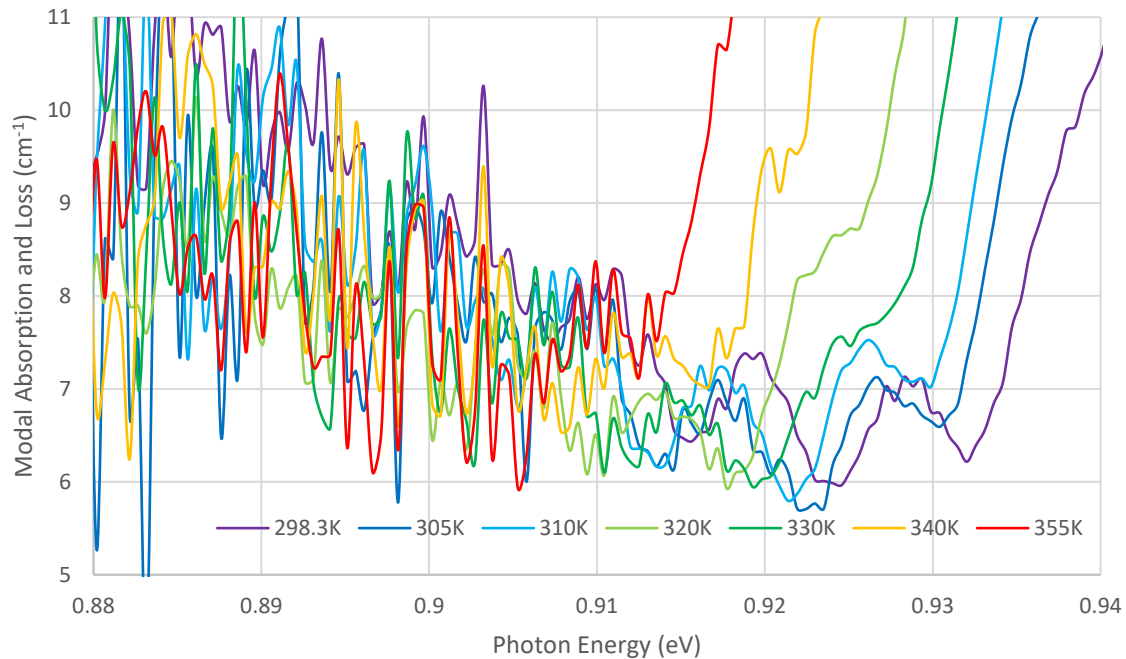
Figure 6.24 Below band-edge optical mode loss with increasing device temperature for thin waveguide core samples
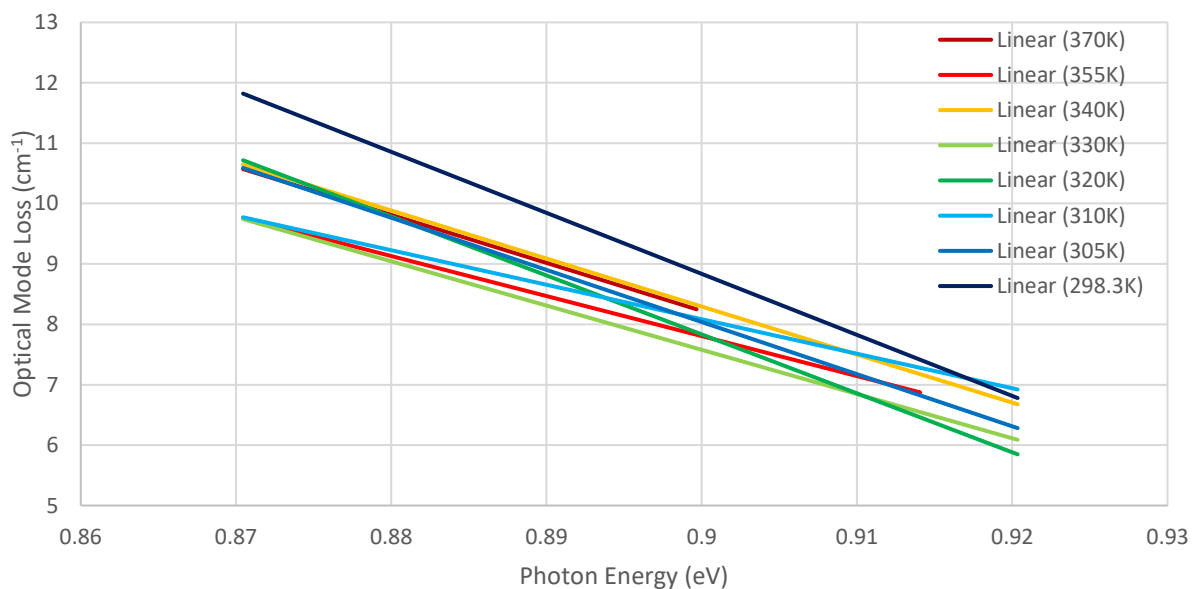
Figure 6.25 Linear fits of below band-edge optical mode losses with increasing device temperature for thin waveguide core samples

An important feature of the data presented in Fig 6.24 and 6.25 is the relative insensitivity of optical mode loss with respect to increasing temperature. While the band-edge of these spectra shift by as much as -20meV, the trend in modal absorption below the band-edge does not, suggesting its cause is independent of band-gap narrowing effects. This confirms our belief that the absorption below the apparent band-edge of these spectra is due to losses due to interactions which exist below the band gap of the device.

As seen in wide waveguide samples, there is an initial decrease in both the slope and net value of optical mode loss between room temperature and elevated temperatures. We interrogated this behaviour further and found that this change in optical mode loss is significant only in the initial 7K increase above room temperature (spectra obtained between 305K and 355K are otherwise well matched). Whether this discrepancy between room temperature and elevated temperatures is due to shortcomings in the experiment or an effect which represents a true reduction of optical mode loss is unclear .

If we once more assume that this discrepancy is due to an experimental error, we may conclude that there is no observable change in the wavelength dependence of optical mode loss in the thin waveguide core samples with increasing temperature within the precisions of this experiment. This suggests that the absorption is not strongly dependent upon IVBA in either of these samples.

6.7 Comparison of Measured Optical Mode Loss with Slope Efficiency

Room temperature modal absorption and loss spectra of the wide and narrow waveguide structures were used to extrapolate optical mode loss values of $(2.25\pm0.10)cm^{-1}$ and $(4.8\pm0.4)cm^{-1}$ respectively in Section 6.5. We will consider whether these values are consistent with the measured slope efficiencies of the device seen in Section 6.4.

Theory predicts that the extraction of light from a laser above threshold is proportional to the extraction factor: ——— (Eq. 2.10). As   decreases between these samples, provided there is no change in the internal differential quantum efficiency (or differential injection efficiency, then the measured DQE should increase proportionately. We will consider the DQE of the 2mm samples only, as these were obtained from a larger set of samples.

	Narrow Waveguide Sample	Wide Waveguide Sample
Measured DQE ( )	0.147	0.215
Measured ( ) (cm^{-1})	4.8	2.25
( ) (2mm sample) (cm^{-1})	6	6
Adjusted DQE ( )	0.164	

Table 6.4 Measured and modelled device characteristics for the narrow and wide waveguide core samples, for the purpose of comparing the change in slope efficiency with internal optical mode loss

$$\text{Equation 6.4}$$

$$\text{Equation 6.5}$$

$$\text{Equation 6.6}$$

Provided the same proportionality is present in the DQE of narrow and wide waveguide cores, then the DQEs may be related by Eq. 6.6. Given this, we may compare the DQE measured for narrow core waveguides with that predicted by the extraction factors calculated from the optical mode loss and mirror loss of the two samples and the measured DQE for the wide core samples, 0.147 and 0.164 respectively. This shows the results of the DQE measurements are largely explained by the change in optical mode loss measured, with the remaining difference in the internal efficiencies likely due to a difference in the recombination currents exhibited by the two waveguide cores.

6.8 Concluding Remarks

A comparison of waveguide structures for InAs QDs lasers on GaAs substrates has demonstrated improved slope efficiencies in laser structures with wider waveguide core thickness due to a reduction in the internal optical mode loss: (4.8±0.4)cm^{-1} and (2.25±0.10)cm^{-1} for samples with nominal waveguide core thicknesses of 2440Å and 3740Å respectively.

We have also shown the optical mode loss below the material band-edge may be compared with the modelled modal absorption due to FCA, ICBA and IVBA through the use of the modulated approach to the segmented contact method. We noted that the modelled optical mode loss underestimated the overall absorption by 0.5-1cm^{-1}, with a shallower trend than expected at room

temperature. A better agreement between the optical mode loss of wide waveguide core sample optical mode loss and its modelled values was demonstrated for data obtained at 340K. In this sample, we have shown that the wavelength dependence can be explained by the combined wavelength dependences of modelled FCA, IVBA and dispersion.

Modelled and experimental data obtained for the narrow waveguide core samples showed poorer agreement, suggesting wavelength dependent effects beyond the model used are not yet accounted for. We present strong evidence that these unaccounted for effects are a result of bend losses in the thin waveguide core. These will both account for the greater wavelength dependence of optical mode loss and the oscillations present throughout the spectra. Further work, beyond the scope of this thesis, would attempt to ascertain whether observable bowing of the substrate exists in these devices and if this is consistent with the oscillations observed.

Fimmwave. (2001). Oxford: Photondesign.

ADACHI, S. 1985. GaAs, AlAs, and AlxGa1–xAs: Material parameters for use in research and device applications. *Journal of Applied Physics,* 58, R1-R29.

HENRY, C., LOGAN, R., MERRITT, F. & LUONGO, J. 1983. The effect of intervalence band absorption on the thermal behavior of InGaAsP lasers. *IEEE Journal of Quantum Electronics,* 19, 947-952.

KOZO OSAMURA AND YOTARO, M. 1972. Free Carrier Absorption in n -GaAs. *Japanese Journal of Applied Physics,* 11, 365.

RINZAN, M., PERERA, A., MATSIK, S., LIU, H., BUCHANAN, M., VON WINCKEL, G., STINTZ, A. & KRISHNA, S. 2005. Terahertz absorption in AlGaAs films and detection using heterojunctions. *Infrared physics & technology,* 47, 188-194.

SKAULI, T., KUO, P. S., VODOPYANOV, K. L., PINGUET, T. J., LEVI, O., EYRES, L. A., HARRIS, J. S., FEJER, M. M., GERARD, B., BECOUARN, L. & LALLIER, E. 2003. Improved dispersion relations for GaAs and applications to nonlinear optics. *Journal of Applied Physics,* 94, 6447-6455.

SPITZER, W. G. & WHELAN, J. M. 1959. Infrared Absorption and Electron Effective Mass in n-Type Gallium Arsenide. *Physical Review,* 114, 59-63.

LEVINSTEIN,M. RUMYANTSEV, S. SHUR, M. 1996, *Handbook Series on Seimconductor Parameters*, World Scientific, London

HARRIS, A. J. & CASTLE, P. F. 1986. Bend Loss Measurements on High Numerical Aperture Single-Mode Fibers as a Function of Wavelength and Bend Radius. *Journal of Lightwave Technology,* LT-4, p. 34.

TANGONAN, G. L. 1988. HSU, H. P. JONES, V. PILKULSKI, J. Bend Loss Measurements for Small Mode Field Diameter Fibres. *Journal of Lightwave Technology,* LT-4, p. 34.

FAUSTINI, L. & MARTINI, G. 1997. Bend Loss in Single-Mode Fibers. *Journal of Lightwave Technology,* 15, Vol. 4, p. 671.

ETTENBERG, M. & PAFF, R. J. 1970. *Journal of Applied Physics,* 41, No. 10, p. 3926-3927.

Chapter 7   Conclusion

7.1   Summary of Work

This thesis demonstrates that improvements to the SCM for measurement of modal absorption and loss lead to the measurement of   with precisions of 0.1cm-1. These methods included a modulated approach to the SCM and a novel method of amplitude calibration of photodetector arrays by a flux superposition method. These improvements have also allowed us to confidently compare the wavelength dependence of   in InAs QD samples with varying waveguide core thicknesses.

The importance of the precise measurement of this waveguide dependence is show to be crucial to the extrapolation of the value of   at the lasing wavelength from optical mode losses below the band edge. We compared the experimental wavelength dependent   values with those experimental from waveguide models of these structures to confirm that this wavelength dependence, while not widely explored in the literature, was realistic due to the wavelength dependence of FCA, IVBA and wavelength dispersion.

Finally, an investigation into the temperature dependence of optical mode loss demonstrated no measurable change up to temperatures 370K in both the wide and narrow waveguide core thicknesses considered.

What follows is a breakdown of the individual findings of Chapters 4, 5 and 6 which have led to these core findings.

7.1.1 Summary of Findings: Chapter 4 Modulated Segmented Contact Method for Precise Measurement of Optical Mode Loss

- Precision of SCM for modal absorption and loss measurements shown to be limited by systematic drift incurred with increasing integration times. Adjusting for this drift based upon the perceived drift in signal intensity from a time series study of the data was seen to be inadequate for reducing this uncertainty to less than 0.1cm-1.

- Procedures for reducing the systematic drift of the SCM experiment were introduced including stabilising the position of the microtranslation stage, selected cooling power mode of the

detection system and limiting background light level. Systematic drift seen to persist despite these measures, therefore a method to reduce the impact of systematic drift is introduced: a modulated method of measurement of ASE from devices.

- We describe how this modulated approach can be generalised to any detection system where time series measurements could be saved, provided measurements taken during switching between sections and background readings could be removed. This approach is seen to introduce a loss of effective measurement time which limits the desirable rate of switching (which should be as frequent as possible where minimising systematic drift is key). Switching rate chosen led to approximately 30% loss of effective integration time.

- Repeated trials of the original SCM and its modulated approach for determining α_i (found from exponential fits to the modal loss below the band-edge) were used to compare the absolute uncertainty of the two methods with each other; and also to see whether the experimental uncertainty found from the 95% confidence values of the exponential fits were a good indicator of the measurement's uncertainty. The modulated method demonstrated a large reduction in uncertainty (from 0.33cm-1 to 0.14cm-1) and better agreement with the average uncertainty derived from the 95% confidence intervals (0.15cm-1 and 0.12cm-1 for the original and modulated methods respectively).

- The remaining discrepancy of 0.02cm-1 in the modulated method represents the remaining error from systematic drift. This may be reduced further by increasing the modulation frequency.

7.1.2 Summary of Findings: Chapter 5 Amplitude Calibration of Photodetector Array by Flux Superposition

- Amplitude calibration of InGaAs photodiode array detection system was motivated by a strong wavelength dependence of the optical mode loss, observable at wavelengths below the material band edge. Such wavelength dependence had not been demonstrated experimentally in devices emitting at telecoms wavelengths (1.3-1.6μm) previously. Investigation of this wavelength dependence led to the identification a non-linear response of in detection system.

- Initial measurements of a large non-linearity in the photodetector array shown by introduction of additional light from an IR lamp source to the measurement of spectrally resolved ASE from a segmented contact device across a line of pixels. A linear response of the detection system could

not be found under any illumination conditions.

- Non-linearity was then measured by the method of flux superposition, with respect to background corrected ASE collected from two segmented contact devices (operated by synchronised pulse generators) combined with a beam splitter.

- Non-linearity for each set of signal combinations was used to determine a conversion function for each individual pixel, expressable by two variables. These two variables were solved numerically by finding the minimum residual sum of the non-linearities measured with respect to a two dimensional array of possible conversion functions. The numerical fit was performed over two iterations.

- This amplitude calibration method was applied to modal absorption and loss data obtained from ASE of a segmented contact device measured at two different intensities (varied by reducing the iris diameter attached to a lens) to demonstrate the improved consistency of calibrated data with changing light intensity. The application of this calibration also showed the original data gave a large underestimate of the modal absorption and loss spectra, owing to the much larger difference in ASE for large values of absorption.

- The trend in the wavelength dependence originally observed was reduced slightly when data was calibrated, but was still large enough (a clear change of 1.5cm-1 across 125nm) such that a wavelength dependence of factors contributing to α_i must be considered in later modelling.

- Flux superposition method was used to compare the non-linearity of the detection system as measured when using high or low gain capacitor elements. Low gain element shown to be significantly more non-linear in its response. However, calibration by the flux superposition method was shown to reduce the residual non-linearity of the low gain capacitor to similar levels to that seen in when using a high gain capacitor.

7.1.2 Summary of Findings: Chapter 6 Waveguide Dependence of Optical Mode Loss

- Both improvements (amplitude calibration and modulated method) are used in the measurement of modal absorption and loss by the SCM to investigating the relationship between modal loss and waveguide core thickness.

- Performance of InAs QDWELL BA lasers with an expected lasing wavelength of 1.3μm, for 1, 2, 3 and 4mm long cavity lengths with as cleaved facets for samples with wide (3340Å) and narrow waveguide core (2040Å) thicknesses were investigated.

- The wide waveguide core samples appeared to exhibit the lowest threshold currents for 2mm long devices (153Acm-2 vs 201Acm-2 in the narrow waveguide core sample).

- The lasing wavelength of wide waveguide core samples was generally higher than the narrow waveguide core samples (1.309μm and 1.303μm respectively). The lasing wavelength of 1mm long devices was significantly shorter than this (1.207μm and 1.210μm for wide and narrow core samples respectively). This was due to short cavity lasers emitting using the first excited stated of InAs QDs.

- External differential quantum efficiencies were measured with respect to the 2, 3 and 4mm long cavities. These results showed a consistent improvement in the measured external differential quantum efficiency for the wide waveguide core samples, consistent with an improved value of α_i or internal differential quantum efficiency.

- The amplitude calibrated, modulated SCM is applied to two devices from each of the waveguide core thicknesses in order to test the repeatability of the measurement of α_i from device-device. The wide waveguide core samples demonstrated excellent agreement in their modal absorption, but deviated slightly at the peak modal absorption values. This change was consistent with a small (1°) uncertainty in the rotational alignment segmented contact devices (the modal absorption for which is strongly dependent on polarisation) with respect to the polariser element. α_i for these devices agreed to within 0.1cm-1, with respective values of (2.20±0.11)cm-1 and (2.26±0.16)cm-1. Errors are the sum of residual systematic drift error and precision of exponential fit from 95% confidence intervals.

- Values for   in the two narrow core samples meanwhile exhibited poorer agreement, with values of (5.06±0.22)cm-1 and (4.60±0.26)cm-1 observed. The calculated experimental uncertainties in this measurement was higher due to oscillations in modal absorption and loss observed in both spectra.

- The optical mode loss and its wavelength dependence in both structures was determined through modelling of the effective complex refractive indices, using values for the dispersive relations of the device layers and inferring the wavelength dependent absorptions of doped semiconductors from literature values.

- In the case of wide waveguide core samples the model closely matches the observed wavelength dependence of optical mode loss. This suggests that the wavelength dependence of FCA, IVBA and dispersion by the waveguide can explain shallow wavelength dependences in optical mode loss.

- For narrow waveguide core samples the resonant peaks of the model suggested weak guiding of the optical mode could allow coupling with the device structure beyond the cladding layer. However, the peak spacing of these oscillations with respect to wavelength of these resonances was much less than observed in the sample.

- We proposed that the oscillations in the experimental data greatly resemble the absorption oscillations present in single mode optical fibres, present due to a combination of weak guiding of the optical mode (consistent with our model) and bend losses.

- The bend loss oscillation phenomenon reported in the literature resembled that observed in narrow waveguide core segmented contact devices on several counts: the peak wavelength spacing was of a similar order (20-40nm in papers, 11-14nm in our samples); occurred at similar wavelengths (1.3-1.6μm); increased in amplitude with increasing wavelength; peaks of oscillations followed an exponential trend; peak spacing increases with increasing wavelength.

- In measuring the temperature dependence of modal absorption and loss, we saw the peak spacing of these oscillations increase with increasing temperature. This effect would be consistent with reduced bowing of devices with increasing temperature, due to a reduced lattice

mismatch between AlxGa1-xAs claddings and GaAs substrates with temperatures increasing from room temperature.

- Temperature dependence of optical mode loss was investigated with further measurements of the modal absorption and loss by the improved SCM with increasing device temperatures.

- Band-edge shifts of the wide and narrow waveguide core samples were identical with increasing temperature, suggesting the band-gap narrowing of their respective InAs QD and wetting layers are equal. This suggests the nominal growth of the active region of these devices was consistent.

- For elevated temperatures (305K-370K) no overall increase in the net value of optical mode loss or variation in its wavelength dependence was observed, in either the wide or narrow waveguide core samples. This suggested that IVBA was not a strong contributor to the optical mode loss observed.

- Because of the significant trend in increasing optical mode loss with wavelength in narrow waveguide structures, it was possible to see a contrast in the shift of the band-edge of the InAs QD with respect to no shift in the trend of optical mode loss. This confirmed that the trend in optical mode loss below the band-edge is independent of conduction band to valence band processes.

- The values for   obtained at room temperature from the modal absorption and loss experiments were used to infer whether a difference in   alone could give the change in   originally observed for 2mm long devices, given a change in the extraction factor which contributes to this term.

-     of these two samples were originally observed as 0.147 and 0.215 in the narrow and wide waveguide core samples respectively. A decrease in   consistent with that observed from modal absorption and loss measurements would give an adjusted value for   in the narrow waveguide core sample of 0.164. Additional change in   would be accounted for by difference in recombination current between different waveguide core structures.

7.2 Impact and Further Work

As a result of this work, I have demonstrated how improvements to the segmented contact method for the measurement of modal absorption and loss allow the measurement of optical mode loss of semiconductor lasers to precisions as low as 0.1cm^{-1}. With careful device selection, this measurement is shown to be repeatable across multiple segmented contact devices. As a result, it may be used to optimise semiconductor devices for optical mode loss with respect to a range of parameters, including waveguide geometry (as explored in Chapter 6) as well as doping density and profile.

In future applications of this work, I would hope to compare devices with differences in optical mode loss which approach this precision as this would prove the ultimate recommendation for this methodology. This might be achieved by investigating parameters which are expected to produce smaller differences in optical mode loss (e.g. smaller changes in waveguide core thickness) or by performing the measurement of optical mode loss upon a single device throughout it's lifetime (e.g. as part of a lifetime study).

While the calibration and modulated methods have been addressed individually, we can also consider how these experimental techniques relate to each other. For example, if a modulated approach to the amplitude calibration method were utilised, it would be possible to test for drifts in the non-linearity of the detector system. Correlation of this drift in non-linearity with, for example, environmental temperature, could prove useful in diagnosing and minimising systematic drift further.

The modulated method could see further improvement by assessing the reduction of systematic error with increasing switching rate in this system, against the loss of effective integration time this would introduce. A thorough investigation of the signal-noise ratio with decreasing exposure times may also be used to confirm if shorter exposure times, resulting in a smaller fraction of mixed signal frames, may be used to improve the measurement precision further. This will prove useful for either improving the precision of   further or reducing the necessary integration times.

Investigations into the oscillations in modal absorption and loss observed in narrow waveguide core samples are ongoing. The parallels between the oscillations we have observed and those seen in studies of bend losses in optical fibres strongly suggests that weak guiding of the optical mode and bowing of devices could be the cause. In order to confirm this is the cause, it would be necessary to determine if this bowing is observable and if this is consistent with the oscillations observed. Depending upon the scale of bowing, it may be possible to measure using a high magnification optical microscope. If the bowing is easily observed, we might go further and attempt to observe a variation in the bowing with increasing temperatures. Modelling of oscillations due to bend losses in optical fibres are discussed in the literature and could be adapted to the modelling of slab waveguides. If bend losses prove to be the cause of the increased loss in the narrow waveguide samples, then minimisation of device bowing for improved efficiency may prove an important consideration in quality control of laser diodes in industry.

As an alternative to the above approach, it may be possible to control the bowing of a segmented contact device by applying pressure in order to correct the device bowing. This might be achieved by incorporating a micrometer-controlled probe into the apparatus, while the segmented contact device is itself mounted upon two platforms (at the extremes of it's length) such that the central bowing of the structure may move freely when force is applied. Where a relationship between micrometer position and bowing is established, this may be used to determine the device curvature if optical measurement proves insufficient. Other means for applying force to the centre of this structure may utilise piezoelectric materials or materials with a very high coefficient of thermal expansion. I would anticipate that the oscillatory behaviour of thin waveguide core samples would be particularly sensitive to such an experiment, and so would be the ideal case to apply this method.

Because of the work conducted,   may be studied in greater detail than before. The applications presented in this work (characterisation of optical mode loss with respect to waveguide core thickness) can be extended to include devices with other changes in waveguide. These include changes in cladding thickness (which contribute greatly to overall device thickness), composition and doping concentration/profile.

It is also intended that this method be applied to investigating the influence of defects in the laser structure upon   . In particular, devices grown monolithically upon silicon substrates demonstrating poor lifetime performance due to propagating thermal defects would be investigated to consider whether increased optical mode loss is observed. This is important for determining the causes of poor lifetime performance in these structures; increased non-radiative recombination or increased optical mode loss.